國立交通大學

電子工程學系電子研究所

博士論文

應用於生醫感測與高速網路之
互補式金氧半光偵測器

CMOS Photodetectors for Biomedical Detections and High-Speed Networks

研 究 生 ：張育維

指導教授 ：黃遠東博士

中華民國 九十八 年 七 月

應用於生醫感測與高速網路之
互補式金氧半光偵測器

CMOS Photodetectors for Biomedical Detections and High-Speed Networks

研究生：張育維　　　Student: Yu-Wei Chang
指導教授：黃遠東博士　　　Advisor: Dr. Yang-Tung Huang

國立交通大學
電子工程學系電子研究所
博士論文

A Dissertation
Submitted to Department of Electronics Engineering and Institute of Electronics
College of Electrical and Computer Engineering
National Chiao Tung University
in Partial Fulfillment of the Requirements
for the Degree of
Doctor of Philosophy
in
Electronic Engineering

July 2009
Hsinchu, Taiwan, Republic of China

中華民國九十八年七月

應用於生醫感測與高速網路之
互補式金氧半光偵測器

研究生：張育維　　　　　　　　指導教授：黃遠東博士

國立交通大學

電子工程學系電子研究所

摘要

本研究提出四種應用於生醫感測與高速網路之積體互補式金氧半(CMOS)光偵測器，研究內容包含了設計、分析、製作、與量測。在生醫感測的應用上，提出P^+/N_{well}指狀光二極體(finger photodiode)搭配轉阻放大電路(trans-impedance amplifier)，可量測過氧化氫(H_2O_2)、葡萄糖(glucose)與組織胺(histamine)的最低濃度分別為 1 μM、1 μM與 10 μM；提出基板浮接(floating bulk)環狀光電晶體(ring-shaped phototransistor)搭配外環光二極體，在可見光波段具有高於 1000 A/W的響應度(responsivity)，對於辣根過氧化酶(HRP)的檢測極限為 2.7 pM。在高速網路的應用上，提出的網狀空間調變光二極體(spatially modulated photodiode)，可有效地把光電流中的慢速成分扣除，所設計製作的元件展現出 5.5 GHz的高頻寬；提出之具深N_{well}層的PIN光二極體，其深N_{well}層被連接到高電位以排除在P_{sub}層所產生的慢速擴散載子，所設計製作的元件對於 50 Ω負載可達 800 mV_{pp}輸出電壓與 2.5 Gbps操作速度。所開發之光偵測器效能皆比文獻上其他金氧半光偵測器高。

CMOS Photodetectors for Biomedical Detections and High-Speed Networks

Student: Yu-Wei Chang Advisor: Dr. Yang-Tung Huang

Department of Electronics Engineering and Institute of Electronics

National Chiao Tung University

ABSTRACT

The design, analysis, manufacture, and measurements of the four integrated CMOS photodetectors for biomedical detections and high-speed networks are presented. For biomedical applications, the proposed P^+/N_{well} finger photodiode with a trans-impedance amplifier demonstrated that the minimum concentration successfully detected for H_2O_2, glucose, and histamine were 1 μM, 1 μM, and 10 μM, respectively; the proposed ring-shaped phototransistor with a floating bulk enclosed by a ring-shaped photodiode exhibited a responsivity higher than 1000 A/W for the visible spectrum range and a detection limit of 2.7 pM for HRP (horse-radish peroxidase). For high-speed applications, the meshed SMPD (spatially modulated photodiode) can effectively subtract the deferred portion from the immediate portion of the photocurrent, and the manufactured device demonstrated a high bandwidth of 5.5 GHz; the proposed DNW-based (deep-N_{well}-based) PIN photodiode, in which the slowly diffusive carriers generated in P_{sub} are decoupled from the photocurrent by connecting the DNW to a positive supply voltage, was capable of outputting 800 mV_{pp} with up to 2.5 Gbps for 50-Ω loads. These proposed photodetectors exhibited better performances than other reported CMOS photodetectors.

誌　謝

博班生涯看似短短幾年，實則對整個長遠的人生有著莫大助益。這段期間的歷練，幫助我內心成長與蛻變，一一回想起來都相當珍貴，要感謝的人有好多好多。

首先，我想感謝指導教授黃遠東老師多年來的殷殷教誨，言教上，孜孜不倦地引導我嚴謹踏實的求學態度，身教上，始終秉持著一絲不苟的處世原則。看到老師常常費盡氣力地批改大大小小的研究論文，只希望學生能夠早點進入狀況獨當一面，我深深地體會到蠟燭那種不惜燃燒自己只為照亮別人的精神，感動萬分。此外，老師也訓練我學習採購儀器、建立系統、撰寫計畫、接待外賓、出國觀摩、擔任助教、帶專題生，並鼓勵我參與服務學習、為原住民上山課輔，熱心公益、開闊人生觀，這些五彩繽紛的豐富經驗，讓我覺得博班生涯不虛此行，值回票價！

對於跨領域的研究而言，想要把元件設計、生醫檢測、高速網路整合起來，單靠我一根朽木是難撐大廈的，幸好有了許多志同道合的夥伴一起來築夢。在生醫檢測的應用上，感謝楊裕雄老師的指導，以及夥伴游秉鈞、戴妤庭、林明瑜的協助。在高速網路的應用上，感謝陳巍仁老師的指導，以及夥伴劉川漳、黃世豪的協助。關於論文內容的呈現，也感謝各位口試委員所給予的肯定與寶貴建議。

實驗室的成員能夠齊聚一堂，就是一種緣分。感謝博班學長鄧俊修、許世欣、許俊彥、裴廷漢、林俊廷、呂明峰的經驗分享，以及博班同儕楊玉麟、徐新峰、陳建華的相互照應，當然還有每年來來去去、族繁不及備載的碩班學弟所帶來的歡樂氣氛。

在精神層面上，我很感謝爸爸、媽媽、弟弟、女友這一路上的支持與鼓勵，心的力量是無遠弗屆、沒有極限的！遇到任何境界，只要正面積極地看待，都可以轉化為生生增上的泉源。在此也由衷地感謝上日下常老和尚慈悲的甘露法語，以及福智團體所提供的學習資源，幫助我更瞭解生命的價值，建立崇高的人生目標。站在巨人的肩膀上，讓我可以看得更高、更遠、更美好。所以，只要是對一切眾生無限生命有幫助的事，不論過程有多艱辛、別人都不願意作的，我也要努力去完成它！

祝福大家，都能獲得最圓滿的快樂 ^_^

Contents

List of Tables

List of Figures

Chapter 1

Introduction

1.1 Integrated CMOS Photodetectors

The CMOS (Complementary Metal-Oxide Semiconductor) technology is economically the most important technology for the manufacture of microelectronic circuits [1]. Its power dissipation is much smaller than other technologies, and this allows to integrate much more CMOS gates on IC (integrated circuits) than in NMOS or bipolar technology, resulting in much better performance.

Semiconductors are the ideal material for internal photoelectric effect because of the high carrier mobility, the low dark current, and the high efficiency for carriers generation compared to phonon generation or single carrier excitation [2]. For a semiconductor photodetector, the electron-hole pairs generated by photon absorption contribute to the internal electrical conduction of the device, and contribute to a corresponding current at the contacts of the external circuits.

The realization of photodetectors in a standard CMOS technology has attracted much interest in the last decade. This is owing to its low cost, high throughput, and the capability for integration with subsequent circuits without any process modification. These properties enable the manufacture of complete data-acquisition systems on a single silicon chip [3].

For a integrated CMOS photodetector, there is a trade-off between the gain and the bandwidth. The photodetector for biomedical applications is focused on the high gain, whereas the photodetector for high-speed applications is focused on the high bandwidth. In this dissertation, the design, analysis, manufacture, and measurements of the proposed CMOS photodetectors for biomedical applications and high-speed applications are presented respectively.

1.2 Integrated CMOS Photodetectors for Biomedical Applications

With the rapid progress of biotechnology and microelectronics, a new generation of biomedical diagnosis is expected worldwide. The development of a portable, accurate, inexpensive, and easy-to-use biosensor has become the most important niche in the health care industry [4], [5]. Detecting the optical properties changed by chemical reactions is a competent approach to examine various important biological molecules [6], [7].

Among the optical biosensing techniques, emission photometry and absorption photometry have drawn substantial attention in the area of medical diagnosis [4]–[12]. Emission photometry is the detection of the light emitted by molecules through chemical reactions in response to the concentration of an analyte. The light emission process can further be classified into chemiluminescence, fluorescence, and phosphorescence according to specific characteristics. This popular technique is capable of real-time measurement with high selectivity to the analyte. However, it may suffer from luminophor degeneration, which leads to signal attenuation with time [7]–[11]. Circumventing this difficulty, absorption photometry, another widely used technique, relies on the change of photon absorption through chemical reactions in response to the analyte concentration. The biosensing system based on absorption photometry offers advantages for analyte monitoring with high spatial resolution and has potential for applications in microarray analysis [7], [12].

Regarding the commercial instruments for optical analysis, a photomultiplier tube usually serves as the optical sensor in a spectrophotometer. Commonly used wavelength range includes ultraviolet and visible light. Despite its high sensitivity, the spectrophotometer has limited applications in home care instruments because of its bulky size, high cost, and high voltage (about 1000 V) [2]. On the other hand, the integrated CMOS photodetector is characterized as having a small size, a low cost, a high throughput, and low power consumption. Hence it becomes an attractive candidate for personalized diagnostic kits. Although much research has been devoted to CMOS biosensor using emission photometry, few studies have been done on CMOS biosensor using absorption photometry [7], [9].

In this research, two optical biosensing system were developed based on absorption photometry. The proposed integrated CMOS photodetectors include the finger photodiodes and ring-shaped phototransistors. Experimental results demonstrated high sensitivities, and the miniature systems would have potential toward a practical home care instrument for personalized clinical diagnosis.

1.3 Integrated CMOS Photodetectors for High-Speed Applications

Due to the steadily increasing demands for system clock frequencies, electrical interconnects suffer a lot from design problems, including system synchronization, power dissipation, impedance matching, and pin inductance. To avoid these problems, using optical interconnects between chips or boards would be an effective way [13], [14]. The semiconductor materials suitable for optical components can be generally divided into two categories. On the one hand, optical components manufactured in III-V materials require a hybrid technology, which leads to a relatively high cost and high power consumption. On the other hand, silicon is characterized as high throughput and low cost, and hence becomes an attractive candidate for integrating photodetectors with subsequent circuits.

In a standard CMOS technology, a P/N junction can be formed by adopting the N_{well}/P_{sub}, N^+/P_{well}, or P^+/N_{well} junction. For 850-nm incident light, the absorption depth of silicon is approximately 16.7 μm, and the N_{well}/P_{sub} junction is typically adopted to achieve a wider depletion region as well as a larger drift current. But the N_{well}/P_{sub} junction depth (about 2 μm) is so shallow that a large portion of photogenerated carriers are deep in the substrate and results in a slow diffusion response. Consequently, a traditional CMOS photodiode made by a single N_{well}/P_{sub} junction is not capable of high-speed operation. Efforts were contributed to circumvent this bottleneck in recent years, such as the finger photodiode [15], [16] and the finger-shaped spatially modulated photodiode (SMPD) [17]–[20]. The finger photodiode adopts interdigitated P/N junctions to increase the depletion regions. It can improve the responsivity, but the photocurrent is still dominated by the substrate current, which makes the improvement in bandwidth insignificant. The finger-shaped SMPD composes of a row of junction diodes which are alternatively covered and uncovered with optical masks. This SMPD structure finds a way to weaken the influence of the substrate current by subtracting the deferred portion from the immediate portion of the photocurrent.

In this research, two types of CMOS photodetectors were investigated to further improve the frequency response: enhanced SMPDs and deep-N_{well} based photodiodes. Experimental results exhibited higher operating speed compared to the prior art, and the proposed photodetectors would be beneficial to the high-speed networks.

1.4 Organization of The Dissertation

This dissertation is organized as follows. Chapter 2 deals with a biosensing system on the basis of the finger photodiode and trans-impedance amplifier. The biomedical detections of H_2O_2, glucose, and histamine are also examined. Chapter 3 is concerned with the ring-shaped phototransistor, which exhibits a high sensitivity and a low sample-volume requirement for the biomedical detection. In Chapter 4, the square-shaped SMPD and meshed SMPD are addressed to eliminate the slow substrate photocurrent for higher bandwidth. Chapter 5 presents the deep-N_{well} based PIN photodiodes for applications in high-speed networks. Finally, the conclusion is given and the future works are suggested in Chapter 6.

Chapter 2

Optoelectronic Integrated Circuits for Biomedical Applications

2.1 Introduction

Based on a standard CMOS technology and absorption photometry, an optical biosensing system is proposed [21]. The whole system was assembled into a compact prototype, and it exhibits a high sensitivity and real-time measurement capability.

2.2 Principles and Methods

2.2.1 Absorption Photometry

The absorbance A of the materials is described by the Beer-Lambert law [6]

$$A = -\log\left(\frac{I}{I_0}\right) = \epsilon_\lambda \cdot l \cdot c \quad \Longrightarrow A \propto c \tag{2.1}$$

where I_0 and I respectively denote the initial light intensity and the light intensity after passing through the material, ϵ_λ is the wavelength-dependent molar absorptivity in units of $\mathrm{l \cdot mol^{-1} \cdot cm^{-1}}$, l is the path length in units of cm, and c is the concentration of absorbing species in the material in units of $\mathrm{mol \cdot l^{-1}}$. With a monochromatic light source and a fixed path length, the absorbance would be proportional to the analyte concentration. Thereby detecting the optical signals modulated by the biochemical reactions is an efficient way to quantitate the analyte.

For the enzyme reaction, the initial rate v of the overall reaction is expressed as [22]

$$v = \frac{dA}{dt} = \frac{V_{\max} \cdot [\text{analyte}]}{[\text{analyte}] + K_m} \Longrightarrow v \propto [\text{analyte}], \quad \text{when } [\text{analyte}] \text{ is small} \tag{2.2}$$

where $V_{\max}$ represents the maximum reaction rate, [analyte] represents the analyte concentration, and K_m represents the Michaelis constant defined as the analyte concentration at which the reaction occurs at half of the maximum rate. K_m is an indicator showing the affinity between an enzyme and a given substrate; at the same time it further reveals the stability of the enzyme-substrate complex. Referring to Equation (2.2), while [analyte] is much smaller than K_m, the initial rate v would be approximately proportional to [analyte].

2.2.2 Biochemical Reactions

In this research, the ABTS/H_2O_2/HRP method is adopted as the basis for biomedical applications; ABTS represents 2,2'-azino-bis(3-ethylbenzthiazoline-6-sulphonic acid), and HRP stands for horseradish peroxidase. The biochemical equation is expressed as [23]

$$\text{ABTS} + H_2O_2 \xrightarrow{\text{HRP}} \text{ABTS}^+ + H_2O \tag{2.3}$$

For qualitative analysis, one can easily observe this chemical reaction since the ABTS solution is visually light green and the ABTS^+ solution is dark blue. For quantitative analysis, one can detect the optical absorbance of the solution to evaluate the concentration. The absorption spectra obtained from a standard spectrophotometer (Hitachi U-3310) show that ABTS has an absorption peak at 340 nm with 50-nm FWHM (full width at half maximum), whereas ABTS^+ has an absorption peak at 415 nm with 50-nm FWHM and lower broad peaks at 640 nm and 730 nm as shown in Figure 2-1.

Moreover, many important biomedical targets such as glucose, histamine, lactate, and uric acid, can be successfully catalyzed to H_2O_2 by different enzymes. The biochemical reactions for glucose and histamine can be expressed as [24]

$$\text{Glucose} + O_2 \xrightarrow{\text{GOx}} \text{Gluconic Acid} + H_2O_2 \tag{2.4}$$

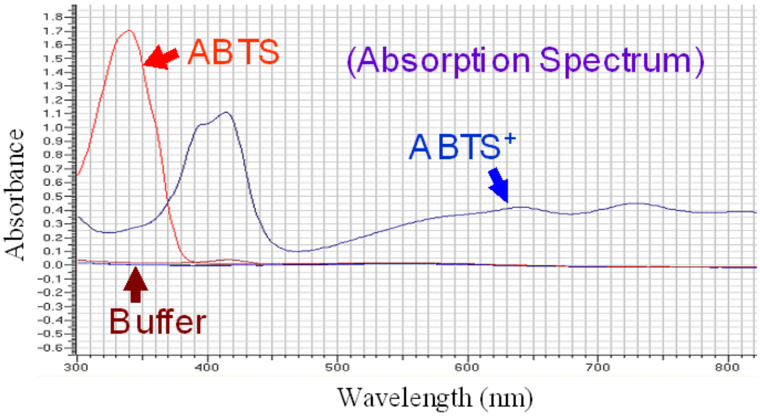

Figure 2-1: The absorption spectrum of ABTS and $ABTS^+$.

$$\text{Histamine} + H_2O \xrightarrow{\text{DAO}} \text{ImAA} + NH_3 + H_2O_2 \tag{2.5}$$

where GOx and DAO represent glucose oxidase and diamine oxidase, respectively, and ImAA stands for imidazole acetic acid. Glucose is the essential substance in terms of metabolism; the glucose concentration in the blood is an efficient indicator for follow-up examination of diabetes [7]. Another example is histamine, a biogenic neurotransmitter. It can influence many cells' reactions, including allergy and inflammation. With sufficient ABTS and HRP, coupled enzymatic reactions can be formed by combining (2.3) with Equation (2.4) and Equation (2.5), respectively. The absorbance of the materiel would be proportional to the concentration of glucose and histamine, respectively. Therefore, the ABTS/H_2O_2/HRP method is quite useful to quantitate these targets' concentration for medical diagnosis.

2.2.3 Finger Photodiode and Transimpedance Amplifier

As shown in Figure 2-2, the CMOS biochip was mainly composed of a photodetector and a TIA (transimpedance amplifier). Figure 2-3 depicts the top view and cross section of the proposed P^+/N_{well} finger photodiode. Typically, a CMOS photodiode can be formed by adopting a $N_{\text{well}}/P_{\text{sub}}$, N^+/P_{well}, or P^+/N_{well} junction. With the illumination of the short wavelength light for biochemical experiments, the absorption depth of silicon is quite shallow, and most photogenerated carriers are very close to the photodiode surface. Since only the excess carriers inside the depletion region and within the diffusion length

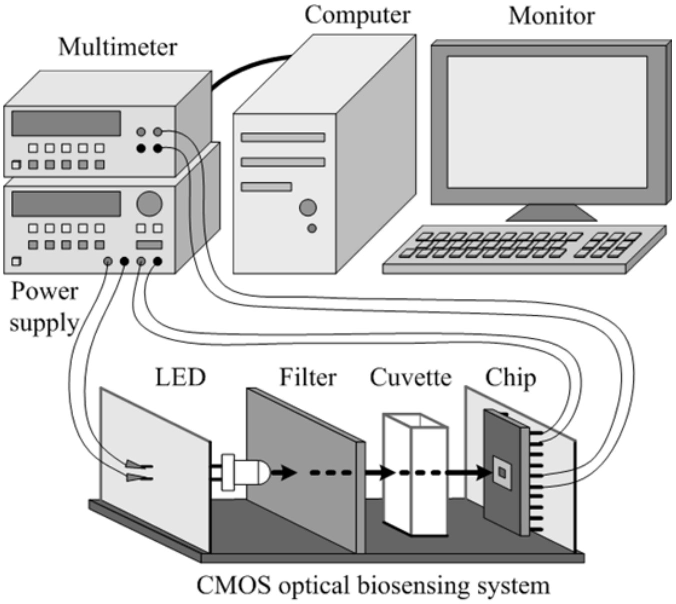

Figure 2-2: The diagram of the miniature CMOS optical biosensing system and the experimental setup.

contribute to the photocurrent, the shallower P^+/N_{well} junction (about 0.2-μm deep) was adopted in this study to accomplish a better responsivity. (N^+/P_{well} junction is an alternative.) Moreover, the interdigitated P^+/N_{well} junctions was used to extend the depletion regions near the surface and hence increase the photocurrent [25]. Each P^+ stripe was 1-μm wide with 4-μm seperation between stripes, and the stripes were interconnected by metal lines and contacts. The total area of this finger photodiode was 100 μm × 100 μm. The photodiode was surrounded by double guard rings to keep the substrate noise off; the P^+ guard ring was connected to ground, and the N^+ guard ring was connected to a high potential [26].

In a standard CMOS technology, the dielectric layers above the active region comprise an inter-layer dielectric layer, inter-metal dielectric layers, and optional passivation layers (PASS). For a multi-layer structure, the reflectance can be calculated by using the impedance-transformation approach [27]. The effective wave impedance Z_i at the front of the ith layer is expressed as

$$Z_i = \eta_i \frac{Z_{i+1} + j\eta_i \tan(k_i d_i)}{\eta_i + jZ_{i+1} \tan(k_i d_i)} \tag{2.6}$$

where η_i, k_i, and d_i denote the intrinsic impedance, the wavenumber, and the thickness

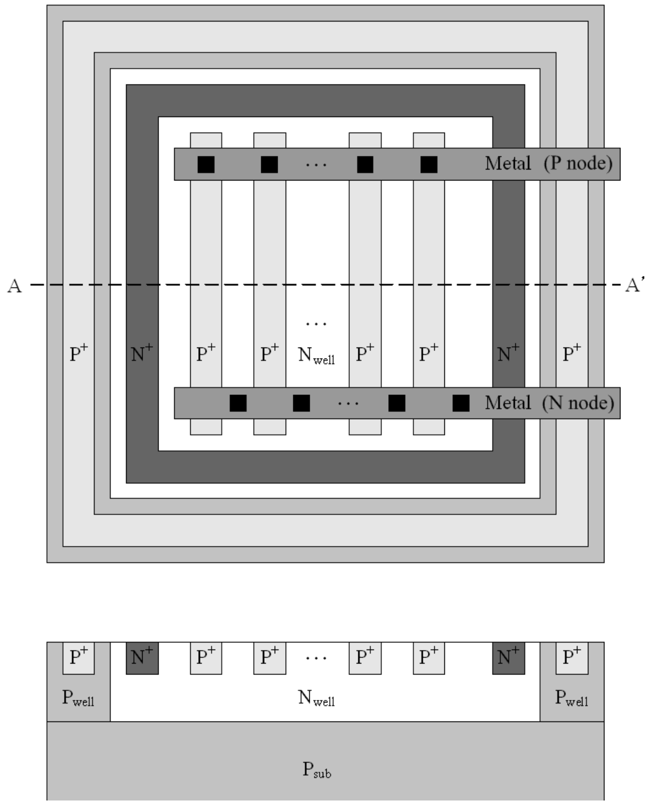

Figure 2-3: The top view and cross section of $\mathrm{P}^+/\mathrm{N}_{\mathrm{well}}$ finger photodiode.

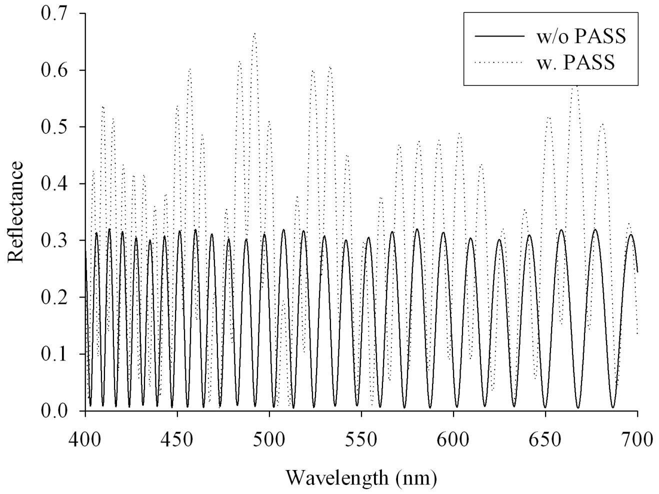

Figure 2-4: The calculated reflectance as a function of wavelength for the device with and without passivation layers.

of the ith layer, respectively; Z_{i+1} denotes the effective impedance at the front of the $(i+1)$th layer. This recursive calculation starts from the known impedance of the last layer (silicon substrate), $Z_{\text{last}} = \eta_{\text{Si}}$, backward to the effective impedance at the front of the surface layer, Z_1. Then the reflectance R of the photodiode can be obtained as

$$R = \left| \left(\frac{Z_1 - \eta_0}{Z_1 + \eta_0} \right)^2 \right| \tag{2.7}$$

where η_0 is the intrinsic impedance of air. For the device with and without PASS, the simulation results of the wavelength-dependent reflectance are shown in Figure 2-4. By removing PASS above the active region of the photodiode, simulation results show that the reflectance can be reduced from 0.169 to 0.116 for the 430-nm light, and from 0.481 to 0.006 for the 650-nm light.

As shown in Figure 2-5, the subsequent circuit included a current source, a current mirror, a TIA, and an output buffer. The TIA consisted of a common-source stage M_0, two source followers M_1 and M_2, and an external feedback resistance R_F. M_1 served in the feedback loop to isolate R_0 from the loading effect, and M_2 drove the load capacitance to alleviate the stability issue [28]. The gain of the TIA is given as

$$A_T = \frac{R_F g_{m0} R_0}{1 + (R_F g_{m0} R_0)/R_F} \simeq R_F, \qquad \text{for } g_{m0} R_0 \gg 1 \tag{2.8}$$

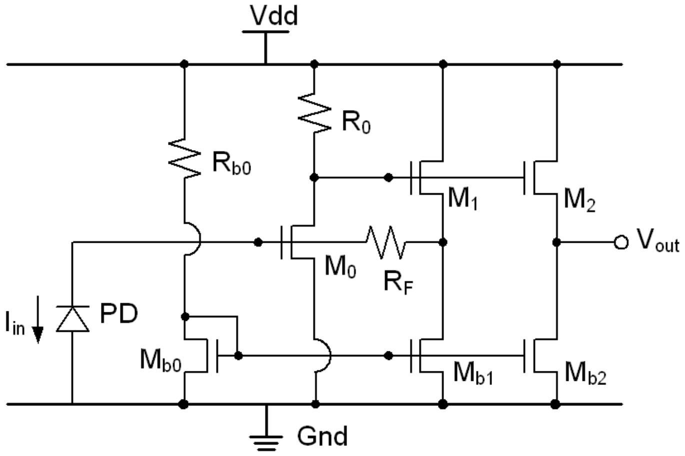

Figure 2-5: The configuration of the subsequent circuit. Device parameters are $M_0 = (100$ μm/0.5 μm), $M_1 = M_2 = (50$ μm/0.5 μm), $M_{b0} = M_{b1} = M_{b2} = (1$ μm/0.5 μm), $R_0 = 8$ kΩ, and $R_{b0} = 15$ kΩ.

where g_{m0} is the transconductance of M_0; $g_{m0}R_0$ was designed large enough to make A_T approximated to R_F. The external R_F allowed us to adjust the amplification factor and the dynamic range of the TIA. The input-referred noise current of the TIA is given as

$$\overline{I_{n,in}^2} = \frac{4kT}{R_F} + \frac{4kT}{R_F^2}\left(\frac{\gamma}{g_{m0}} + \frac{1}{g_{m0}^2 R_0} + \frac{\gamma}{g_{m0}^2 g_{m1} R_0^2}\right) \tag{2.9}$$

where g_{m1} is the transconductance of M_1, and γ is the excess noise coefficient [28]. The input-referred noise current were reduced by enlarging g_{m0}, g_{m1}, R_0, and R_F. In addition, to prevent the above-mentioned circuits from illumination, these regions were covered with floating metals as optical masks.

2.2.4 Biosensing System Setup

The diagram of the proposed CMOS optical biosensing system is illustrated in Figure 2-2. A narrowband LED is used as the light source, and a bandpass filter allows the light of a specific wavelength to travel through the cuvette, in which the light is partially absorbed by the biochemical materials. The light after passing through the cuvette is detected by the CMOS biochip, which is mainly composed of a photodetector and a transimpedance amplifier (TIA). The photodetector converts the transmitted optical signals into current signals, and then the TIA converts them into voltage signals. The voltage signals are measured by a multimeter (Agilent 34401A), which is connected to a personal computer via a general purpose interface bus (GPIB), and an application software (Labview) is used for data acquisition.

2.2.5 Preparation of Biochemical Reagents

The biochemical experiments were assisted by Prof. Yuh-Shyong Yang's group. ABTS (10 mg/tab), H_2O_2 (30%, W/W), HRP (250 U/mg), β-D-glucose, histamine, and DAO from porcine kidney (0.06 U/mg) were purchased from Sigma. GOx from Aspergillus Niger was purchased from Fluka. Sodium phosphate powders (monobasic and dibasic) were obtained from J. T. Baker. Other chemical reagents were of analytical grade and were used without further purification.

The HRP, GOx, and DAO stock solutions were prepared in a 100-mM phosphate buffer and were stored at -20 °C. These stock enzyme solutions were melted in an ice bath just before use and were diluted with a pH 7.0 phosphate buffer. The activity assays of HRP, GOx/HRP, and DAO/HRP in the systems containing various concentrations of H_2O_2, glucose, and histamine, respectively, were initiated by adding 1-ml colorimetry reagent (30-mM ABTS in a 100-mM phosphate buffer, pH 7.0). The reactions were performed at 25 °C (for HRP and GOx/HRP) and 37 °C (for HRP and DAO/HRP), respectively.

2.3 Experimental Results

2.3.1 Characteristics of the Whole System

The biochip was manufactured using the TSMC (Taiwan Semiconductor Manufacturing Company) 0.35-μm CMOS technology. The die size (including the photodiode, core circuits, and I/O pads) is 1.35 mm × 1.35 mm. The dimensions of the miniature biosensing system shown in Figure 1 are about 8 cm (length) × 6 cm (width) × 7 cm (height). The finger photodiode was reverse-biased moderately to ensure that the photocurrent was linearly proportional to the absorbed photons. The photocurrent was then converted into voltage signal by the subsequent TIA. With a 3-V power supply, the lower bound and upper bound of the output voltage were 0.49 V and 2.02 V, respectively.

Red LEDs (Centenary 31134) and a bandpass filter (Onset 650FS10-50) were used to produce 650-nm light. When the biochip was illuminated, the output voltage V_{out} as a function of the input optical power for a 650-nm wavelength is shown in Figure 2-6(a). For R_F =10 MΩ and 1 MΩ, the sensitivities were approximately 145 V/μW and 16 V/μW, respectively. But the output voltage V_{out} for R_F =10 MΩ would saturate at 2.02 V when the input optical power was larger than 10 nW. Combining the results of the linear region with (2.1) gives the corresponding relationships between the absorbances and the output voltages for two different R_F's, as shown in Figure 2-6(b). These relationships would be beneficial for the analysis of biochemical experiments since the absorbance of the material is proportional to the target's concentration.

Similarly, purple LEDs (Centenary 40327) and a bandpass filter (Newport 20BPF10-430) were used to produce 430-nm light. When the biochip was illuminated, the output voltage as a function of the input optical power for a 430-nm wavelength is shown in Figure 2-7(a). For R_F =10 MΩ and 1 MΩ, the sensitivities were approximately 26 V/μW and 3 V/μW, respectively. The output voltage V_{out} for R_F =10 MΩ would saturate at 2.02 V when the input optical power is larger than 60 nW. The relationships between the absorbances and the output voltages for two different R_F's are shown in Figure 2-7(b).

The measurement results of the CMOS chip indicate that the sensitivity of 650-nm light is higher than that of 430-nm light. But from the perspective on the biochemical product ABTS$^+$, the absorption of 430-nm light is stronger than that of 650-nm light. Accordingly, for comparison, the following biochemical experiments were performed with 650-nm light and 430-nm light individually.

2.3.2 H_2O_2 Detection

The biochemical equation of the ABTS/H_2O_2/HRP method is expressed in Equation (2.3). When the substrate ABTS and the enzyme HRP are sufficient, the amount of the product ABTS$^+$ would be proportional to the H_2O_2 concentration. For the experiment performed using 650-nm light and R_F = 1 MΩ, Figure 2-8(a) illustrates the real-time measured voltages V_{out} under various H_2O_2 concentration, with an arrow indicating the trend of increasing concentration (incr. conc.). The minimum H_2O_2 concentration was successfully detected as 1 μM, which is one order of magnitude better than the limit reported in previous literatures (about 50 μM) [4], [5], and is even comparable to the limit obtained from a commercial spectrophotometer (Hitachi U-3310). With the relationship depicted in Figure 2-6(b), the absorbance at each time point for various H_2O_2 concen-

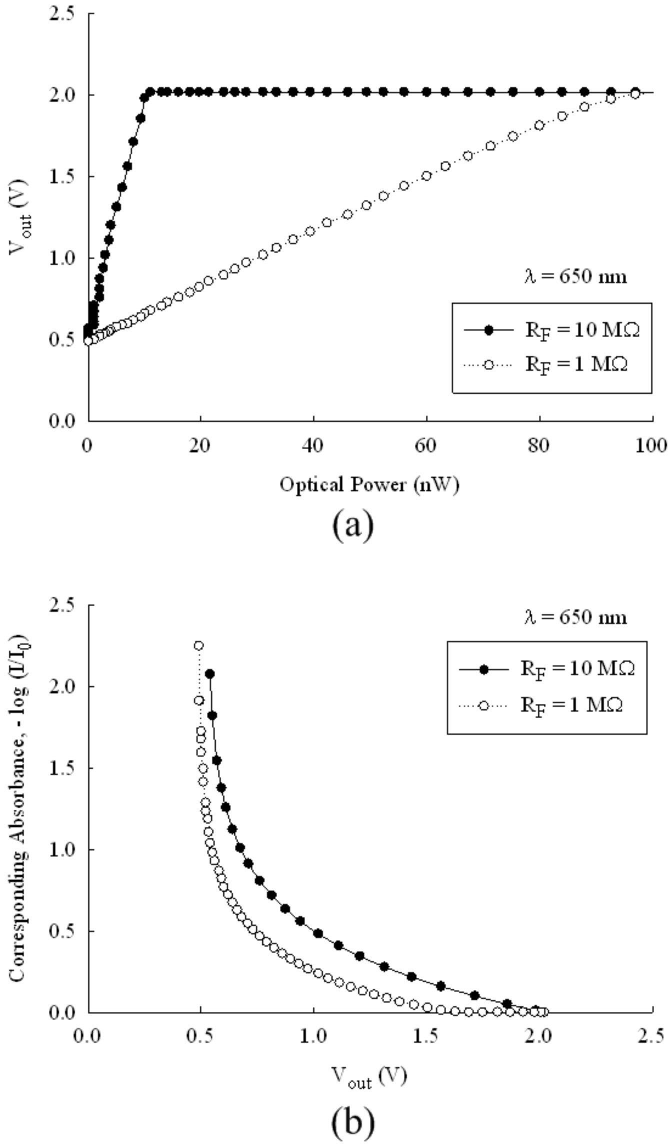

Figure 2-6: Experimental results of the CMOS optical biosensing system with $R_F = 10$ MΩ and $R_F = 1$ MΩ at $\lambda = 650$ nm. (a) The output voltage versus the input optical power. (b) The corresponding absorbance versus the output voltage.

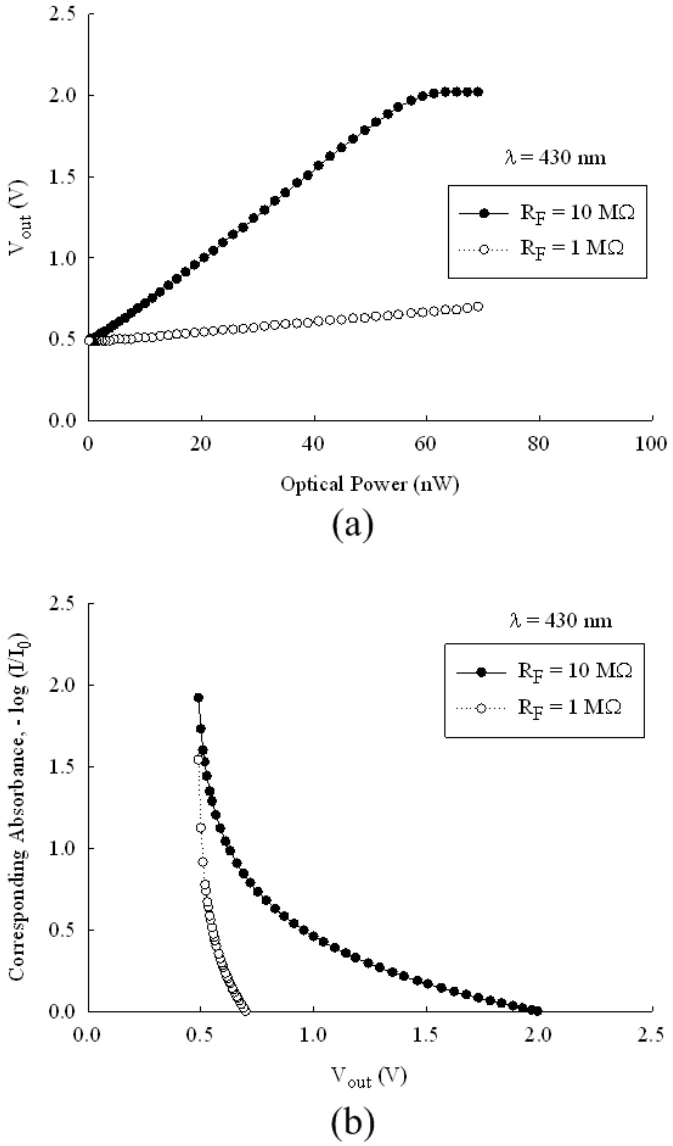

Figure 2-7: Experimental results of the CMOS optical biosensing system with $R_F = 10$ MΩ and $R_F = 1$ MΩ at $\lambda = 430$ nm. (a) The output voltage versus the input optical power. (b) The corresponding absorbance versus the output voltage.

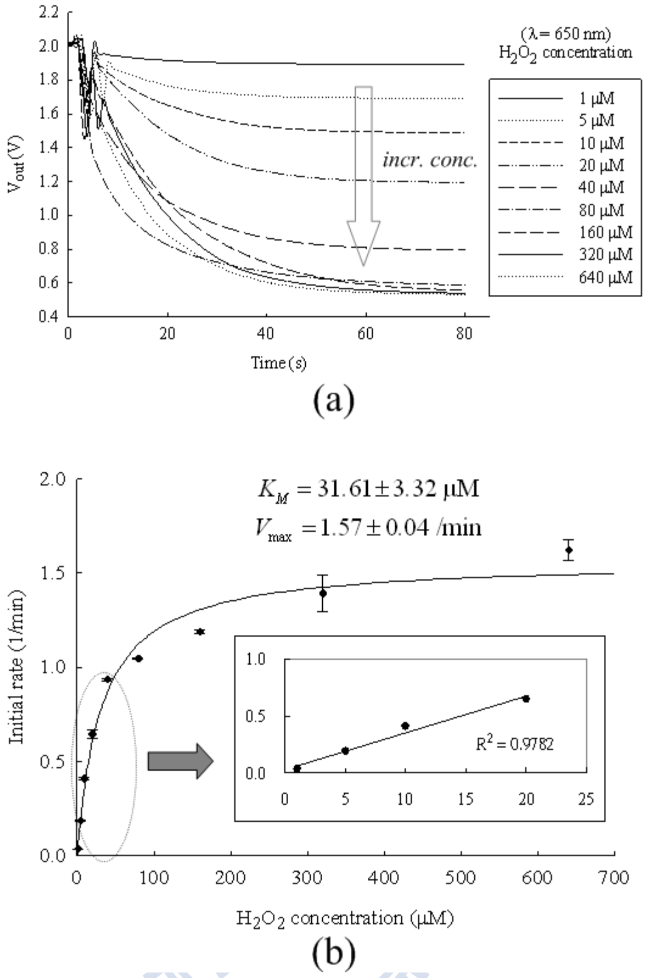

Figure 2-8: Experimental results of the H_2O_2 detection with 650-nm light at 25 °C. (a) Real-time measurement of the output voltage for t = 0–80 s. (b) The Michaelis-Menten plot.

tration can be obtained. The Michaelis-Menten plot of H_2O_2 concentration is shown in Figure 2-8(b), where the Michaelis constant $K_m = 20.22 \pm 3.31$ μM was computed by using a nonlinear regression program (SigmaPlot). For a small [H_2O_2], the experimental results demonstrate a good linearity with the coefficient of determination $R^2 = 0.9782$, as shown in the inset of Figure 2-8(b).

Similarly, for the experiment performed using 430-nm light and $R_F = 10$ MΩ, Figure 2-9(a) illustrates the real-time measured voltages V_{out} under various H_2O_2 concentration. The minimum H_2O_2 concentration was successfully detected also as 1 μM. With the relationship depicted in Figure 2-7(b), the absorbance at each time point for various H_2O_2 concentration can be obtained. The Michaelis-Menten plot of H_2O_2 concentration is shown in Figure 2-9(b), where $K_m = 22.28 \pm 6.61$ μM. For a small [H_2O_2], the experimental

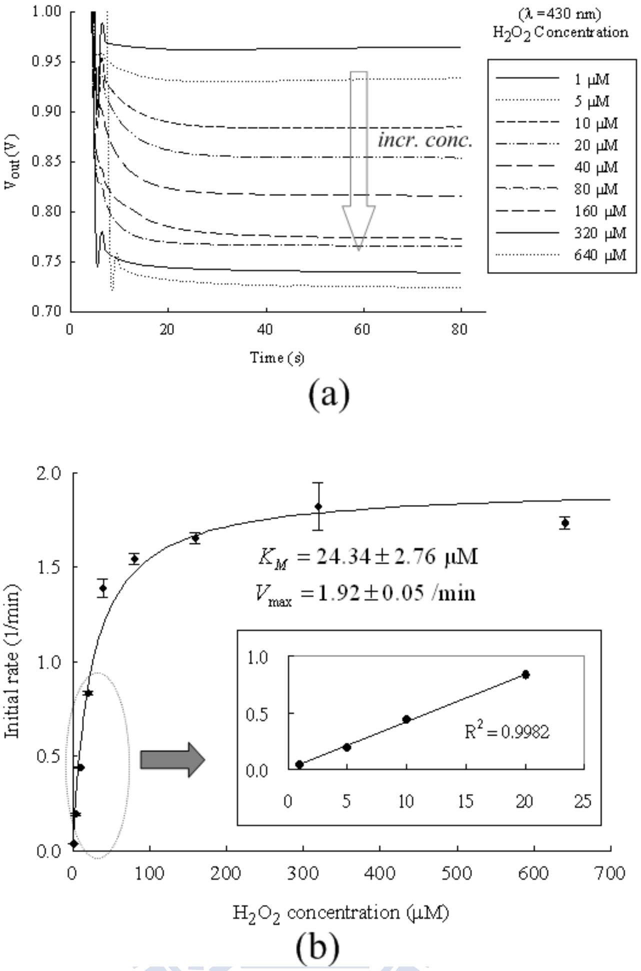

Figure 2-9: Experimental results of the H_2O_2 detection with 430-nm light at 37 °C. (a) Real-time measurement of the output voltage for t = 0–80 s. (b) The Michaelis-Menten plot.

results demonstrate a good linearity with R^2 = 0.9982 as shown in the inset of Figure 2-9(b).

2.3.3 Glucose Detection

The coupled enzymatic reactions for glucose detection are expressed in (2.3) and (2.4). Sufficient ABTS, HRP, and GOx would ensure that the absorbance of the material is proportional to the glucose concentration. For the experiment performed using 650-nm light and R_F = 1 MΩ, the real-time measured voltages V_{out} under various glucose concentrations are illustrated in Figure 2-10(a). The minimum glucose concentration was successfully detected as 10 μM. The Michaelis-Menten plot of glucose concentration is

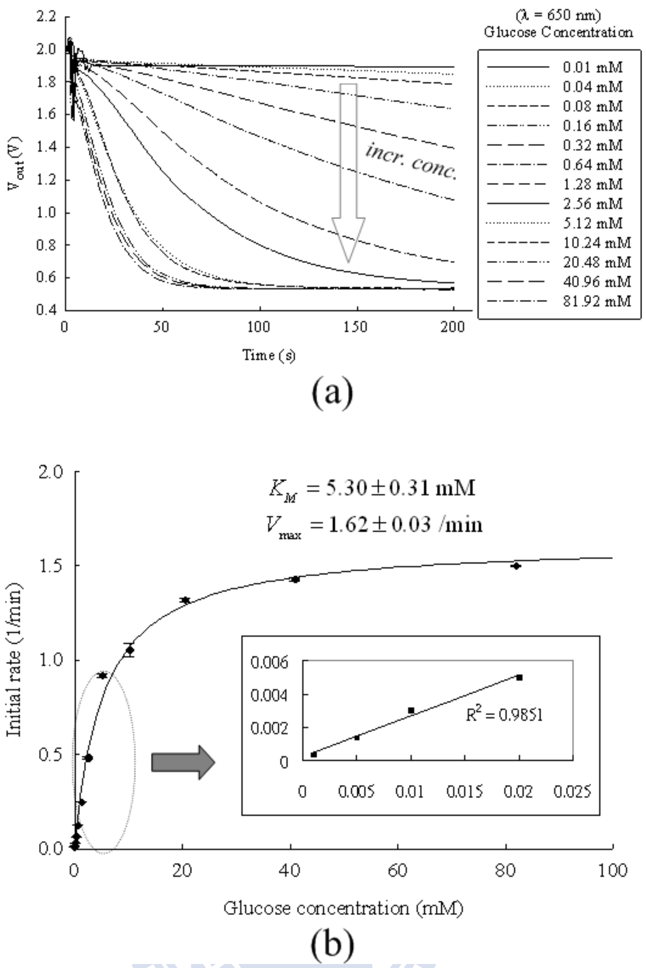

Figure 2-10: Experimental results of the glucose detection with 650-nm light at 25 °C. (a) Real-time measurement of the output voltage for $t = 0\text{–}200\ s$. (b) The Michaelis-Menten plot.

shown in Figure 2-10(b), where $K_m = 4.87 \pm 0.99$ mM. In order to detect a lower glucose concentration, the experiment was then performed using $R_F = 10$ MΩ. The obtained Michaelis-Menten plot is shown in the inset of Figure 2-10(b), where $R^2 = 0.9851$, and the detection limit of the glucose concentration was improved to 1 μM. This detection limit is two orders of magnitude better than the limit reported in previous literatures (about 500 μM) [4], [5], and is comparable to the limit obtained from a commercial spectrophotometer (Hitachi U-3310).

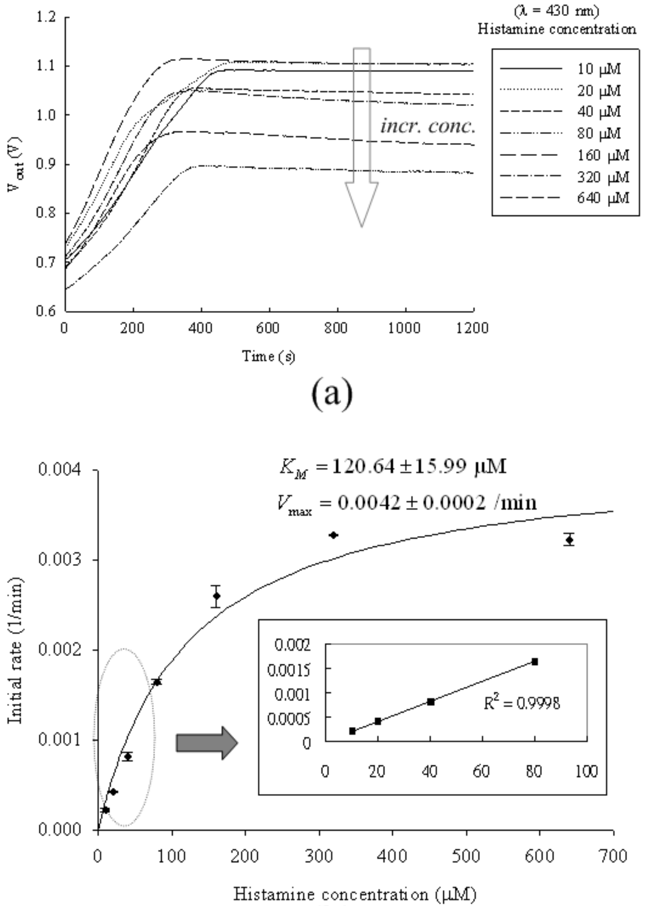

(a)

(b)

Figure 2-11: Experimental results of the histamine detection with 430-nm light at 37 °C. (a) Real-time measurement of the output voltage for t = 0–1200 s. (b) The Michaelis-Menten plot.

2.3.4 Histamine Detection

The coupled enzymatic reactions for histamine detection are expressed in Equations (2.3) and (2.5). Sufficient ABTS, HRP, and DAO would ensure that the absorbance of the material is proportional to the histamine concentration. For the experiment performed using 430-nm light and $R_F = 10$ MΩ, the real-time measured voltages V_{out} under various histamine concentrations are illustrated in Figure 2-11(a). The minimum histamine concentration was successfully detected as 10 μM, which is comparable to the limit obtained from a commercial spectrophotometer (Hitachi U-3310). The Michaelis-Menten plot of histamine concentration is shown in Figure 2-11(b), where $K_m = 125.04 \pm 30.17$ μM. For a diluted histamine solution, the experimental results demonstrate a good linearity with $R^2 = 0.9998$ as shown in the inset of Figure 2-11(b).

2.3.5 Interfering Agents

For the ABTS/H_2O_2/HRP system, although HRP, GOx, and DAO are highly specific enzymes, some chemicals in the blood may affect the H_2O_2 detection. Among the possible interfering agents in the blood, uric acid and acetaminophen were observed to have limited effects on the H_2O_2 detection, whereas ascorbic acid (AA) would somewhat affect the H_2O_2 detection [29]. For healthy adults, the physiological concentration of AA in the blood is about 60 μM, and the glucose concentration in the blood is about 3–8 mM [30], i.e. the ratio of [AA] to [H_2O_2] is about 0.01. Since the sensitivity of our system for glucose detection is in the low μM range, the blood sample could be diluted to a 10^{-2} to 10^{-3} concentration for detection.

To investigate the effects of AA upon the ABTS/H_2O_2/HRP system, the experiments were performed using 10 μM H_2O_2 and various AA concentrations in the reaction mixture. The activity of HRP was determined using the system with 650-nm light and $R_F = 1$ MΩ, and the experimental results are shown in Figure 2-12. For [H_2O_2] = 10 μM and [AA] < 1 μM, the variation in the absorbance A of the reaction mixture was negligible. For [H_2O_2] = 10 μM and [AA] > 3 μM, the significant interference with the ABTS/H_2O_2/HRP system due to the large AA concentration can be observed. However, when the diluted blood sample of a healthy adult is used in our detection system, the ratio of [AA] to [H_2O_2] is about 0.01 and the expected AA concentration is much less than 1 μM. Therefore, the interference from AA is also negligible for the blood examination.

2.4 Summary

An optical biosensing system based on a standard CMOS technology and absorption photometry has been presented. The whole system was assembled into a compact prototype, in which the CMOS biochip composed of a photodiode and a TIA demonstrated a high sensitivity and linearity. The quantum efficiency of the P^+/N_{well} photodiode was enhanced by adopting the interdigitated structure and removing the passivation layers in the CMOS structure. In addition, the switchable feedback resistance of the TIA allowed a user to adjust the amplification factor and the dynamic range for examining different concentration levels of an analyte. The ABTS/H_2O_2/HRP method was introduced as a useful basis for quantifying various analytes by coupling them with biochemical reactions

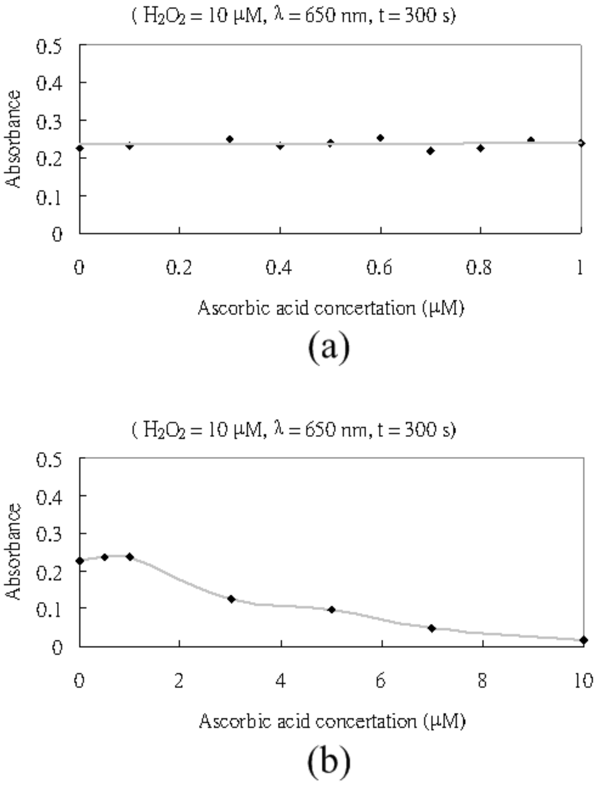

Figure 2-12: The absorbance A of the reaction mixture versus the AA concentration. (a) At low concentration. (b) At high concentration.

that produce H_2O_2. The experimental results reveal that the detection limits of H_2O_2, glucose, and histamine concentration are 1 μM, 1 μM, and 10 μM, respectively. The detection limits are at least one order of magnitude better than those of reported CMOS biosensors, and are even comparable to those of a commercial spectrophotometer.

The whole system exhibits a high detection capability, a large dynamic range, a high reproducibility, a short response time, and a low sample volume requirement. Therefore, the development of this CMOS biosensing system is a stepping stone toward a portable, reliable, inexpensive, and convenient home care instruments. In the future, more advanced functions such as rapid screening and automatic monitoring could be realized, and a practical miniature instrument for personalized clinical diagnosis may be reasonably expected.

Chapter 3

Ring-Shaped Phototransistors for Biomedical Applications

3.1 Introduction

A conventional CMOS photodiode can easily be formed by utilizing a single $\mathrm{N^+/P_{well}}$, $\mathrm{P^+/N_{well}}$, or $\mathrm{N_{well}/P_{sub}}$ junction, but the responsivity is low [1]. Avalanche multiplication is a way to bring an internal current gain. However, the demand for high bias voltage also limits its use in many applications. Circumventing this difficulty, a CMOS phototransistor could have a current amplification under moderate bias through the internal transistor action [31].

In this research, a high-sensitivity phototransistor manufactured in a standard CMOS technology is proposed [32]. Based on this phototransistor, a miniature optical biosensing system is developed. The optoelectronic measurements and biochemical experiments are also presented.

3.2 Principles and Methods

3.2.1 Absorption Photometry

The absorbance A of the materials is described by the Beer-Lambert law [6]

$$A = -\log\left(\frac{I}{I_0}\right) = \epsilon_\lambda \cdot l \cdot c \quad \Longrightarrow A \propto c \tag{3.1}$$

where I_0 and I respectively denote the initial light intensity and the light intensity after passing through the material, ϵ_λ is the wavelength-dependent molar absorptivity in units of $\mathrm{l\cdot mol^{-1}\cdot cm^{-1}}$, l is the path length in units of cm, and c is the concentration of absorbing species in the material in units of M ($1\ \mathrm{M} = 1\ \mathrm{mol\cdot l^{-1}}$). When the light source and the path length are fixed, the absorbance would be proportional to the analyte concentration. Therefore, detecting the optical signals modulated by the biochemical reactions is an efficient way to quantitate the analyte of interest.

Regarding a commercial spectrophotometer, the used sample volume and the path length are about 1 ml and 1 cm, respectively. Referring to (3.1), when a shorter path length is used, the change in the absorbance becomes smaller, which makes the detection of concentration more difficult. For a miniature system, in order to further reduce the sample volume as well as the path length, the development of a high-sensitivity optical sensor is of great importance.

3.2.2 Biochemical Reaction

Horse-radish peroxidase (HRP) is a popular enzyme that has been widely used in biochemical applications. While an antibody is used to recognize a target protein of interest, HRP can be conjugated to the antibody to serve as a label for determining the amount of the target [33]. HRP is usually used combining with hydrogen peroxide (H_2O_2) to oxidize an added substrate that is luminescent or chromogenic. Reported optical methods for HRP detection include the luminol/H_2O_2/HRP reaction [4], the ABTS/H_2O_2/HRP reaction [21], and the TMB/H_2O_2/HRP reaction [34]. The end products of these reactions can either emit or absorb the light of specific wavelengths for analysis.

The TMB/H_2O_2/HRP reaction is adopted as the basis for biomedical applications in our system. TMB stands for 3,3',5,5'-tetra-methyl-benzidine. It is neither mutagenic nor carcinogenic [35] and is a widely used reagent for ELISA (enzyme-linked immuno-sorbent assay).

The oxidation of TMB by H_2O_2 with HRP can be easily observed for qualitative analysis. The reactant solution is visually light green, whereas the soluble end product is deep blue. After the addition of sulfuric acid (H_2SO_4) to the media, this reaction would be stopped and result in a yellow product [36]. The process can be expressed as [37]

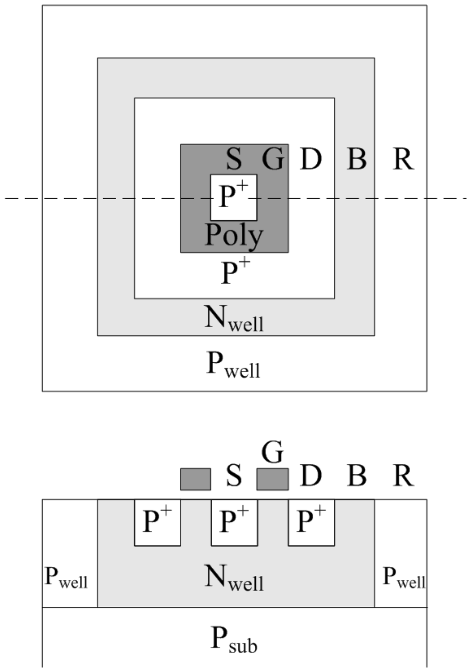

Figure 3-1: The top view and cross section of the PMOS phototransistor.

$$\mathrm{TMB} \xrightarrow{\mathrm{H_2O_2\ +\ HRP}} \mathrm{TMB}^{+} \xrightarrow{\mathrm{H_2SO_4}} \mathrm{TMB}^{2+} \tag{3.2}$$

For quantitative analysis, the analyte concentration can be evaluated by detecting the optical absorbance of the solution. The absorption spectra obtained from a standard spectrophotometer (Hitachi U-3310) show that the reactant TMB has an absorption peak at 280 nm, whereas the blue product TMB^+ has absorption peaks at 370 nm and 650 nm. With the presence of H_2SO_4, the yielded yellow product TMB^{2+} has an absorption peak at 450 nm.

3.2.3 Ring-Shaped Phototransistor

The top view and cross section of the proposed PMOS phototransistor are shown in Figure 3-1. The P^+ source placed in the center is surrounded by the polysilicon gate and the P^+ drain, while the $\mathrm{N_{well}}$ bulk (B) is enclosed by the $\mathrm{P_{well}}$ ring (R). It can be regarded as a PMOS with a photodiode connected across the bulk (B) and the square ring (R).

The PMOS phototransistor leaves the $\mathrm{N_{well}}$ bulk floating and uses the $\mathrm{N_{well}}/\mathrm{P_{sub}}$ junction diode for the optical access [38]. The photogenerated carriers driftting into the $\mathrm{N_{well}}$ would change the bulk potential, and thereby change the threshold voltage as well as the output drain current.

The output drain current I_D of a MOSFET operated in the saturation region can be expressed as

$$I_D = \frac{1}{2}\frac{W}{L}\mu C_{\mathrm{ox}}\left(V_{GS} - V_T\right)^2\left(1 + \frac{V_{DS}}{V_A}\right) \tag{3.3}$$

where W, L, μ, C_{ox}, V_{GS}, V_T, V_{DS}, and V_A are the channel width, the channel length, the carrier mobility, the oxide capacitance per unit area, the gate-source voltage, the threshold voltage, the drain-source voltage, and the Early voltage, respectively [31]. The shift amount of the threshold voltage due to the bulk charge effect is given by

$$\Delta V_T = \frac{\sqrt{2\varepsilon_s q N_B}}{C_{\mathrm{ox}}}\left(\sqrt{2\psi_B + V_{SB}} - \sqrt{2\psi_B}\right) \tag{3.4}$$

where ε_s, q, N_B, and ψ_B are the permittivity of silicon, the unit electric charge, the doping concentration of the bulk, and the bulk Fermi level from the intrinsic Fermi level, respectively; V_{SB} is the source-bulk voltage resulting from the optical access.

Using the proposed layout style, the sensing area of the outer ring photodiode is enlarged, so as to cause a larger shift amount of the threshold voltage. The channel length is also smaller than that of a conventional PMOS with the same area. Since the output drain current is inversely proportional to the channel length, a larger photocurrent response could be expected.

3.2.4 Biosensing System Setup

The proposed PMOS phototransistor with area of 100 μm × 100 μm was manufactured using the TSMC (Taiwan Semiconductor Manufacturing Company) 0.35-μm standard CMOS technology. The photograph and the illustrated diagram of the whole biosensing system are shown in Figure 3-2, and its dimensions are about 7 cm (length) × 5 cm (width) × 5 cm (height). A red LED (Centenary 31134) is used as the light source, and a slide is placed above the PMOS phototransistor to hold the biochemical sample. A sample volume of only 10 μl is required for the detection. The path length l through the sample is about 0.1 cm.

The light travelling through the sample is partially absorbed and then detected by the PMOS phototransistor, which converts the transmitted optical signals into current signals. The current signals are measured using a precision semiconductor parameter

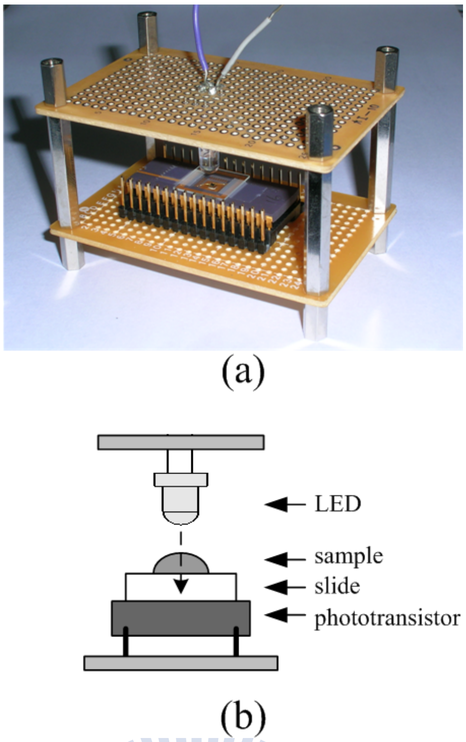

Figure 3-2: The phototransistor-based biosensing system: (a) photogragh and (b) illustrated diagram.

analyzer (HP 4156A), which is connected to a personal computer via a general purpose interface bus (GPIB). An application software (Interactive Characterization Software, ICS) is used for data acquisition.

3.2.5 Preparation of Biochemical Reagents

The biochemical experiments were assisted by Prof. Yuh-Shyong Yang's group. TMB liquid substrate system, HRP-streptavidin, and phosphate buffered saline (PBS) powders were purchased from Sigma. Other chemical reagents were of analytical grade and used without further purification.

The HRP stock solutions ($1\mu g/\mu l$) were prepared in a PBS buffer and stored at -20 °C. The stock enzyme solutions were melted in an ice bath just before use and diluted with double distilled water (ddH_2O). The reactions were performed at 25 °C.

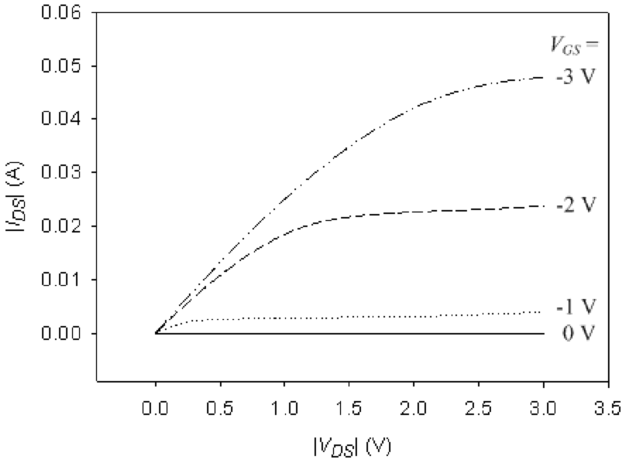

Figure 3-3: The measured *I*-*V* charateristics of the PMOS phototransistor.

3.3 Experimental Results

3.3.1 Device Characteristics

While the proposed PMOS phototransistor was without illumination, the measured *I*-*V* characteristics are shown in Figure 3-3. The bias conditions were as follows: the source was grounded, the drain voltage swept from 0 V to -3 V, the gate voltage stepped from 0 V to -3 V, the bulk was floating, and the ring voltage was fixed at -3 V. It can be seen that for $V_{DS} = -3$ V, the phototransistor was operated in the saturation region. The larger $|V_{GS}|$ was, the larger $|I_{DS}|$ was.

While the phototransistor was illuminated, the output drain current varied in response to the light intensity. For $V_{DS} = -3$ V, the measured photocurrent responses under various illumination intensities of 650-nm light are shown in Figure 3-4(a). The photocurrent response divided by illumination intensity can give the responsivity, and the results are shown in Figure 3-4(b). For $V_{GS} = -2$ V and -3 V, the phototransistor exhibited a responsivity higher than 1000 A/W. The responsivity is 2000 folds higher than that of a traditional silicon P/N junction photodiode (about 0.5 A/W) [2].

Even for very small bias voltages such as $V_{DS} = -0.1$ V and $V_{GS} = 0$ V, the phototransistor can successfully detected the change of illumination intensity and exhibited a responsivity of about 50 A/W.

Two measurements with an interval of four months were performed, and the device

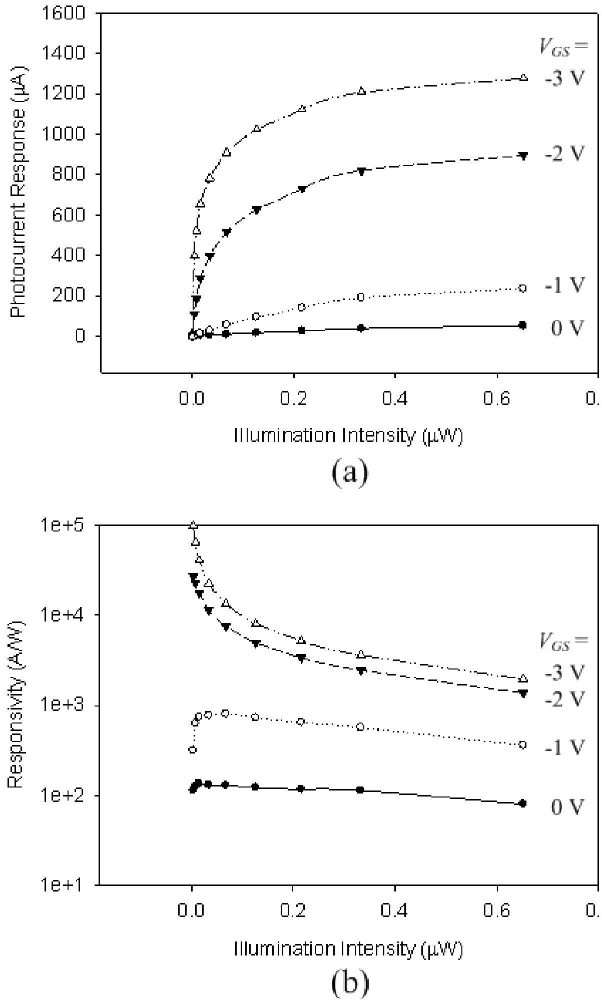

Figure 3-4: The optoelectronic characteristics of the PMOS phototransistor for $V_{DS} = -3$ V with various V_{GS}: (a) photocurrent response versus illumination intensities and (b) responsivity versus illumination intensities.

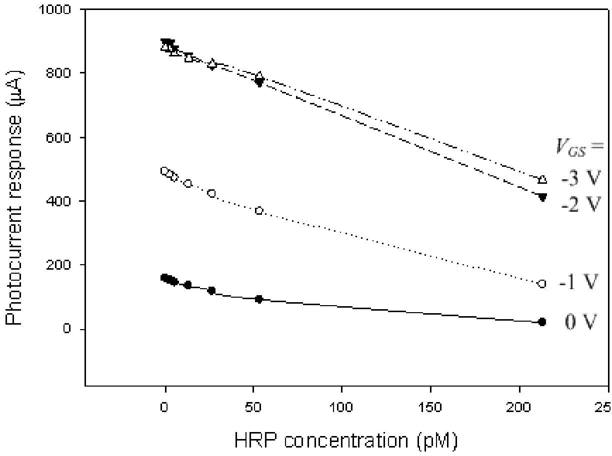

Figure 3-5: The photocurrent response versus HRP concentration for $V_{DS} = -3$ V with various V_{GS}.

dark current were observed to examine the device stability. For $V_{DS} = -3$ V and $V_{GS} = -2$ V, the drift amount of dark current after four months was 29.2 μA, which is much smaller than the amplitude of photocurrent response (at least hundreds μA). For $V_{DS} = -0.1$ V and $V_{GS} = 0$ V, the drift amount of dark current after four months was 0.75 nA, which is also much smaller than the amplitude of photocurrent response (at least hundreds nA). Hence the stability of the proposed PMOS phototransistor could be acceptable.

3.3.2 HRP Detection

The system setup is illustrated in Figure 3-2. A sample volume of only 10 μl was required to be dropped on the slide above the phototransistor. For the experiments performed using 650-nm light with different HRP concentrations, the measured photocurrent responses for $V_{DS} = -3$ V with various V_{GS} are shown in Figure 3-5. The used HRP concentration values were 0.0, 2.7, 5.3, 13.3, 26.6, 53.2, and 212.8 pM, respectively. Each data point is the average of five measurement results.

For $V_{DS} = -3$ V and $V_{GS} = -2$ V, the highest sensitivity of 2.5 μA/pM was achieved, and the linear relationship ranged from 2.7 pM to 212.8 pM with the coefficient of determination $R^2 = 0.9990$ calculated by an application software (Microsoft Excel). The statistical information of the photocurrent response I_{ph} is summarized in Table 3.1. For the buffer solution, the I_{ph} mean is 901.0 μA and the standard deviation is 1.140 μA. For

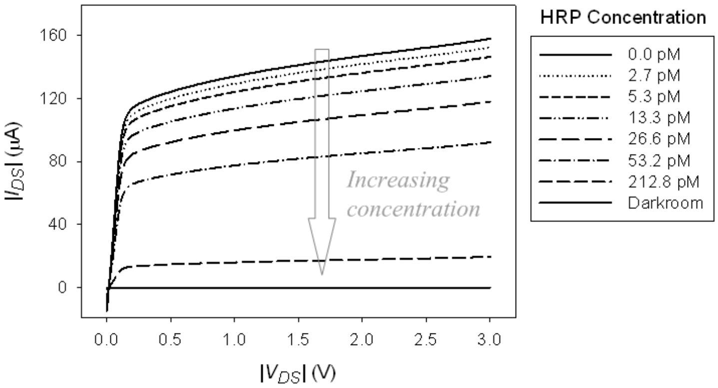

Figure 3-6: The measured I-V characteristics for $V_{GS} = 0$ V under various HRP concentrations.

the 2.7-pM solution, the $I_{\rm ph}$ mean is 893.2 μA and the standard deviation is 2.510 μA. Since the difference in the $I_{\rm ph}$ mean is much larger than the standard deviation, the experimental results indicated that the minimum HRP concentration successfully detected was 2.7 pM. This detection limit is three orders of magnitude better than that of a lately reported silicon biosensor (2.4 nM) [11], and is even comparable to the limit obtained from a commercial spectrophotometer (Hitachi U-3310). The required sample volume of our system is also smaller.

For $V_{GS} = 0$ V, the phototransistor can still be used for biochemical detection, and the measured I-V characteristics under various HRP concentrations are shown in Figure 3-6, with an arrow indicating the trend of increasing concentration. When the HRP concentration is increasing, the color of the end product become darker, which implies that more light will be absorbed, and thus the output drain current become smaller and closer to the condition in a darkroom. Even for very small bias voltages such as $V_{DS} = -0.1$ V, the experimental results shown in Figure 3-7 also demonstrated a detection limit of 2.7 pM. The difference in $I_{\rm ph}$ mean between the buffer and 2.7-pM solution is 3.1 μA, which is much larger than the standard deviation of 0.1 μA.

To investigate the corresponding absorbances for various HRP concentration solutions, firstly the relationship between the absorbance and the photocurrent response can be obtained by combining (2.1) and Figure 3-4(a), and the results are shown in Figure 3-8(a). Then combining Figure 3-5 and Figure 3-8(a) gives the relationship between the absorbance and HRP concentration. For $V_{DS} = -3$ V and $V_{GS} = -2$ V, the obtained

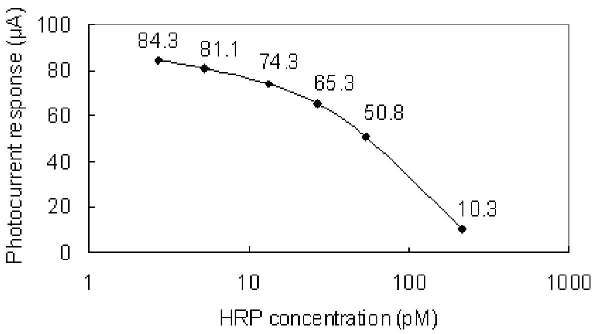

Figure 3-7: The photocurrent response versus HRP concentration for $V_{DS} = -0.1$ V and $V_{GS} = 0$ V.

Table 3.1: The statistical information of the photocurrent response I_{ph} and the absorbance A for $V_{DS} = -3$ V and $V_{GS} = -2$ V under various HRP concentration.

	I_{ph} (μA)		Absorbance	
Conc. (pM)	mean	SD	mean	SD
buffer	901.0	1.140	-0.004	0.002
2.7	893.2	2.510	0.017	0.005
5.3	879.2	1.140	0.054	0.002
13.3	857.4	1.643	0.113	0.004
26.6	826.8	1.924	0.195	0.004
53.2	770.8	1.304	0.346	0.003
218.8	414.8	3.194	1.302	0.007
darkroom	0.0	1.342	2.417	0.003

(Conc.: concentration, SD: standard deviation)

results show that the linear detection range was from 2.7 pM to 212.8 pM with $R^2 = 0.9991$, which is depicted in Figure 3-8(b). The statistical information of the absorbance A is summarized in Table 3.1.

3.4 Applications for Screening Skin-Whitening Agents

3.4.1 Motivation

In recent years, abundant candidates of skin whitening agents have been developed. To screen the efficiency of these whitening agents, much attention has been devoted to the development of convenient biosensors.

Melanin (also called pigment) is a substance that gives the skin its color. Melanocytes

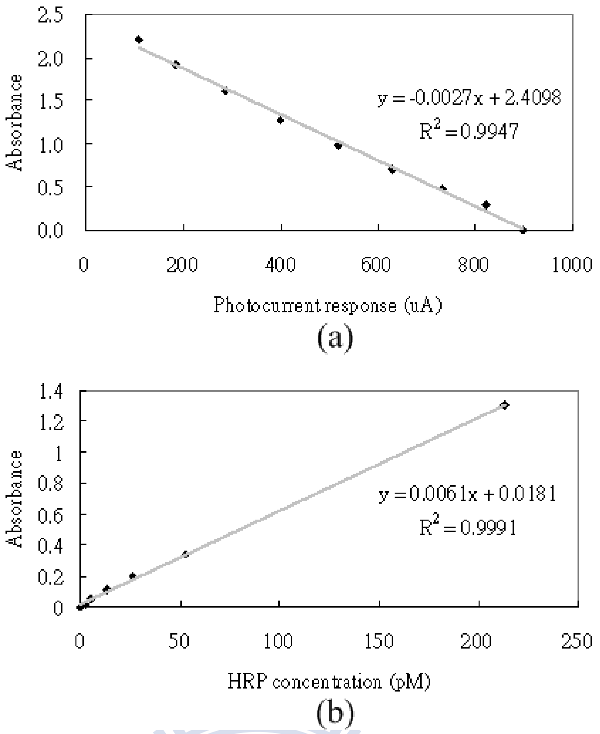

Figure 3-8: The corresponding absorbance versus (a) photocurrent response and (b) HRP concentration.

increase their production of melanin in response to sun exposure, and that would lead to freckles. For skin-whitening agents, the mechanism of melanogenesis suppression could be divided into two categories: the inhibition of melanin production pathway and the decrease of melanocyte proliferation [39], [40].

In this research, three major methods for evaluating effects of skin whitening agents were applied: melanin, MTT, and tyrosinase assays. The schematic diagram of these assays are shown in Figure 3-9. Melanin assay is related to content of melanin product; MTT assay is related to viability of melanoma cells; tyrosinase assay is related to tyrosinase activity.

3.4.2 Materials and Methods

Melanin Assay

Murine melanoma B16-F10 cells (ATCC: CRL-6475) were cultured in DMEM (Dulbecco's modified Eagle's medium) with 10% heat-inactivated fetal bovine serum, 1.5-g/L sodium bicarbonate, 4.5-g/L glucose, and 1% antibiotics. The cells were seeded in 6-well

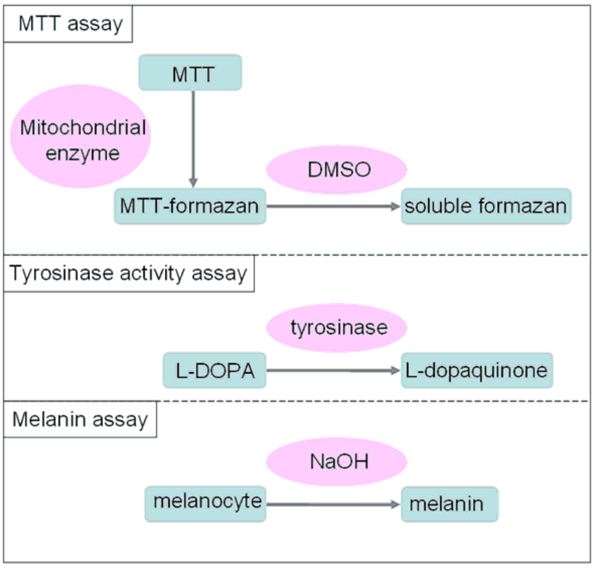

Figure 3-9: The schematic diagram of three major assays for evaluating whitening agents.

plates at densities of 2×10^5, 1×10^5, 5×10^4, and 2.5×10^4 cells/ml, respectively. After the incubation in a 5% CO_2 incubator at 37 °C for 5 hours, cells were digested by 0.25% (w/v) trypsin with 0.52-mM EDTA solution (GIBCO), and washed with PBS (phosphate-buffered saline). Then the supernatant was discarded, and cells were lysed in 200-μl 1-N NaOH at 80 °C for 1 hour. To evaluate the density of cells, the optical absorbance was measured using the CMOS biosensor.

MTT Assay

Murine melanoma B16-F10 cells were cultured and seeded in 6-well plates at several densities. After the incubation in a 5% CO_2 incubator at 37 °C for 5 hours, 800-μl 1-mg/ml MTT [3-(4,5-dimethylthiazol-2-yl)-2,5-diphenyltetrazolium-bromide] solution freshly prepared in PBS was added to each well of cells cultured plate. The cells were incubated at 37 °C for 4 hours, and then 800-μl DMSO (dimethyl sulfoxide) was added to each well to dissolve the purple MTT-formazan. After the incubation at 37 °C for 10 minutes, the optical absorbance was measured using the CMOS biosensor.

Tyrosinase Assay

Murine melanoma B16-F10 cells were cultured and seeded in 6-well plates at several densities. After the incubation in a 5% CO_2 incubator at 37 °C for 3 days, cells were digested by 0.25% (w/v) trypsin with 0.52-mM EDTA solution (GIBCO), and washed with PBS (phosphate-buffered saline). Then the supernatant was discarded, and cells were lysed in 150-μl 0.1-M sodium phosphate buffer (pH6.8) containing 1% Triton X-100 and 0.1-mM PMSF. Then cells were frozen at -20 °C for 30 minutes. After thawing and mixing, cellular extracts were clarified by centrifugation at 12000 rpm for 30 minutes at 4 °C. The 80-μl supernatant and 20-μl 2-mg/ml L-DOPA were placed in 96-well plates. Specific activity was defined as the amount of L-dopaquinone formed per cell. Following the incubation at 37 °C, the optical absorbance was measured using the CMOS biosensor.

Absorption Photometry

The analyte concentration can be quantitated by detecting the optical absorbance of the product solution. The absorption spectra obtained from a spectrophotometer (Hitachi U-3310) show that the products for melanin assay, MTT assay, and tyrosinase assay have absorption peaks at 470 nm, 520 nm, and 550 nm, respectively.

System Setup

The top view and cross section of the proposed CMOS phototransistor are shown in Figure 3-1, and the illustrated diagram and the photograph of the whole biosensing system are shown in Figure 3-2. A green LED (Centenary 36341) with a peak at 520 nm is used as the light source, and a slide is placed above the CMOS phototransistor to hold the biochemical sample. Only a sample volume of 10 μl is required for the detection. The path length through the sample is about 0.1 cm

3.4.3 Experimental Results

Melanin Assay

The experimental I_d-V_d curves of the phototransistor for measuring the melanin assay are shown in Figure 3-10, in which NaOH represents the reference condition without melanocytes. The results indicate that the density of 5×10^4 cells/ml can be successfully detected using the miniature CMOS biosensor.

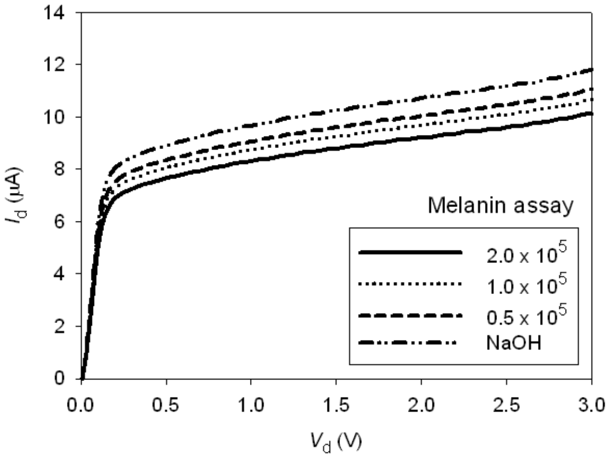

Figure 3-10: The measured I_d-V_d curves for the melanin assay.

MTT Assay

The measured I_d-V_d curves for the MTT assay is shown in Figure 3-11. DMSO is used as the reference without melanocyte. It indicates that the density of 5×10^4 cells/ml can be successfully detected.

Tyrosinase Assay

The measured I_d-V_d curves for the tyrosinase assay is shown in Figure 3-12. H_2O is used as the reference without melanocyte. It indicates that the density of 5×10^4 cells/ml can be successfully detected.

Kojic Acid Effect

Kojic acid is a well-known standard in skin whitening used to evaluate the potency of a new drug candidate. This whitening agent can inhibit the tyrosinase activity and reduce the melanin content without influencing the proliferation of B16-F10 cells. The effects of Kojic acid on these three assays was determined at different concentrations, as shown in Figure 3-13.

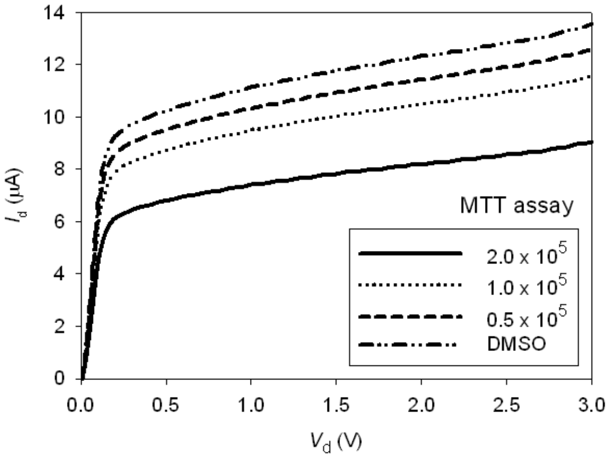

Figure 3-11: The measured I_d-V_d curves for the MTT assay.

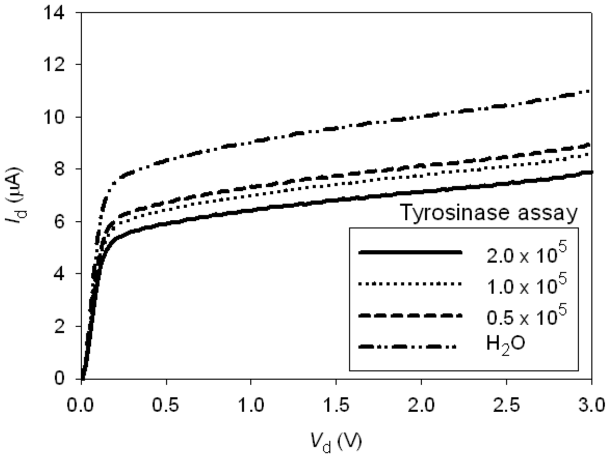

Figure 3-12: The measured I_d-V_d curves for the tyrosinase assay.

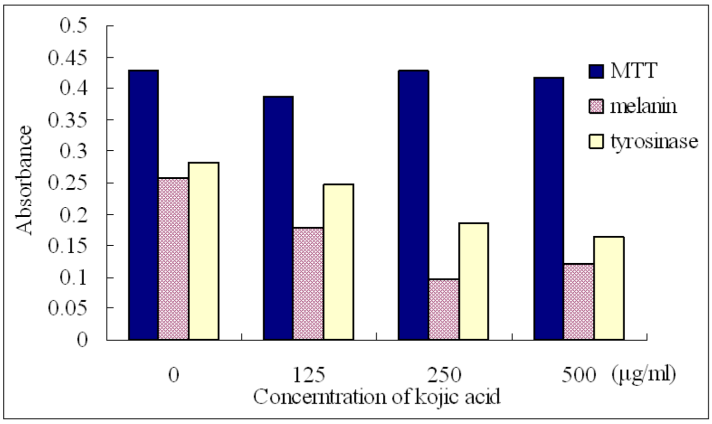

Figure 3-13: The effects of Kojic acid on B16-F10 cells for melanin, MTT, and tyrosinase assays.

3.5 Applications for Ultra-Violet Detection

3.5.1 Motivation

The development of a photodetector with high responsivity for the UV/blue spectral range has attracted much interest for many applications [8], [21], [41], [42]. For biochemical analysis, the detection of the optical properties changed by chemical reactions is a competent approach to examine various important biological molecules. Through the chemical reactions, the change of the emitted- or absorbed-light intensity is generally less than 1 μW. Regarding the reported methods, the luminol/H_2O_2/HRP reaction involves the emission of 425-nm light [8], and the ABTS/H_2O_2/HRP reaction involves the absorption of 415-nm light [21].

Much work has been devoted to the realization of photodetectors using a standard CMOS technology or CMOS-compatible technologies in the last decade [41]–[49]. The responsivity of a conventional CMOS photodiode for the UV/blue spectral range is low (about 0.2 A/W) [2]. Circumventing this drawback, a phototransistor can have a current amplification under moderate bias through the internal transistor action [31]. However, little work has been conducted on the phototransistor manufactured using a standard CMOS technology for the UV/blue spectral range.

In this research, the proposed CMOS phototransistor exhibited an enhanced responsivity for the UV/blue spectral range.

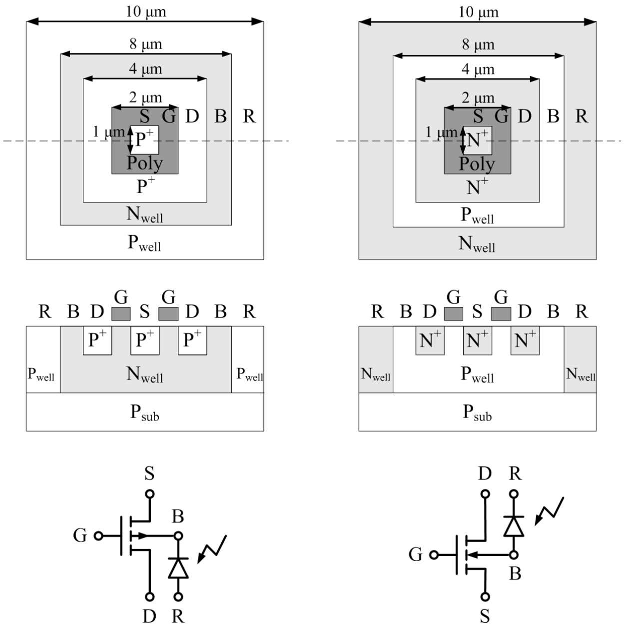

(a) (b)

Figure 3-14: The top view, cross section, and equivalent symbol of the proposed (a) PMOS phototransistor and (b) NMOS phototransistor.

3.5.2 Operating Principle

The device structures of the proposed PMOS and NMOS phototransistor based on CMOS technology are shown in Figs. 3-14(a) and 3-14(b), respectively. For the PMOS phototransistor, the P^+ source is placed in the center with the ring-shaped poly-silicon gate and P^+ drain, while the N_{well} bulk (B) is enclosed by the P_{well} ring (R). For the NMOS phototransistor, the N^+ source is placed in the center with the ring-shaped poly-silicon gate and N^+ drain, while the P_{well} bulk (B) is enclosed by the N_{well} ring (R). In both cases, the phototransistor can be regarded as a MOSFET with a photodiode connected across the bulk (B) and the square ring (R), as shown in Figure 3-14.

Serving as an optical sensor, the phototransistor leaves the bulk floating and mainly uses the N_{well}/P_{well} junction to separate photogenerated electron-hole pairs [46]. The photogenerated carriers drifting into the bulk would change the bulk potential, and thereby change the threshold voltage as well as the output drain current.

For the UV/blue incident light, most photogenerated carriers are very close to the surface (within 0.2 μm). Using the proposed ring-shaped layout style, the near-surface depletion region of the outer N_{well}/P_{well} ring-shaped photodiode is enlarged and superior to that of a conventional MOSFET with the same area, so as to cause a larger shift amount of the threshold voltage. Hence a larger photocurrent response I_{ph} could be expected.

Regarding the proposed phototransistors, the bulk is left floating, while the applied fixed ring-source voltage V_{RS} is negative for PMOS and is positive for NMOS. The bulk-ring voltage V_{BR} resulting from the illumination can be described by the transposed diode equation [31]

$$V_{BR} = V_{th} \ln \left(1 + \frac{I_{BR(ph)}}{I_{BR0}} \right) = V_{th} \ln \left(1 + \frac{k_1 P_{\text{opt}}}{I_{BR0}} \right) \tag{3.5}$$

where V_{th}, $I_{BR(ph)}$, I_{BR0}, and P_{opt} are the thermal voltage, the photocurrent of the bulk-ring diode, the saturation current of the bulk-ring diode, and the incident optical power density, respectively; k_1 is functions of material parameters, transistor bias voltages, and the depletion region area of the $\text{N}_{\text{well}}/\text{P}_{\text{well}}$ junctions. Thus the resulted bulk-source voltage V_{BS} can be expressed as $V_{BS} = V_{BR} + V_{RS}$. For illuminated PMOS, V_{BS} is negative since its N_{well} bulk accumulates excess electrons; for illuminated NMOS, V_{BS} is positive since its P_{well} bulk accumulates excess holes.

The shift amount of the threshold voltage ΔV_T due to the bulk charge effect is given by [31]

$$\Delta V_T = \frac{\sqrt{2\varepsilon_s q N_B}}{C_{\text{ox}}} \left(\sqrt{2\psi_B - V_{BS}} - \sqrt{2\psi_B} \right) \tag{3.6}$$

where ε_s, q, N_B, C_{ox}, and ψ_B are the permittivity of silicon, the unit electric charge, the doping concentration of the bulk, the oxide capacitance per unit area, and the bulk Fermi level from the intrinsic Fermi level, respectively. When PMOS and NMOS phototransistors are illuminated, the absolute value of the threshold voltage $|V_T|$ will both become smaller.

The photocurrent response I_{ph} is the difference in the output drain current, which can be expressed as

$$I_{\text{ph}} = |I_D - I_{D0}| \tag{3.7}$$

where I_D and I_{D0} denote the output drain current of the phototransistor with and without illumination, respectively. It implies that I_{ph} of the phototransistor will increase with the $\text{N}_{\text{well}}/\text{P}_{\text{well}}$ sensing area A, the channel aspect ratio W/L, and the bias voltages $|V_{GS}|$ and $|V_{DS}|$.

Overall, with advantages of the ring-shaped structure and the MOSFET amplification,

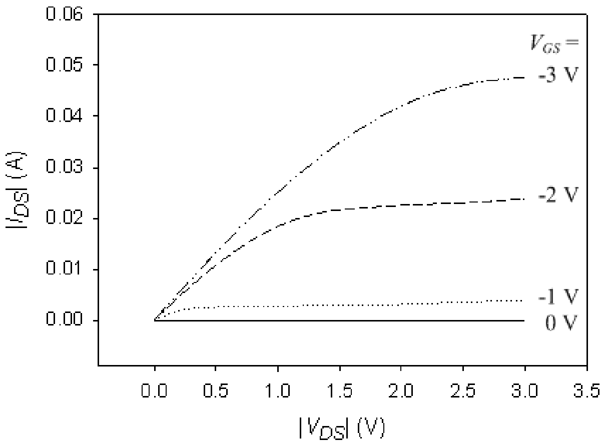

Figure 3-15: The measured *I*-*V* characteristics of the PMOS phototransistor without illumination.

the proposed CMOS phototransistor is expected to perform a better responsivity than conventional CMOS-based photodetectors.

3.5.3 Experimental Results

The proposed PMOS and NMOS phototransistors were respectively duplicated and concatenated to form each 10 × 10 array with a total area of 100 μm × 100 μm, and they were manufactured using the TSMC (Taiwan Semiconductor Manufacturing Company) 0.35-μm standard CMOS technology. To characterize these phototransistors, a UV/blue LED (Centenary 40327) with the peak of 400 nm was used as the light source, while its light intensity was adjusted by a power supply (Agilent E3631A). A reference photodetector and a pinhole were introduced to measure the optical power density for various bias voltages applied to the LED. A precision semiconductor parameter analyzer (HP 4156A) and a test fixture (HP 16058A) were used to characterize the CMOS photodetectors.

Figure 3-15 shows the measured *I*-*V* characteristics of the PMOS phototransistor without illumination. The bias conditions were as follows: the source was grounded, the drain voltage swept from 0 V to -3 V, the gate voltage stepped from 0 V to -3 V, the bulk was floating, and the ring voltage was fixed at -3 V.

While the phototransistors were illuminated, the output drain current varied in response to the light intensity. For the PMOS phototransistor with $|V_{DS}| = 3$ V, the measured photocurrent responses are shown in Figure 3-16(a). The larger $|V_{GS}|$ was,

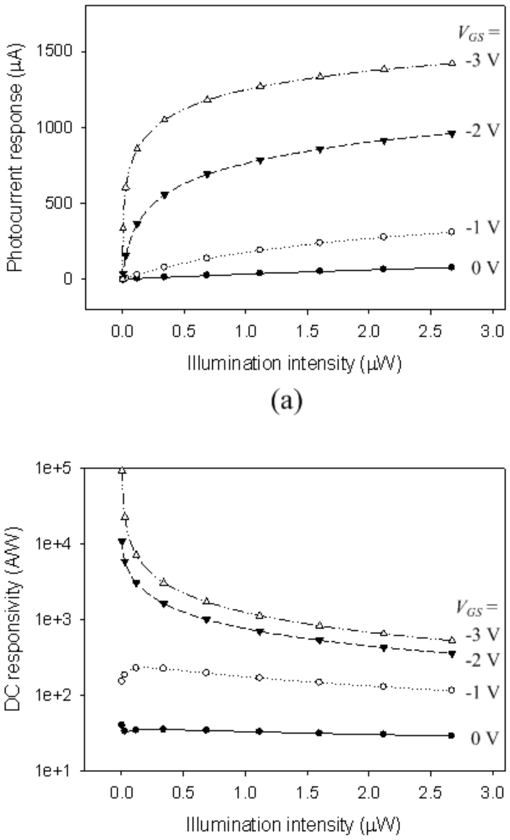

(a)

(b)

Figure 3-16: The optoelectronic characteristics of the PMOS phototransistor for $V_{DS} = -3$ V with various V_{GS}: (a) photocurrent response versus illumination intensities and (b) DC responsivity versus illumination intensities.

the larger $|I_D|$ as well as I_{ph} were. The photocurrent response divided by illumination intensity gives the DC responsivity, and the results are shown in Figure 3-16(b). With $V_{GS} = -3$ V, the phototransistor exhibited a responsivity higher than 1500 A/W when the illumination intensity was less than 1 μW, as the condition for applications in most biochemical detection. This responsivity is 7500 folds higher than that of a conventional silicon P/N junction photodiode (about 0.2 A/W) [2]. In addition, when the illumination intensity was about 0.1 μW, a higher responsivity of 7200 A/W can be achieved.

Even for very small bias voltages such as $V_{GS} = V_{DS} = -0.1$ V, the phototransistor can successfully detect the change of illumination intensity and exhibited a responsivity of about 17.9 A/W. The dark current was less than 1 nA.

Table 3.2 summarizes the measured responsivities for the PMOS and NMOS phototransistors under various bias conditions ($V_{GS} = V_{DS}$) with illumination of 0.7-μW 400-nm light. The characteristics of other reported photodetectors manufactured in a standard CMOS technology are also compared [47]–[49]. The difference between the PMOS and NMOS phototransistor mainly results from that the N_{well} bulk of PMOS is distinguished from P_{sub}, whereas the NMOS has a larger bulk region since P_{well} is inherently connected with P_{sub}. For further applications in integrated circuits or sensor arrays, the floating P_{well} of NMOS phototransistor can be separated from the P_{sub} by introducing a deep-N_{well}. Among these CMOS photodetectors, the proposed phototransistor exhibits a higher responsivity but at the expense of bandwidth. The measured dynamic responsivities for 1 Hz, 1 kHz, and 1 MHz were about 1700, 800, and 600 A/W, respectively. However, the bandwidth is sufficient for applications in biochemical analysis.

3.6 Summary

Based on absorption photometry and a PMOS phototransistor manufactured in a standard CMOS technology, a high-sensitivity biosensing system has been presented. The whole system was assembled into a compact prototype, and the TMB/H_2O_2/HRP reaction which absorbs 650-nm light was adopted as the basis for biomedical applications in our system. This system exhibited a high detection capability of 2.5 μA/pM, a great detection limit of 2.7 pM, a large linear detection range from 2.7 to 212.8 pM, and a low required sample volume of 10 μl.

Table 3.2: The UV/blue responsivity of the CMOS photodetectors.

Device Type	Ref.	λ (nm)	Bias (V)	R (A/W)
Conventional PD	[47]	400	3	0.23
NPN PT	[48]	420	5	0.25
Avalenche PD	[49]	380	14.5	5.3
PMOS PT	This work	400	0.1	17.9
			1	1100
			2	1700
			3	1700
NMOS PT	This work	400	0.1	2.3
			1	2600
			2	2900
			3	1500

(PD: photodiode, PT: phototransistor)

This high-sensitivity miniature CMOS biosensor is also employed for the investigation of whitening mechanisms using 520-nm light. Three assays (Melanin, MTT, and tyrosinase) were performed, and the effect of the whitening agent kojic acid is examined. Experimental results demonstrated that the density of 5×10^4 cells/ml can be successfully detected for these assays, and indicated that the miniature CMOS phototransistor platform can be developed to a portable and high-throughput system for the evaluation of the whitening reagent in the popular cosmetic industry.

In addition, this ring-shaped phototransistor is applied to the UV/blue spectral range with a high responsivity. Experimental results demonstrated that the responsivity for 400-nm light was higher than 1500 A/W, which is also superior to that of other reported photodetectors manufactured in a standard CMOS process. Even for very small bias voltages such as 0.1 V, the phototransistor can exhibit a responsivity of 17.9 A/W. The proposed device structure is therefore an attractive option in applications for the UV/blue spectral range.

Chapter 4

Spatially-Modulated Photodiodes for High-Speed Applications

4.1 Introduction

In order to further improve the frequency response, we propose two enhanced layout style, named square-shaped SMPD and meshed SMPD, to increase the sidewall depletion regions and to subtract the substrate current more effectively than other CMOS photodetectors. The characteristics of these SMPDs using various P/N junctions are also analyzed in detail.

4.2 Device Structure and Operation Mechanism

The device structure of the square-shaped SMPD and meshed SMPD adopting $\mathrm{N_{well}}/\mathrm{P_{sub}}$ junctions are illustrated in Figs. 4-1(a) and 4-1(b), respectively. Here, the x-axis is the direction perpendicular to the surface. L_1, D_1, and L_2 indicate the thicknesses of the neutral $\mathrm{N_{well}}$ region, the depletion region, and the neutral $\mathrm{P_{sub}}$ region, respectively. W_P, W, and w' represent the widths of the unit cell, the $\mathrm{N_{well}}$ region, and the neutral $\mathrm{N_{well}}$ region, respectively. As shown in the figure, several equal minimal areas of $\mathrm{N_{well}}$ with these square shapes are placed with the optimum spacing between each other, on the premise that the depletion regions of adjacent cells are in direct contact with each other. The dark areas represent the regions of the shaded junction diodes, which are covered with floating metals as optical masks, and the rest areas represent the regions of the unshaded

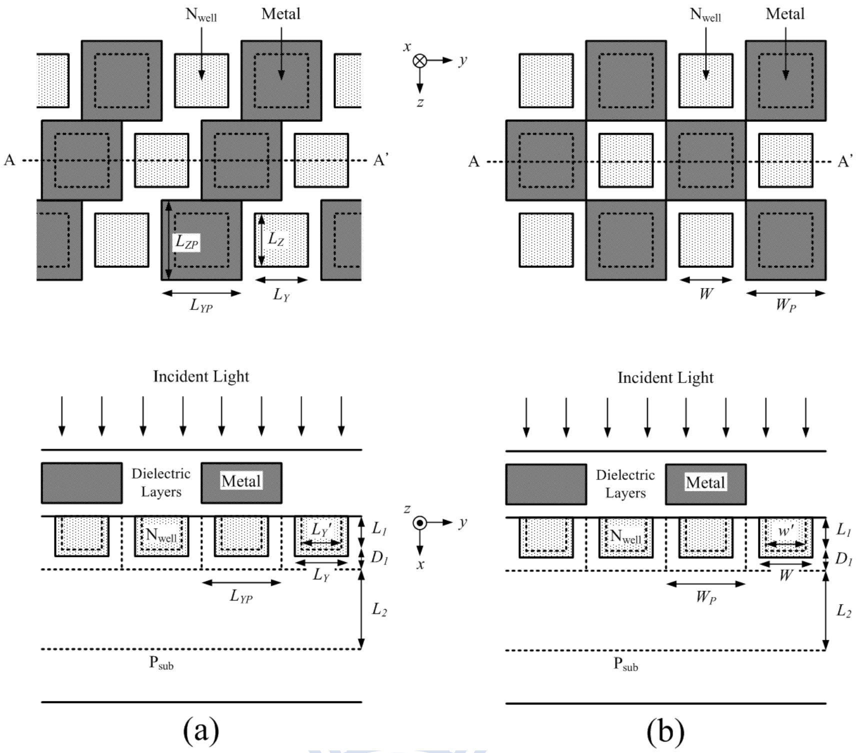

Figure 4-1: The top view and cross section of (a) the $N_{\text{well}}/P_{\text{sub}}$ square-shaped SMPD and (b) the $N_{\text{well}}/P_{\text{sub}}$ meshed SMPD.

junction diodes, which allow the incident light to penetrate into the silicon substrate.

When the $N_{\text{well}}/P_{\text{sub}}$ SMPD is illuminated, optical excitations only occur in the unshaded junction diodes, which can be further divided into three regions: depletion regions, neutral P_{sub} regions, and neutral N_{well} regions. (i) In the depletion regions, the photogenerated carriers contribute to the drift current and do not significantly degrade the frequency response. (ii) In the neutral P_{sub} regions, the photogenerated carriers have a chance to diffuse toward the adjacent shaded junction diodes. The time required for these carriers to diffuse upwardly to the depletion regions limits the total frequency response. Accordingly, the unshaded junction diodes provide the relatively immediate current (I_{imm}), and the shaded junction diodes provide the relatively deferred current (I_{def}). If the latter is subtracted from the former, the slow diffusion response resulting from the substrate current can be eliminated [18]. Therefore, the SMPD is much faster than the individual junction diodes. (iii) In the neutral N_{well} regions, the photogenerated carriers also require a long time to diffuse toward the depletion region. By reducing the photogenerated carriers in the neutral N_{well} region, the total frequency response can be improved further. The proposed SMPD structures are aimed to effectively shrink the neutral $\mathrm{N_{well}}$ region and extend the depletion region. As a result, the total photocurrent consists mostly of the drift current, and the frequency response is improved.

The layout topologies of the SMPD adopting $\mathrm{N^+/P_{well}}$ or $\mathrm{P^+/N_{well}}$ junctions are analogous to Figure 4-1, except that the doping type and the doping concentration are changed.

4.3 Theoretical Analysis of the Photocurrent

4.3.1 General Considerations

For the unshaded area, the incident photon flux density in the frequency domain $(s = jw)$ can be expressed as [31]

$$\Phi_0(s) = \frac{P_{opt}(s)}{A}\frac{\lambda}{hc}(1-R) \tag{4.1}$$

where $P_{opt}(s)$, A, λ, h, c, and R represent the input optical power, the device area, the wavelength of the incident light, the Plank's constant, the speed of light, and the reflectance, respectively. The electron-hole generation rate $G(x, s)$ from optical excitation is given as

$$G(x, s) = \alpha\Phi_0(s)e^{-\alpha x} \tag{4.2}$$

where α is the absorption coefficient.

The total photocurrent is contributed from two different regions: the depletion regions and the neutral regions. In a depletion region, the photocurrent density is mainly contributed by the drift current density, given as

$$\mathbf{J}_{dr}(\mathbf{s}) = q\int G(x, s)d\mathbf{r}. \tag{4.3}$$

where $\mathbf{r}$ is in the direction of electric field. Then the drift current can be obtained by taking surface integrals as

$$I_{dr}(s) = \int \mathbf{J}_{dr}(\mathbf{s})\cdot d\mathbf{s}. \tag{4.4a}$$

In a neutral region, the electric field is negligible and thus the photocurrent density is mainly contributed by the diffusion current density. Therefore, the continuity equations of these photogenerated carriers in the frequency domain can be written as

$$\begin{aligned} sN_p &= G - \frac{N_p}{\tau_n} + D_n \nabla^2 N_p && (4.5a)\\ sP_n &= G - \frac{P_n}{\tau_p} + D_p \nabla^2 P_n && (4.5b) \end{aligned}$$

where N_p is the electron concentration in the p-type material, and P_n is the hole concentration in the n-type material; τ_p and τ_n are the carrier lifetimes for electrons and holes, respectively; D_n and D_p are the diffusion constants for electrons and holes, respectively. Combining the continuity equations in (4.5a) and (4.5b) with the boundary conditions yields the minority carrier concentrations N_p and P_n, and the electron and hole diffusion current density can then be obtained as

$$\begin{aligned} \mathbf{J}_n(s) &= qD_n \nabla N_p && (4.6a)\\ \mathbf{J}_p(s) &= -qD_p \nabla P_n. && (4.6b) \end{aligned}$$

Then the electron and hole diffusion currents can be obtained by taking surface integrals as

$$\begin{aligned} I_n(s) &= \int \mathbf{J}_n(s) \cdot d\mathbf{s}, && (4.7a)\\ I_p(s) &= \int \mathbf{J}_p(s) \cdot d\mathbf{s}. && (4.7b) \end{aligned}$$

4.3.2 Square-Shaped SMPD

For an $\mathrm{N_{well}/P_{sub}}$ square-shaped SMPD shown in Figure 4-1(a), the drift current of a depletion region can be obtained from (4.3) as

$$I_{dr}(s) = \frac{A}{2W_P^2} q\Phi_0(s) \left\{ \left(W_P^2 - w'^2 \right) \left(1 - e^{-\alpha L_1} \right) + W_P^2 \left[e^{-\alpha L_1} - e^{-\alpha (L_1 + D_1)} \right] \right\}. \qquad (4.8)$$

In the N$_{\text{well}}$ neutral regions, the boundary conditions of a unit cell are governed by

$$\begin{aligned} \left.\frac{\partial P_n}{\partial x}\right|_{x=0} &= 0, \quad P_n|_{x=L_1} = 0 && \text{(4.9a)} \\ P_n|_{y=0} &= 0, \quad P_n|_{y=w'} = 0 && \text{(4.9b)} \\ P_n|_{z=0} &= 0, \quad P_n|_{z=w'} = 0. && \text{(4.9c)} \end{aligned}$$

To solve this problem analytically, the Fourier series in the space domain that satisfy the boundary conditions given above are taken. According to (4.5b) and (4.6b), the hole diffusion current can be obtained by taking surface integrals over the side surfaces and the bottom surface as

$$\begin{aligned} I_p(s) = {} & \sum_{m=1}^{\infty}\sum_{n=1}^{\infty}\sum_{k=1}^{\infty} \frac{A}{2W_P^2} qD_p\alpha\Phi_0(s) \times \frac{(2m-1)\pi(-1)^{m+1}e^{-\alpha L_1}+2\alpha L_1}{(\alpha L_1)^2+\left[\frac{(2m-1)\pi}{2}\right]^2} \\ & \times \left[\frac{w'^2}{L_1}\frac{2\,(2m-1)}{(2n-1)(2k-1)\pi} + L_1\frac{8(2n-1)}{(2m-1)\,(2k-1)\pi} + L_1\frac{8(2k-1)}{(2m-1)\,(2n-1)\pi}\right] \\ & \times \frac{(-1)^{m+1}}{s+D_pB_{mnk}+\frac{1}{\tau_p}} \times \frac{4}{(2n-1)\pi} \times \frac{4}{(2k-1)\pi} \qquad \text{(4.10)} \end{aligned}$$

where

$$B_{mnk} = \left[\frac{(2m-1)\,\pi}{2L_1}\right]^2 + \left[\frac{(2n-1)\,\pi}{w'}\right]^2 + \left[\frac{(2k-1)\,\pi}{w'}\right]^2. \qquad \text{(4.11)}$$

In the neutral P$_{\text{sub}}$ regions, the boundary conditions of a unit cell can be approximated by

$$\begin{aligned} N_p|_{x=L_1+D_1} &= 0, \quad N_p|_{x=L_1+D_1+L_2} = 0, && \text{(4.12a)} \\ N_p|_{y'=0} &= N_p|_{y'=\frac{2}{\sqrt{5}}W_P} && \text{(4.12b)} \end{aligned}$$

where $y\prime$ is the rotation axis after rotating the y-axis an angle of $\cos^{-1}\left(2/\sqrt{5}\right)$. According to (4.5a) and (4.6a), the immediate and deferred electron diffusion currents can be obtained by taking surface integrals over the top surface as

$$I_{nI}(s) = \frac{A}{2} q D_n \alpha \Phi_0(s) e^{-\alpha(L_1+D_1)} \frac{m\pi}{L_2} \times \left[\sum_{m=1}^{\infty} C_m(s) + \sum_{m=1}^{\infty} \sum_{n=1}^{\infty} C_{mn}(s) \right] \quad (4.13a)$$

$$I_{nD}(s) = \frac{A}{2} q D_n \alpha \Phi_0(s) e^{-\alpha(L_1+D_1)} \frac{m\pi}{L_2} \times \left[\sum_{m=1}^{\infty} C_m(s) - \sum_{m=1}^{\infty} \sum_{n=1}^{\infty} C_{mn}(s) \right] \quad (4.13b)$$

where

$$C_m(s) = \frac{1}{2\left[s + D_n \left(\frac{m\pi}{L_2} \right)^2 + \frac{1}{\tau_n} \right]} \times \frac{2m\pi \left[1 - (-1)^m e^{-\alpha L_2} \right]}{(\alpha L_2)^2 + (m\pi)^2} \quad (4.14a)$$

$$C_{mn}(s) = \frac{\left[\frac{2}{(2n-1)\pi} \right]^2}{s + D_n \left(\frac{m\pi}{L_2} \right)^2 + D_n \left[\frac{(2n-1)\pi}{\frac{2}{\sqrt{5}} W_P} \right]^2 + \frac{1}{\tau_n}} \times \frac{2m\pi \left[1 - (-1)^m e^{-\alpha L_2} \right]}{(\alpha L_2)^2 + (m\pi)^2} . \quad (4.14b)$$

Since $I_{\text{imm}}(s) = I_{dr}(s) + I_p(s) + I_{nI}(s)$ and $I_{\text{def}}(s) = I_{nD}(s)$, the differential output current can be obtained as

$$\begin{aligned} I_{od}(s) &= I_{\text{imm}}(s) - I_{\text{def}}(s) \\ &= \left[I_{dr}(s) + I_p(s) + I_{nI}(s) \right] - I_{nD}(s). \end{aligned} \quad (4.15)$$

4.3.3 Meshed SMPD

For an $\text{N}_{\text{well}}/\text{P}_{\text{sub}}$ meshed SMPD shown in Figure 4-1(b), the drift current of a depletion region can be obtained from (4.3) as

$$I_{dr}(s) = \frac{A}{2 L_{YP} L_{ZP}} q \Phi_0(s) \left\{ L_{YP} L_{ZP} \left[e^{-\alpha L_1} - e^{-\alpha(L_1+D_1)} \right] + \left(L_{YP} L_{ZP} - L'_Y L'_Z \right) \left(1 - e^{-\alpha L_1} \right) \right\} . \quad (4.16)$$

In the N_{well} neutral regions, the boundary conditions of a unit cell are governed by

$$\left. \frac{\partial p_n}{\partial x} \right|_{x=0} = 0, \quad p_n|_{x=L_1} = 0, \quad (4.17)$$

$$p_n|_{y=0} = 0, \quad p_n|_{y=L'_Y} = 0, \quad (4.18)$$

$$p_n|_{z=0} = 0, \quad p_n|_{z=L'_Z} = 0. \quad (4.19)$$

To solve this problem analytically, the Fourier series in the space domain that satisfy the boundary conditions given above are taken. According to (4.5b) and (4.6b), the hole diffusion current can be obtained by taking surface integrals over the side surfaces and the bottom surface as

$$\begin{aligned} I_p(s) \;=\; & \frac{AqD_p\alpha\Phi_0(s)}{2L_{YP}L_{ZP}} \sum_{m=1}^{\infty}\sum_{n=1}^{\infty}\sum_{k=1}^{\infty} \frac{1}{s + D_p\left[\frac{(2m-1)\pi}{2L_1}\right]^2 + D_p\left[\frac{(2n-1)\pi}{L_Y'}\right]^2 + D_p\left[\frac{(2k-1)\pi}{L_Z'}\right]^2 + \frac{1}{\tau_p}} \\ & \times \left[\frac{L_Y' L_Z'}{L_1}\frac{2\,(2m-1)}{(2n-1)(2k-1)\pi} + \frac{L_1 L_Z'}{L_Y'}\frac{8(2n-1)}{(2m-1)\,(2k-1)\pi} + \frac{L_1 L_Y'}{L_Z'}\frac{8(2k-1)}{(2m-1)\,(2n-1)\pi}\right] \\ & \times \frac{(2m-1)\pi(-1)^{m+1}e^{-\alpha L_1} + 2\alpha L_1}{(\alpha L_1)^2 + \left[\frac{(2m-1)\pi}{2}\right]^2} \times \frac{4}{(2n-1)\pi} \times \frac{4}{(2k-1)\pi} \times (-1)^{m+1}. \qquad (4.20) \end{aligned}$$

In the neutral $\mathrm{P_{sub}}$ regions, the boundary conditions of a unit cell can be approximated by

$$n_p|_{x'=0} \;=\; 0, \quad n_p|_{x'=L_2} = 0, \qquad (4.21)$$

$$n_p\,(y=0) \;=\; n_p\,(y=L_{YP})\,, \qquad (4.22)$$

$$n_p\,(z=0) \;=\; n_p\,(z=L_{ZP})\,. \qquad (4.23)$$

According to (4.5a) and (4.6a), the immediate and deferred electron diffusion currents can be obtained by taking surface integrals over the top surface as

$$I_{nI}(s) \;=\; \frac{A}{4L_{YP}L_{YP}} qD_n\alpha\Phi_0(s)e^{-\alpha(L_1+D_1)}\frac{m\pi}{L_2}\left[\sum_{m=1}^{\infty} C_m(s) + \sum_{m=1}^{\infty}\sum_{n=1}^{\infty} C_{mnk}(s)\right] \qquad (4.24)$$

$$I_{nD}(s) \;=\; \frac{A}{4L_{YP}L_{YP}} qD_n\alpha\Phi_0(s)e^{-\alpha(L_1+D_1)}\frac{m\pi}{L_2}\left[\sum_{m=1}^{\infty} C_m(s) - \sum_{m=1}^{\infty}\sum_{n=1}^{\infty} C_{mnk}(s)\right] \qquad (4.25)$$

where

$$\begin{aligned}
C_m(s) &= \frac{L_{YP}L_{ZP}}{2\left[s + D_n\left(\frac{m\pi}{L_2}\right)^2 + \frac{1}{\tau_n}\right]} \times \frac{2m\pi\left[1-(-1)^m e^{-\alpha L_2}\right]}{(\alpha L_2)^2 + (m\pi)^2}, && (4.26)\\
C_{mnk}(s) &= \frac{8L_{YP}L_{ZP}}{s + D_n\left(\frac{m\pi}{L_2}\right)^2 + D_n\left[\frac{(2n-1)\pi}{L_{YP}}\right]^2 + D_n\left[\frac{(2k-1)\pi}{L_{ZP}}\right]^2 + \frac{1}{\tau_n}}\\
&\quad \times \frac{2m\pi\left[1-(-1)^m e^{-\alpha L_2}\right]}{(\alpha L_2)^2 + (m\pi)^2} \times \frac{2}{\left[(2n-1)\pi\right]^2} \times \frac{2}{\left[(2k-1)\pi\right]^2}. && (4.27)
\end{aligned}$$

Since $I_{\text{imm}}(s) = I_{dr}(s) + I_p(s) + I_{nI}(s)$ and $I_{\text{def}}(s) = I_{nD}(s)$, the differential output current can be obtained as

$$\begin{aligned}
I_{od}(s) &= I_{\text{imm}}(s) - I_{\text{def}}(s)\\
&= \left[I_{dr}(s) + I_p(s) + I_{nI}(s)\right] - I_{nD}(s). && (4.28)
\end{aligned}$$

4.4 Simulations of the Photocurrent Response

4.4.1 Simulation Parameters

For optical interconnects, an optical receiver mainly consists of a photodetector, a transimpedance amplifier (TIA), and a buffer. The proposed SMPD requires a differential-input TIA to subtract the deferred current (I_{def}) from the immediate current (I_{imm}), and the SMPD should be operated in a reverse-biased region. Figure 4-2 illustrates the proposed connecting configurations of the SMPD with the subsequent circuits, where D_U and D_S denote the unshaded diodes and shaded diodes, respectively. (i) For N$_{\text{well}}$/P$_{\text{sub}}$ SMPDs, the N$_{\text{well}}$ nodes are connected to the TIA input nodes, as shown in Figure 4-2(a). The P$_{\text{sub}}$ nodes (V_{P}) are generally connected to ground, and can be alternatively connected to another potential if required. The higher the reverse bias is applied to the SMPD, the larger the depletion regions will be formed, and thereby the larger the photocurrent can be produced. (ii) For N$^+$/P$_{\text{well}}$ SMPDs, the connecting configuration is in a similar way; the N$^+$ nodes are connected to the TIA input nodes, while the P$_{\text{well}}$ nodes are connected to ground. (iii) On the other hand, Figure 4-2(b) shows the connecting configuration for P$^+$/N$_{\text{well}}$ SMPDs. The P$^+$ nodes are connected to the TIA input nodes, while the N$_{\text{well}}$

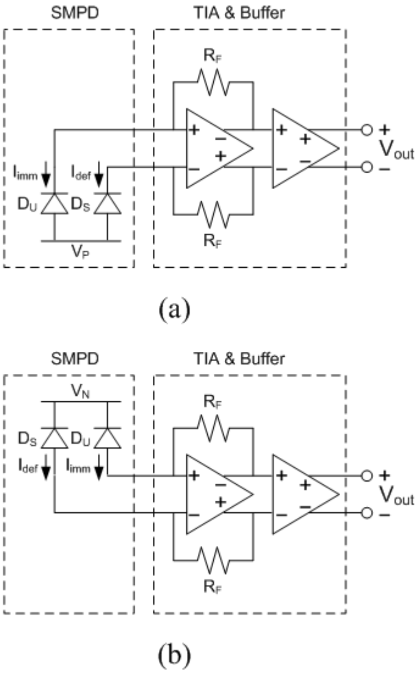

Figure 4-2: Connecting configurations of TIA and SMPD adopting (a) $\mathrm{N_{well}/P_{sub}}$ junctions or $\mathrm{N^+/P_{well}}$ junctions, and (b) $\mathrm{P^+/N_{well}}$ junctions.

nodes (V_{N}) are connected to the highest potential of the whole system.

To compare the characteristics of the proposed SMPDs with other CMOS photodetectors, the traditional finger photodiode and the finger-shaped SMPD as shown in Figure 4-3 are examined. Following the approach described in Section III, the analytic expression of the photocurrent for these photodetectors can also be obtained.

In the following simulations, each kind of CMOS photodetector is illuminated by 850-nm light with 1-mW power. The absorption coefficient of silicon at 850 nm is approximately 0.06 $\mu\mathrm{m}^{-1}$ [1], [50]. The area of the photodetector is set as 50 μm × 50 μm to roughly fit the cross section of a multimode optical fiber [16]. The material parameters such as doping concentrations and junction depths based on a standard CMOS technology are shown in Table **??**. The minority carrier mobility and lifetime of electrons and holes in silicon related to the doping concentration at room temperature (300 K) can be evaluated by [51]

$$\mu_n(N_A) = 232 + \frac{1180}{1+\left(\frac{N_A}{8\times10^{16}}\right)^{0.9}} \tag{4.29a}$$

$$\mu_p(N_D) = 130 + \frac{370}{1+\left(\frac{N_D}{8\times10^{17}}\right)^{1.25}} \tag{4.29b}$$

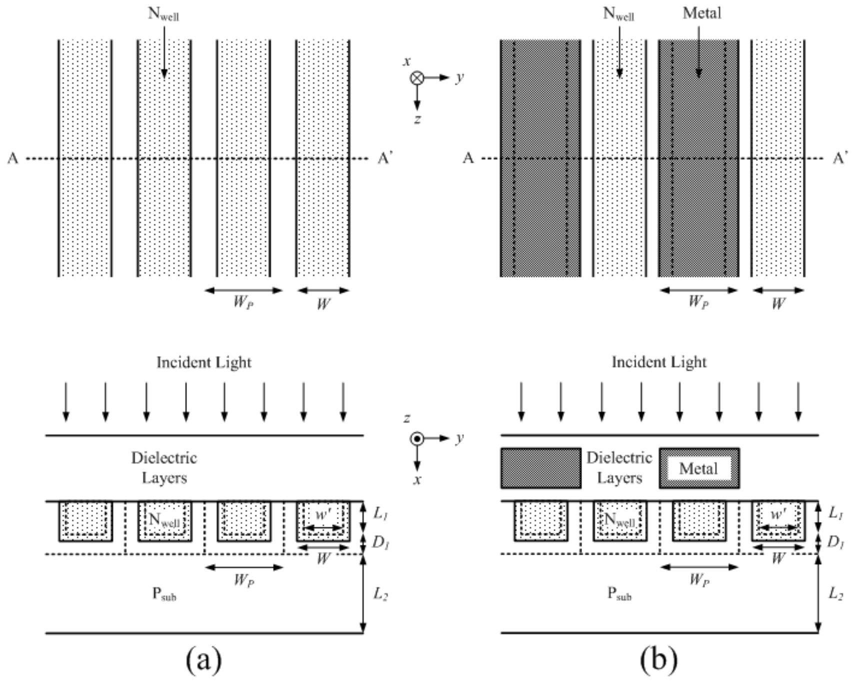

Figure 4-3: Top views and cross sections of (a) finger photodiode and (b) finger-shaped SMPD.

Table 4.1: Doping concentrations and junction depths.

	Doping Conc. (cm^{-3})	Junction Depth (μm)
N$^+$, P$^+$	10^{20}	0.2
N$_{\text{well}}$, P$_{\text{well}}$	10^{18}	1.0
P$_{\text{sub}}$	10^{16}	150

$$\tau_n(N_A) = \frac{1}{3.45\times 10^{-12} N_A + 9.5\times 10^{-32} N_A^2} \tag{4.29c}$$

$$\tau_p(N_D) = \frac{1}{7.8\times 10^{-13} N_D + 1.8\times 10^{-31} N_D^2} \tag{4.29d}$$

where N_A and N_D are the p-type and n-type doping concentration in units of cm^{-3}, respectively. Since the carriers require a finite time to traverse the depletion layer, the bandwidth of the drift current is limited to $f_{\text{drift}} = 2.4/(2\pi t_r)$, where t_r is the carrier transit time to drift through the depletion region [31]. For N$_{\text{well}}$/P$_{\text{sub}}$ junctions, f_{drift} is about 15 GHz; for N$^+$/P$_{\text{well}}$ and P$^+$/N$_{\text{well}}$ junctions, f_{drift} is about 130 GHz.

In the vertical structure of a standard CMOS technology, the dielectric layers above the active region comprise an inter-layer dielectric layer, inter-metal dielectric layers, and optional passivation layers. The reflectance of the multi-layer structure can be calculated using the impedance-transformation approach [21], and the results show that the reflectance can be improved by removing the passivation layer above the active regions of the photodetector.

4.4.2 $\mathbf{N_{well}/P_{sub}}$ Junctions with $V_R = 1$ V

Regarding N_{well}/P_{sub} SMPDs, the allowable minimum widths of W and W_p are 2.1 μm and 3.5 μm, respectively. In order to make sure that the depletion regions of adjacent cells are in direct contact with each other, the reverse bias voltage of the photodiodes is set as 1 V. The simulation results of the photocurrent responses for N_{well}/P_{sub} photodetectors are illustrated in Figs. 4-4 to 4-7, and the characteristics are summarized in Table **??**. In the figures, I_o denotes the total output current of the finger photodiode, and other currents are defined in Section 4.3. It is worth noting that the square-shaped SMPD achieves the largest bandwidth and gain-bandwidth product (GBW) among these CMOS photodetectors.

For a traditional single photodiode, the main contribution to the total photocurrent is the substrate current. The photogenerated carriers deep in the substrate take a longer time to diffuse upwardly to the depletion region, and this process strongly limits the device bandwidth.

For a finger photodiode, the increase in the drift current of the depletion region cannot efficiently improve the bandwidth (only 1.2 MHz), since the photocurrent is still dominated by the substrate current.

For a finger-shaped SMPD, the 3-dB bandwidth is promoted to 1.4 GHz since the slow response effect resulting from the P_{sub} diffusion current is eliminated by subtracting the deferred portion from the immediate portion of the photocurrent.

For the proposed square-shaped SMPD and meshed SMPD, the 3-dB bandwidth is further broadened to 3.9 GHz and 8.5 GHz, respectively. There are three main reasons why adopting these particular layout style (square-shaped N_{well} regions) enhances the bandwidth. (i) The slow response effect resulting from the P_{sub} diffusion current is eliminated as the subtraction becomes more effective on account of the narrower spacing between the shaded and unshaded regions. (ii) Another slow response effect resulting from the N_{well} diffusion current is decreased due to the reduced amount of the photogenerated carriers

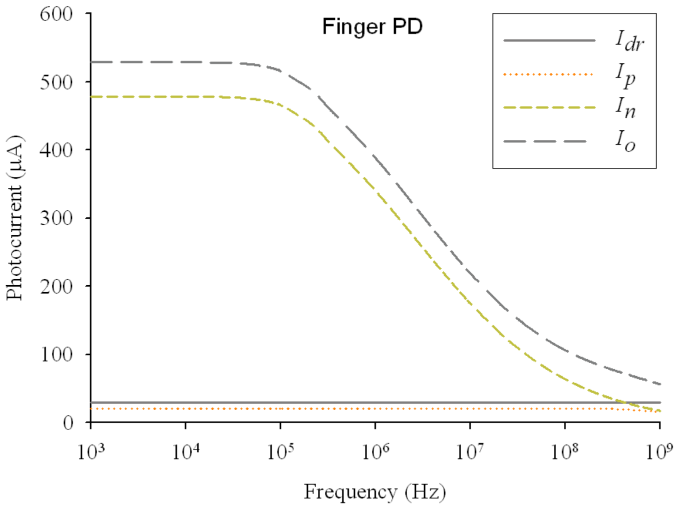

Figure 4-4: Photocurrent response of the $N_{\text{well}}/P_{\text{sub}}$ finger photodiode with $V_R = 1$ V.

Table 4.2: Characteristics of the photodetectors for $N_{\text{well}}/P_{\text{sub}}$, N^+/P_{well}, and P^+/N_{well} junctions.

Photodetector Type		$I_{3\text{dB}}$ (μA)	$f_{3\text{dB}}$ (GHz)	GBW (kA·Hz)
$N_{\text{well}}/P_{\text{sub}}$	Finger SMPD	23.12	1.4	32.4
	Square SMPD	22.29	3.9	86.9
	Meshed SMPD	19.13	8.5	162.6
N^+/P_{well}	Finger SMPD	6.82	8.9	60.7
	Square SMPD	6.70	12.2	81.7
	Meshed SMPD	4.86	22.8	110.8
P^+/N_{well}	Finger SMPD	6.83	7.7	52.6
	Square SMPD	6.70	9.7	65.0
	Meshed SMPD	4.87	22.7	110.5

in the neutral N_{well} regions. (iii) This particular layout style also extends the $N_{\text{well}}/P_{\text{sub}}$ junction area as well as the depletion regions, and hence increases the drift current. The major features of the square-shaped SMPD and meshed SMPD are the decreased diffusion current and the increased drift current. Since the total photocurrent comes mostly from the drift current, it successfully obtains the larger bandwidth and GBW among the CMOS photodetectors.

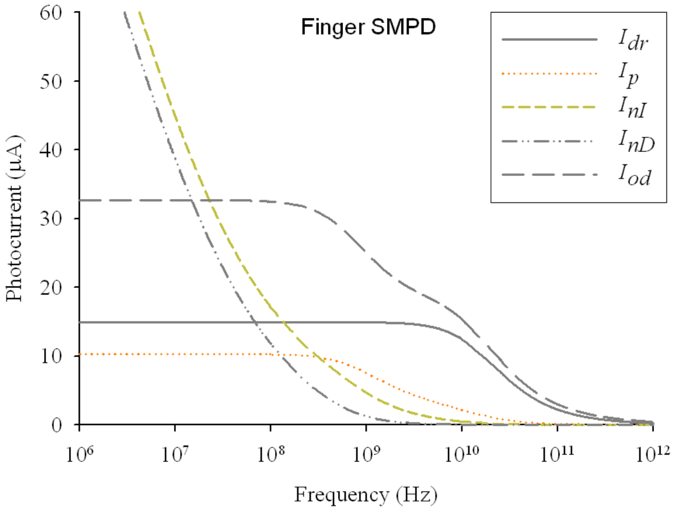

Figure 4-5: Photocurrent response of the $\mathrm{N_{well}/P_{sub}}$ finger-shaped SMPD with $V_R = 1$ V.

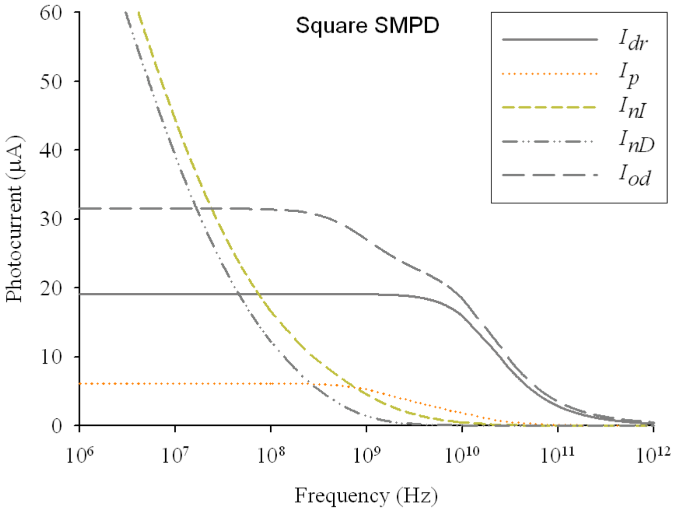

Figure 4-6: Photocurrent response of the $\mathrm{N_{well}/P_{sub}}$ square-shaped SMPD with $V_R = 1$ V.

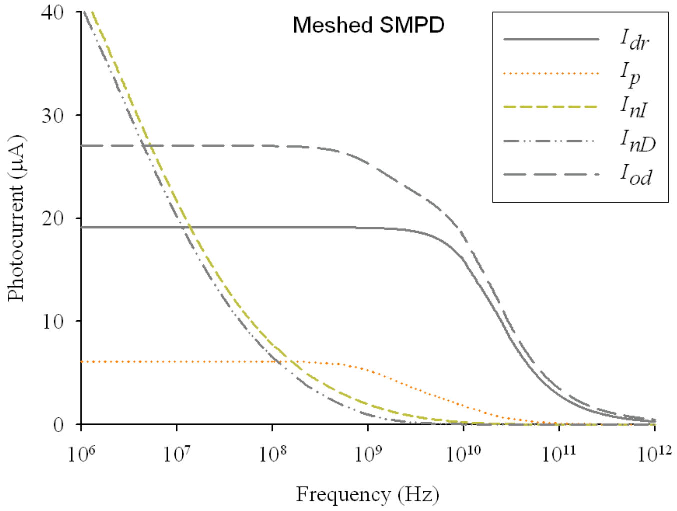

Figure 4-7: Photocurrent response of the $\mathrm{N_{well}/P_{sub}}$ meshed SMPD with $V_R = 1$ V.

4.4.3 $\mathbf{N^+/P_{well}}$ or $\mathbf{P^+/N_{well}}$ Junctions with $V_R = 5$ V

Regarding $\mathrm{N^+/P_{well}}$ and $\mathrm{P^+/N_{well}}$ SMPDs, the practical minimum widths of W and W_p are 1 μm and 1.5 μm, respectively. In order to make sure that the depletion regions of adjacent cells are in direct contact with each other, the reverse bias voltage of the photodiodes is set as 5 V. The simulation characteristics are summarized in Table **??**. For $\mathrm{N^+/P_{well}}$ SMPDs, the $\mathrm{N^+}$ diffusion current does not significantly degrade the bandwidth of the photodetector since the $\mathrm{N^+/P_{well}}$ junction depth (about 0.2 μm) is very shallow. Besides, the slow response effect resulting from the $\mathrm{P_{well}}$ diffusion current is moderated by taking subtraction. The $\mathrm{P_{sub}}$ current can also be removed from the photocurrent by adding a deep $\mathrm{N_{well}}$ layer and connecting it to a positive supply voltage. As a result, high bandwidth and low sensitivity are the common features of the $\mathrm{N^+/P_{well}}$ SMPDs. The $\mathrm{P^+/N_{well}}$ SMPDs are analogous to the $\mathrm{N^+/P_{well}}$ SMPDs, and thereby achieve the comparable performance.

Among various types of CMOS photodetectors, the proposed square-shaped SMPD and meshed SMPD achieve the larger bandwidth and GBW. The 3-dB bandwidths are about 10 GHz and 20 GHz, respectively. It could also be found that the $\mathrm{N^+/P_{well}}$ SMPDs generally achieve a better frequency response than the $\mathrm{P^+/N_{well}}$ SMPDs. This phenomenon results from the difference in mobility between electrons and holes.

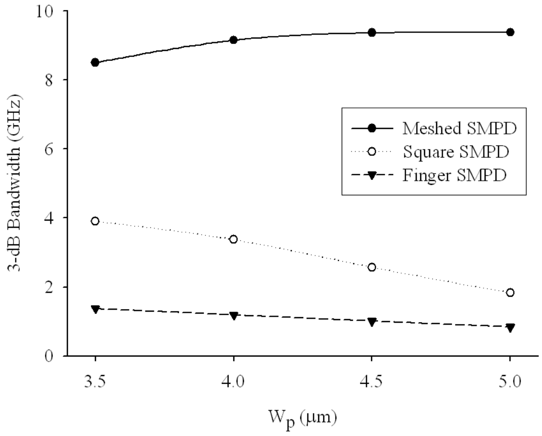

Figure 4-8: The relationship between the 3-dB bandwidth and W_P of $\mathrm{N_{well}/P_{sub}}$ SMPDs with $W = 2.1$ μm.

4.4.4 Influence of Geometric Size

For a SMPD, the geometry has significant influence on the bandwidth. In the first place, W (the width of the particular shape in the $\mathrm{N_{well}}$ region) should be as small as possible to decrease the diffusion current contributed by the neutral $\mathrm{N_{well}}$ region. While W is limited by the design rule of each generation technology, using the square-shaped SMPD could achieve a narrower effective width than that of the finger-shaped SMPD. As for W_P (the width of the unit cell), it should be an appropriate size to ensure that the depletion regions of adjacent cells are in direct contact with each other. In a fixed total area of the SMPD, larger depletion regions will lead to a decreasing diffusion current and an increasing drift current, which will widen the bandwidth.

For $\mathrm{N_{well}/P_{sub}}$ SMPDs with $V_R = 1$ V and $W = 2.1$ μm, the practical maximum width of W_P is 5.1 μm. The simulation results of the 3-dB bandwidths as functions of W_P are illustrated in Figure 4-8. It reveals that the meshed SMPD with $W_p = 5.0$ μm can reach a 3-dB bandwidth of 9.4 GHz. In addition, the results imply that a more advanced CMOS technology will improve the bandwidths of SMPDs, since the diffusion current decreases with the availability of the smaller geometric size of the $\mathrm{N_{well}}$ region.

4.4.5 Parasitic Capacitance

In addition to the intrinsic bandwidth discussed above, the extrinsic bandwidth also governs the in-circuit bandwidth of the SMPD. The extrinsic bandwidth is related to the parasitic capacitances which come from the bottom surface and the side surfaces of the junctions of the SMPD. Although the intrinsic bandwidth of the SMPD is large, the bandwidth of the whole optical receiver would be degraded owing to the parasitic capacitance. Adopting N^+/P_{well} (or P^+/N_{well}) junctions, the calculated parasitic capacitances for finger-shaped, square-shaped, and meshed SMPD are about 1.19 pF, 1.44 pF, and 1.44 pF, respectively. Adopting $N_{\mathrm{well}}/P_{\mathrm{sub}}$ junctions, the parasitic capacitances for finger-shaped, square-shaped, and meshed SMPD could be reduced to 0.37 pF, 0.57 pF, and 0.57 pF, respectively.

In general, the input impedance of the subsequent TIA should be kept low enough to drop off the RC delay effect. By employing a regulated cascode and shunt-shunt feedback configuration, the influence of the parasitic capacitances can be alleviated [52]. Another technique to enhance the TIA bandwidth is inductive peaking, but the stray capacitance caused by the bulky spiral inductor will limit its optimization. By adopting an active inductor, the parasitic capacitance can be greatly reduced to avoid bandwidth deterioration.

4.5 Measurement Results

The high-speed circuits and measurements were assisted by Prof. Wei-Zen Chen's group. The proposed square-shaped SMPD and meshed SMPD adopting $N_{\mathrm{well}}/P_{\mathrm{sub}}$ junctions were manufactured using the TSMC (Taiwan Semiconductor Manufacturing Company) 0.18-μm standard CMOS technology. The experimental setup is shown in Figure 4-9. The OEIC (opto-electronic integrated circuits) chip was mounted on a printed circuit board for measurement. The eye diagrams and the bit error rate performance were characterized using a signal quality analyzer (Anritsu MP1800). The pattern generator in the Anritsu MP1800 sent a $(2^{31}-1)$ PRBS (pseudo-random binary sequence) test pattern to modulate an 850-nm 10-Gbps VCSEL (New Focus) as a light source. The generated light was guided by the multimode fibers (MMF), and the optical power was attenuated by a digital variable attenuator (OZ Optics) for input sensitivity measurement. And the

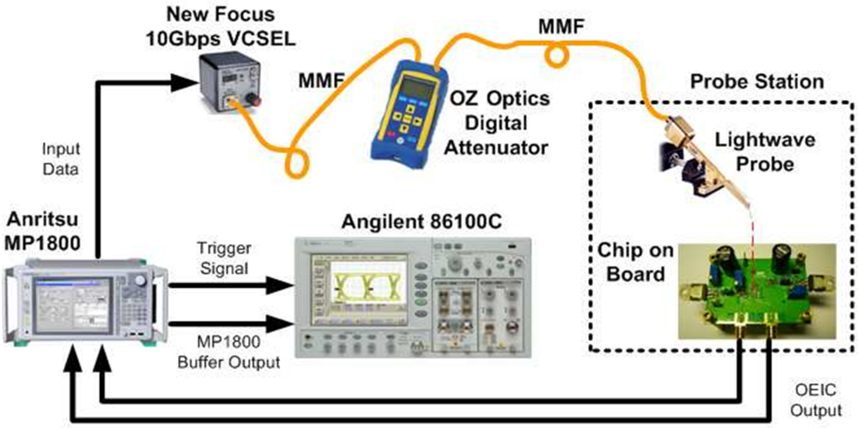

Figure 4-9: The experimental setup for the frequency response measurement.

light was guided by a cascade lightwave probe (fixed in the RF-1 cascade probe station) to the SMPD on the chip. Then the OEIC amplified the photocurrent and sent a pair of differential output signal back to the Anritsu MP1800 for bit-error-rate test. And the Anritsu MP1800 sent the unity-gain buffer output and trigger signal to a wide bandwidth oscilloscope (Agilent 86100C Infiniium DCA-J) for observation and data record.

Figure 4-10 depicts the measured frequency response of the square-shaped SMPD. To investigate the effects of bias voltage on the responsivity and bandwidth of the SMPD, the bias voltages of 1.2 V, 11.2 V, and 14.2 V were applied. The corresponding responsivities were about 29 mA/W, 38 mA/W, and 48 mA/W, respectively; The extrinsic 3-dB bandwidths were about 1.0 GHz, 3.3 GHz, and 3.6 GHz, respectively.

Figure 4-11 depicts the measured frequency response of the meshed SMPD. For the bias voltages of 1.2 V, 11.2 V, and 14.2 V, the corresponding responsivities were about 18 mA/W, 23 mA/W, and 28 mA/W, respectively; The extrinsic 3-dB bandwidths were about 2.0 GHz, 4.0 GHz, and 5.5 GHz, respectively. The achievable bandwidth is wider than other reported photodetectors manufactured using a standard CMOS technology.

4.6 Summary

In this research, we have presented the design, analysis, simulation, and measurement of the square-shaped SMPD and meshed SMPD to achieve a faster photocurrent response. Two other CMOS photodetectors, the finger photodiode and the finger-shaped SMPD, were also examined for comparisons.

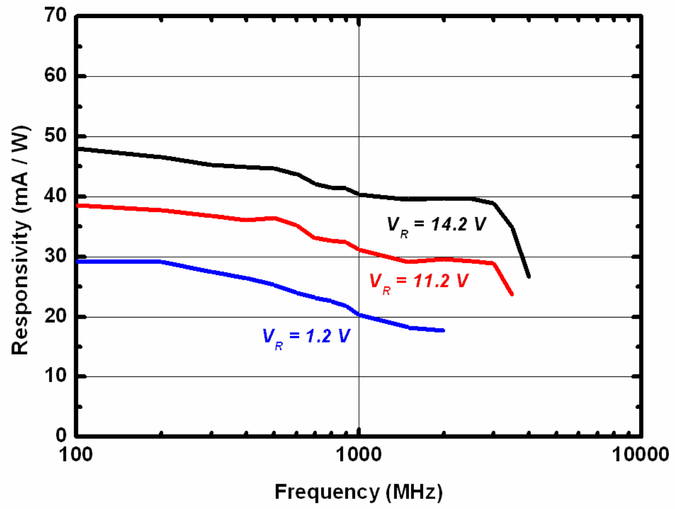

Figure 4-10: The measured frequency response of the N_{well}/P_{sub} square-shaped SMPD.

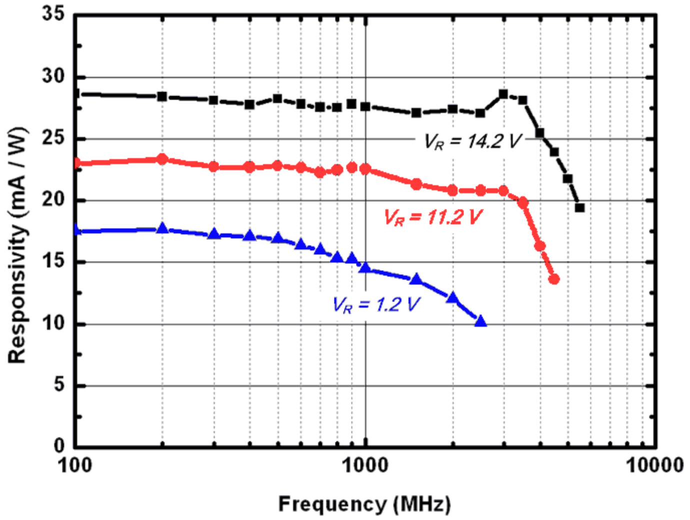

Figure 4-11: The measured frequency response of the N_{well}/P_{sub} meshed SMPD.

For the photodetectors adopting N_{well}/P_{sub} junctions, the traditional single photodiode and the finger photodiode are not capable of high-speed operation, because the bandwidth is limited by the slow response of the substrate current. By subtracting the deferred portion from the immediate portion of the photocurrent, the SMPD promotes the bandwidth to the GHz range. The proposed square-shaped SMPD and meshed SMPD even more efficiently weakens the influences of the diffusion current coming from the neutral N_{well} and P_{sub} regions, and could improve the bandwidth to around 3.9 GHz and 8.5 GHz, respectively. Measurement results of 3.6 GHz and 5.5 GHz are also presented.

On the other hand, for the photodetectors adopting N^+/P_{well} or P^+/N_{well} junctions, the common features are high bandwidth and low sensitivity since the substrate current can be removed from the photocurrent. The proposed square-shaped SMPD and meshed SMPD could also attain a high bandwidth of around 10 GHz and 20 GHz, respectively.

Among the above-mentioned CMOS photodetectors, the N_{well}/P_{sub} meshed SMPD accomplishes the largest GBW, and the bandwidth will be further improved when using a more advanced CMOS technology.

Chapter 5

Deep-N_{well} Based Photodiodes for High-Speed Applications

5.1 Introduction

Typically, the photodetector in CMOS technology is made up of N_{well} to P_{sub} reversed biased junction diode to provide a wider depletion region. However, the penetration depth of the 850-nm light into silicon (about 16.7 μm) is much larger than that of the shallow well (about 2 μm). As a result, a large portion of carriers are generated in the substrate and diffuse in all directions and contribute to the deferred photo current. To boost the speed performance of the photo detector, conventionally, one approach is try to get rid of the slowly diffusive carriers [53]-[57], and an alternative approach is to compensate the frequency response of the photodetector by utilizing equalizer [58]. The former approach can be achieved by using a buried oxide layer [56] or SOI [57] process, but it requires nonstandard CMOS technology and additional cost. On the other hand, the diffusive carrier can be partially eliminated by employing spatially modulated photodetector (SMPD) [53], [54], which consists of a row of photo detectors alternatively covered and uncovered with a light blocking materials. The SMPD is capable of high-speed operation, but at the expense of a relatively smaller responsivity [54].

This research focuses on the design of a CMOS optical receiver, which monolithically integrates a deep-N_{well} (DNW) based photodiode (PD), a trans-impedance amplifier (TIA), and a post limiting amplifier (PA) in a standard CMOS technology. High-speed operation is achieved by utilizing a proposed lateral PIN photodiode. It achieves a higher sensitivity as well as operating speed compared to the prior art [53] without an equalizer. In contrast to conventional multi-die solutions, which composed of the photodetector implemented in more expensive GaAs or InP-InGaAs technology, the fully integrated optical receiver is expected to be much more cost effective. Also, compared to a multi-chip integrated optical receiver, the proposed architecture is free of pin inductance and interstage matching networks for the cascading amplifiers. Thus the gain loss and extra power dissipated in the broad-band matching networks can be greatly saved.

5.2 Principles and Methods

5.2.1 Deep-$\mathrm{N_{well}}$ Based PIN Photodiode

To circumvent the above-mentioned issues of conventional $\mathrm{N_{well}/P_{sub}}$ SMPD without resort to sophisticated equalizer, this research proposes a novel lateral PIN photodiode, emulated by a $\mathrm{P^+/P_{well}/N^+}$ interleaved architecture. Figure 5-1 illustrates the top view and cross section of the detector. This detector is fabricated in the active region, surrounded by $\mathrm{N_{well}}$ and deep $\mathrm{N_{well}}$ (DNW). To comply with the diameter of the multi-mode fiber, the dimension of the photo detector is only 50 μm × 50 μm, consisting of 13 P-I-N fingers. In this experimental prototype, the $\mathrm{P^+}$ and $\mathrm{N^+}$ stripes are 1.45-μm wide (w), separated by a 0.5-μm wide $\mathrm{P_{well}}$ region (w_s). The top of the sensing region is stripped off salicide to disconnect $\mathrm{P^+/P_{well}/N^+}$ regions and is stripped off passivation layers to alleviate the light reflection. Compared to conventional $\mathrm{N_{well}/P_{sub}}$ junction, the electron-hole pairs are mainly generated in the laterally depleted regions. On the other hand, the well is tied to the highest voltage, which protects the PIN photodiode from substrate noise coupling.

The photocurrent I_{ph} of the proposed PIN photodiode can be expressed as

$$I_{ph} = I_p + I_n + I_{dr} \tag{5.30}$$

where I_p and I_n respectively denote the hole and electron diffusion current in the neutral regions, and I_{dr} is the drift current in the depletion regions [31]. In the followings, each component of the photocurrent is explored to investigate the overall frequency response.

Consider the hole current generated in the $\mathrm{N^+}$ diffusion neutral region $I_{p(N^+)}$. As

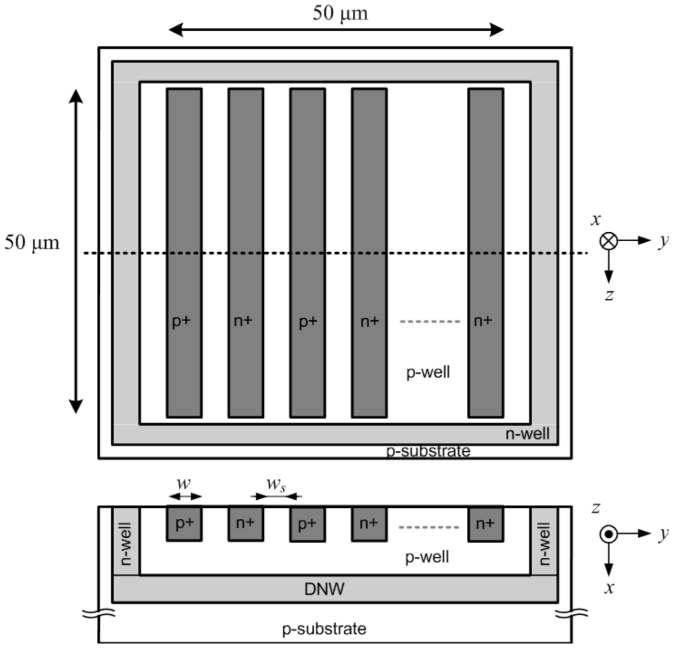

Figure 5-1: Top view and cross section of the PIN photodiode.

illustrated in Figure 5-2, the hole density P_n in the diffusion region is governed by the following boundary conditions:

$$\left.\frac{\partial P_n}{\partial x}\right|_{x=0} = 0, \tag{5.31a}$$

$$P_n|_{x=l'} = 0, \tag{5.31b}$$

$$P_n|_{y=0} = 0, \tag{5.31c}$$

$$P_n|_{y=w'} = 0. \tag{5.31d}$$

Here, x-axis and y-axis represent the directions in perpendicular and parallel to the surface, respectively; L_1 and w' denote the depth and width of the neutral region, respectively; D_1 is the depth of the depletion region. The first boundary condition (5.31a) means that the surface recombination process is much slower than the input signal, and consequently the gradient of excess carrier density in the x-direction is assumed to be zero. The other three boundary conditions (5.31b)-(5.31d) show that the excess carrier density would approach zero at the edge of the depletion region as long as the P/N junction is reverse biased. Based on (5.31a)-(5.31d), the hole diffusion current $I_{p(N+)}$ can then be derived by solving continuity equation using Fourier series expansion [31], [58].

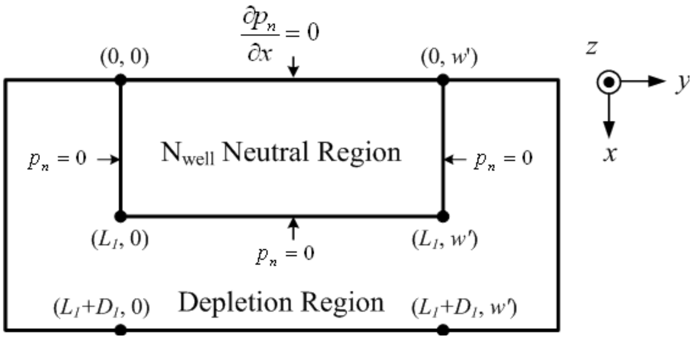

Figure 5-2: Hole density in the N+ diffusion neutral region.

We have

$$
\begin{aligned}
I_{p(N^+)}(s) &= -\frac{A}{(w+w_s)}qD_p\left[\int_0^{w'}\left.\frac{\partial P_n}{\partial x}\right|_{x=l'}dy+\int_0^{L_1}-\left.\frac{\partial P_n}{\partial y}\right|_{y=0}dx+\int_0^{L_1}\left.\frac{\partial P_n}{\partial y}\right|_{y=w'}dx\right]\\
&= \sum_{m=1}^{\infty}\sum_{n=1}^{\infty}\frac{A}{(w+w_s)}qD_p\alpha\Phi_0(s)a_{mn}(-1)^{m+1}\left[\frac{w'}{L_1}\frac{2m-1}{2n-1}+\frac{L_1}{w'}\frac{4\,(2n-1)}{2m-1}\right]\\
&= \sum_{m=1}^{\infty}\sum_{n=1}^{\infty}\frac{AqD_p\alpha\Phi_0(s)}{(w+w_s)}\frac{1}{s+D_p\left[\frac{(2m-1)\pi}{2l'}\right]^2+D_p\left[\frac{(2n-1)\pi}{w'}\right]^2+\frac{1}{\tau_p}}\times\frac{4(-1)^{m+1}}{(2n-1)\pi}\\
&\quad\times\frac{(2m-1)\pi(-1)^{m+1}e^{-\alpha L_1}+2\alpha L_1}{(\alpha L_1)^2+\left[\frac{(2m-1)\pi}{2}\right]^2}\times\left[\frac{w'}{L_1}\frac{2m-1}{2n-1}+\frac{L_1}{w'}\frac{4\,(2n-1)}{2m-1}\right]
\end{aligned}
\tag{5.32}
$$

where A is the area of the photo detector, w is the width of the $\mathrm{P^+}$ and $\mathrm{N^+}$ strips, w_s is the space between these strips, q is the charge density of a single electron, α is the absorption coefficient, Φ_0 is the incident photon flux density, D_p and τ_p are the diffusion constant and lifetime for hole, respectively. According to (5.32), the 3-dB bandwidth of the hole diffusion current can be approximated by choosing m and n equal to 1. Thus

$$
f_{P(\text{3-dB})}=\frac{1}{2\pi}\left[D_p\left(\frac{\pi}{2l'}\right)^2+D_p\left(\frac{\pi}{w'}\right)^2+\frac{1}{\tau_p}\right]. \tag{5.33}
$$

Since D_p, l', and τ_p are technology dependent parameters, the bandwidth of the hole current can be improved by adopting a narrower stripe diffusion region (w) to make w' smaller. The electron diffusion current I_n in the $\mathrm{P_{well}}$ neutral region can be derived using the similar approach. It turns out that a narrower stripe $\mathrm{P^+}$ region and a narrower pitch between the $\mathrm{P^+/N^+}$ diffusion regions will also lead to a faster electron diffusion current.

On the other hand, the drift current I_{dr} can be expressed as [31]

$$\begin{aligned} I_{dr}(s) &= \frac{A}{(w+w_s)}\left\{(w+w_s)\int_{L_1}^{L_1+D_1} qG(x,s)dx + (w+w_s-w')\int_{0}^{L_1} qG(x,s)dx\right\} \\ &= Aq\Phi_0(s)\left\{\left[e^{-\alpha L_1} - e^{-\alpha(L_1+D_1)}\right] + \frac{(w+w_s-w')}{(w+w_s)}\left(1-e^{-\alpha l'}\right)\right\}. \qquad (5.34) \end{aligned}$$

As the drift current velocity is much faster than the diffusion current, the responsivity of the photodetector can be improved by increasing the depletion region without significantly degrading the bandwidth of the photodetector. It is noteworthy that the $\mathrm{P_{well}}$/DNW junction also contributes to the drift current I_{dr}. Nevertheless, the slowly diffusive carriers generated in $\mathrm{P_{sub}}$ are decoupled from the photocurrent of the PIN detector by connecting the DNW to a positive supply voltage. As a result, high speed optical detection can be achieved by the proposed $\mathrm{N_{well}}$ shielding lateral PIN architecture.

In a standard CMOS technology, the dielectric layers above the active region comprise an inter-layer dielectric layer, inter-metal dielectric layers, and optional passivation layers. For a multi-layer structure, the reflectance can be calculated by using the impedance-transformation approach. The effective wave impedance Z_i at the front of the ith layer is expressed as [27]

$$Z_i = \eta_i \frac{Z_{i+1} + j\eta_i \tan(k_i d_i)}{\eta_i + jZ_{i+1}\tan(k_i d_i)} \qquad (5.35)$$

where η_i, k_i, and d_i denote the intrinsic impedance, the wavenumber, and the thickness of the ith layer, respectively; Z_{i+1} denotes the effective impedance at the front of the $(i+1)$th layer. This recursive calculation starts from the known impedance of the last layer (silicon substrate), $Z_{\mathrm{last}} = \eta_{\mathrm{Si}}$, backward to the effective impedance at the front of the surface layer, Z_1. Then the reflectance R of the photodiode can be obtained as

$$R = \left|\left(\frac{Z_1-\eta_0}{Z_1+\eta_0}\right)^2\right| \qquad (5.36)$$

where η_0 is the intrinsic impedance of air. With 850-nm incident light, simulation results show that the reflectance of a CMOS detector is around 0.13, and can be reduced to 0.05 by removing the passivation layers.

Figure 5-3 illustrates the simulation results of the photodetector responsivity based on the design parameters of a standard 0.18-μm CMOS technology [59]. For a PIN detector without DNW shielding, the 3-dB bandwidth of the photodetector is only around 1 MHz.

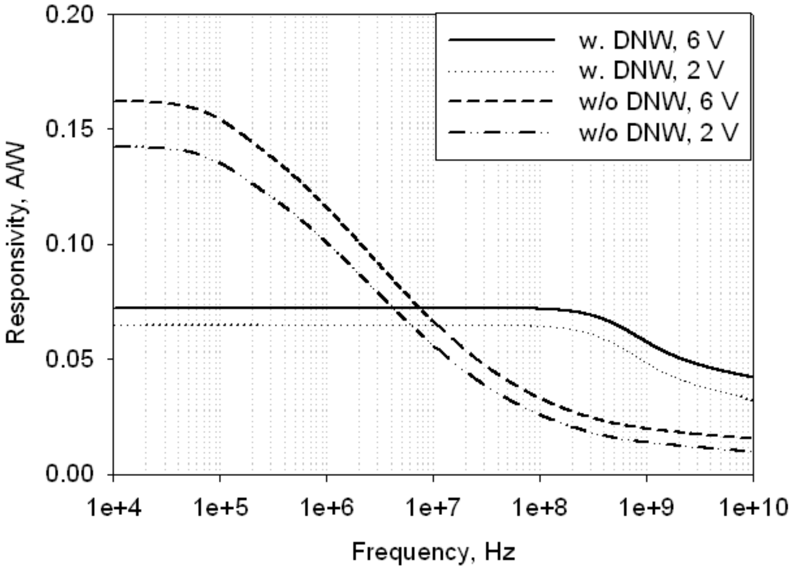

Figure 5-3: Simulated frequency response of PIN PD responsivity

On the contrary, with DNW shielding, it is boosted to 1.2 GHz and 1.9 GHz under a reverse biased voltage V_R of 2 V and 6 V, respectively. Figs. 5-4(a) and 5-4(b) show the frequency response of each component of the photocurrent under a reverse biased voltage V_R of 2 V and 6 V. In both cases, the overall frequency response of I_{ph} is dominated by the hole diffusion current I_p.

The proposed architecture is expected to provide a higher responsivity by enlarging the $\mathrm{P_{well}}$ region and operated in the avalanche mode. In this case, a higher reverse biased voltage can be applied.

5.2.2 Subsequent Circuits

The architecture of the fully integrated optical receiver is shown in Figure 5-5. The incoming optical signal is converted to a photocurrent by on chip PIN photodiode, and regenerated to a voltage signal of 420 $\mathrm{mV_{pp}}$ by a transimpedance amplifier (TIA) and a post limiting amplifier (LA). To alleviate the bandwidth degradation caused by the parasitic capacitances of the photodetector, a trans-impedance amplifier with pseudo-differential regulated cascode (RGC) topology is adopted as the input stage [60]. The gain cell in the limiting amplifier employs the active shunt-shunt feedback to have a wider gain-bandwidth product without inductive peaking. Besides, due to a relatively

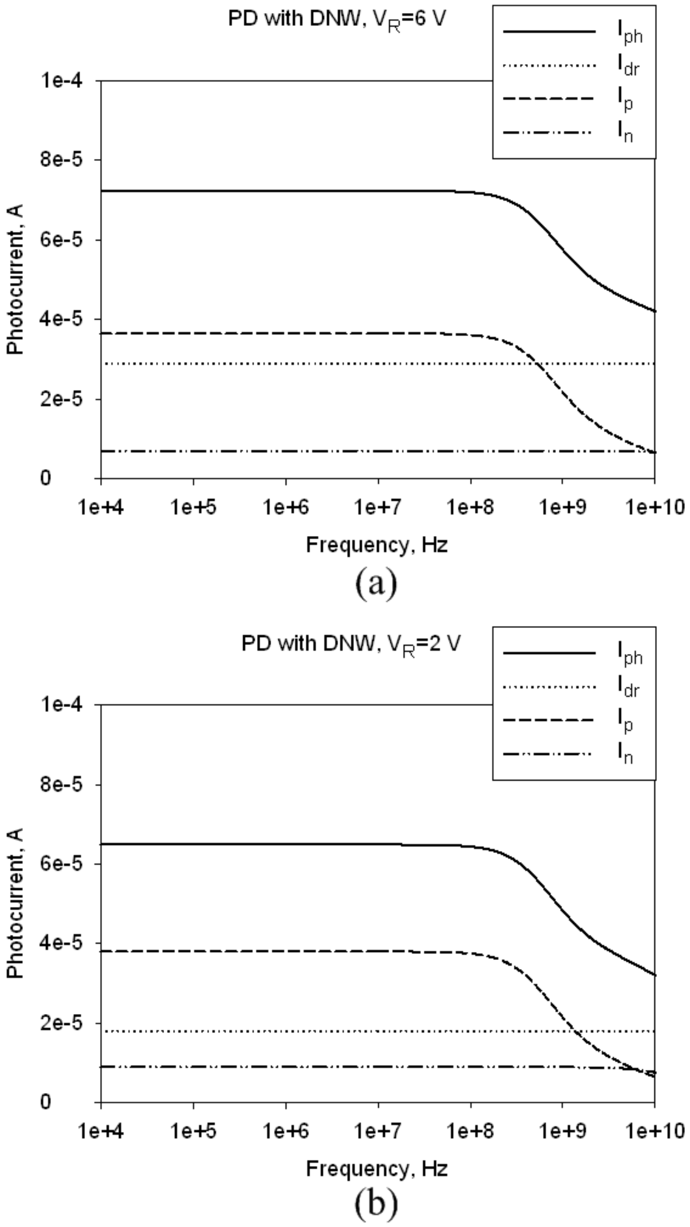

Figure 5-4: (a) $V_R = 6$ V (b) $V_R = 2$ V.

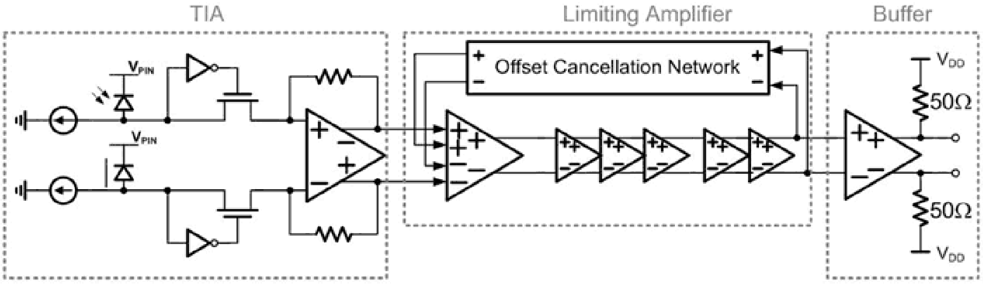

Figure 5-5: Monolithically integrated optical receiver architecture

low responsivity of the PIN detector, no automatic gain control circuit is needed in this design.

For an optical receiver, the input sensitivity is limited by the input referred noise current $\overline{I^2_{n(\mathrm{in})}}$, which can be expressed as

$$\overline{I^2_{n(\mathrm{in})}} = \overline{I^2_{n(\mathrm{TIA})}}\mathrm{BW}_{\mathrm{TIA}} + \frac{\overline{V^2_{n(\mathrm{PA})}}\mathrm{BW}_{\mathrm{PA}}}{T_z^2} \tag{5.37}$$

where T_z is the conversion gain of the TIA, $\overline{I^2_{n(\mathrm{TIA})}}$ represents the input referred noise current of the TIA, $\overline{V^2_{n(\mathrm{PA})}}$ represents the input referred noise voltage of the post voltage amplifier (PA), $\mathrm{BW}_{\mathrm{TIA}}$ and $\mathrm{BW}_{\mathrm{PA}}$ denote the noise bandwidth of TIA and PA, respectively. In this design, the conversion gain of the TIA is about 60 dBΩ to keep the succeeding limiting amplifier from degrading the input sensitivity level.

5.3 Experimental Results

The high-speed circuits and measurements were assisted by Prof. Wei-Zen Chen's group. The chip micrograph is shown in Figure 5-6. Implemented in a standard 0.18-μm CMOS technology, the total chip area is about 620 μm × 860 μm. The receiver IC was mounted on a printed circuit board for measurement. The eye diagrams and the bit error rate performance were characterized using Agilent N4901B. The pattern generator sent a 2^{31-1} PRBS (pseudo-random binary sequence) test pattern to modulate an 850-nm VECSEL (TTR-1F45-457) as a light source. The TIA and the post limiting amplifier were operated under 3.3 V and 1.8 V supply, respectively. The total power dissipation was 138 mW, among which 30 mW was consumed by the output buffer. By cascading the

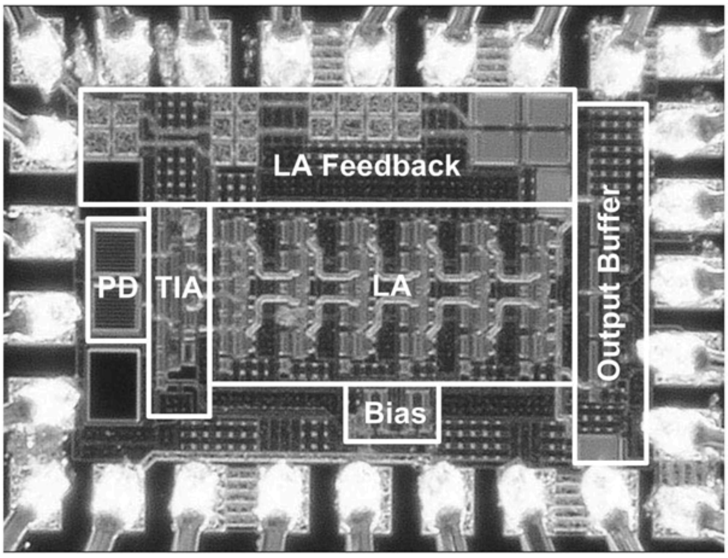

Figure 5-6: Chip micrograph

trans-impedance amplifier and the limiting amplifier on a single chip, the optical receiver provided a conversion gain of 110 dBΩ. The overall 3-dB bandwidth was limited by the photo detector. It was capable of delivering 800-mV_{pp} differential voltage swings to 50-Ω output loads directly.

When the PIN diode was reverse biased under the low-voltage mode (2 V) and high-voltage mode (6 V), the bit-error-rate (BER) performance is summarized in Figs. 5-7(a) and 5-7(b), respectively. Under the high-voltage operating mode, the input sensitivity level of the optical receiver was improved by less than 2 dBm for lower speed operation (1.25 Gbps), which implies that no avalanche mechanism was found in the PIN detector. Also, for BER less than 10^{-12}, the input sensitivity level at 1.25 Gbps and 2.5 Gbps were about -10 dBm and -7 dBm, respectively. It manifests a higher operating speed and a lower BER performance compared to the prior art [53]. Figure 5-8 shows the measured eye diagrams with the input power at the sensitivity level. At 1.25 Gbps under 6 V, the data jitters for RMS (root-mean-square) and PP (peak-to-peak) were about 24.5 ps and 184.9 ps, respectively; at 2.5 Gbps under 6 V, the data jitters for RMS and PP were about 31.0 ps and 204.4 ps, respectively.

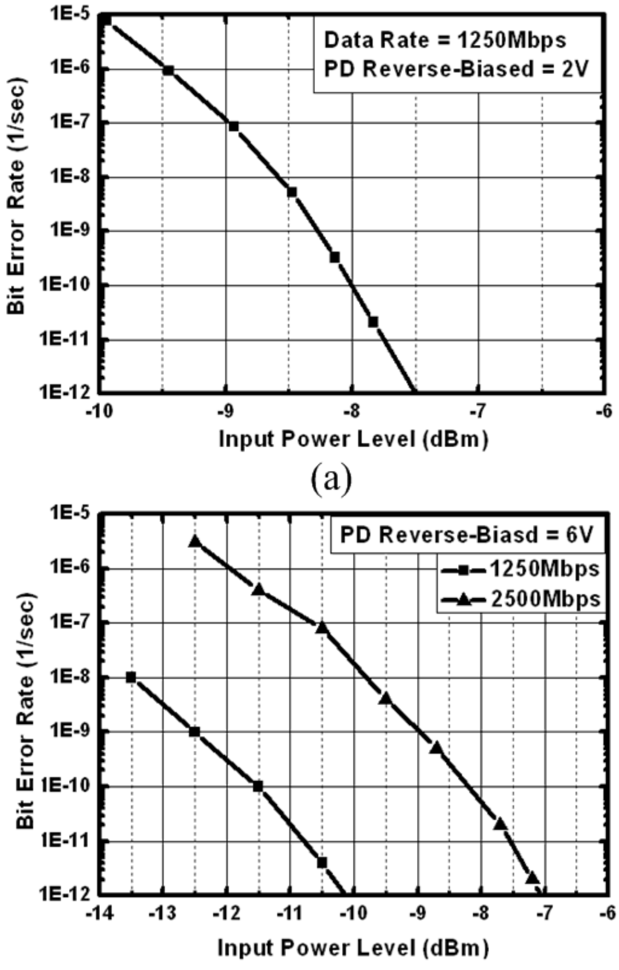

(a)

(b)

Figure 5-7: Measured Bit error rate performance under (a) 2 V and (b) 6V.

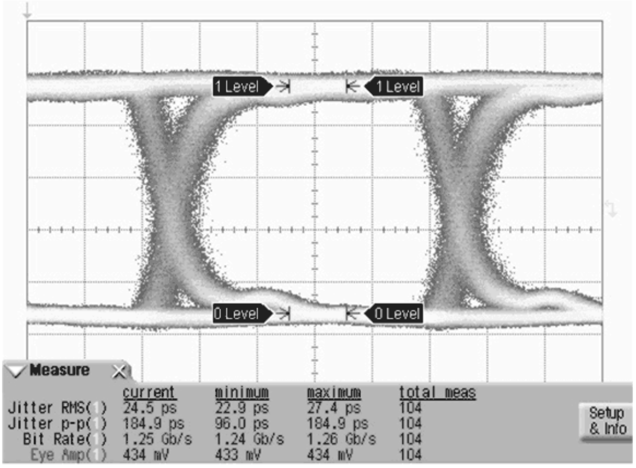

```
              current      minimum      maximum      total meas
Jitter RMS(1) 24.5 ps      22.9 ps      27.4 ps      104
Jitter p-p(1) 184.9 ps     96.0 ps      184.9 ps     104
  Bit Rate(1) 1.25 Gb/s    1.24 Gb/s    1.26 Gb/s    104
   Eye Amp(1) 434 mV       433 mV       434 mV       104
```

(a)

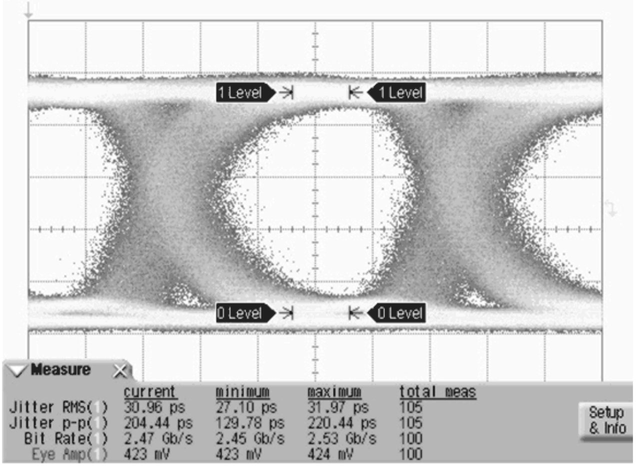

```
              current      minimum      maximum      total meas
Jitter RMS(1) 30.96 ps     27.10 ps     31.97 ps     105
Jitter p-p(1) 204.44 ps    129.78 ps    220.44 ps    105
  Bit Rate(1) 2.47 Gb/s    2.45 Gb/s    2.53 Gb/s    100
   Eye Amp(1) 423 mV       423 mV       424 mV       100
```

(b)

Figure 5-8: Measured eye diagram performance under 6 V: (a) at 1..25 Gbps and (b) at 2.5 Gbps.

5.4 Summary

This research presents the design of a 2.5-Gbps CMOS OEIC, which monolithically integrates a DNW-based PIN photodiode, a trans-impedance amplifier, and a limiting amplifier on a single chip. Incorporating with a novel lateral PIN photodiode, the optical receiver is capable of high-speed operation without an equalizer. By connecting the DNW to a positive supply voltage, the slowly diffusive carriers generated in P_{sub} are decoupled from the photocurrent of the PIN photodiode. A trans-impedance amplifier with pseudo-differential regulated cascode input stage is adopted to tolerate the large input capacitance. The gain cell in the limiting amplifier employs the active shunt-shunt feedback to have a wider gain-bandwidth product without inductive peaking. Measurement results indicated that this optical receiver is capable of operating up to 2.5 Gbps and delivering 800 $\mathrm{mV_{pp}}$ to 50-Ω output loads. With a 2^{31}-1 PRBS test pattern, the input sensitivity of the optical receiver is about -7 dBm for bit error rate (BER) less than 10^{-12}. The data jitters for RMS and PP were about 31.0 ps and 204.4 ps, respectively. The proposed CMOS OEIC manifests potential for the applications of short-range optical interconnects.

Chapter 6

Conclusion

6.1 Integrated CMOS Photodetectors for Biomedical Applications

Based on a standard CMOS technology and absorption photometry, two optical biosensing systems have been presented.

The biosensing system composed of an integrated photodiode and a TIA demonstrated a high sensitivity and linearity. By utilizing the interdigitated structure and removing the passivation layers, the quantum efficiency of the P^+/N_{well} photodiode was enhanced. For examining different concentration levels of an analyte, the switchable feedback resistance of the TIA allowed a user to adjust the amplification factor and the dynamic range. The ABTS/H_2O_2/HRP method was introduced as a useful basis to quantify various analytes that could produce H_2O_2 through biochemical reactions. Experimental results reveal that the detection limits of H_2O_2, glucose, and histamine concentration were 1 μM, 1 μM, and 10 μM, respectively. The detection limits are at least one order of magnitude better than those of reported CMOS biosensors, and are even comparable to those of a commercial spectrophotometer.

Another biosensing system composed of a PMOS phototransistor demonstrated a higher sensitivity and a lower sample-volume requirement. The whole system was assembled into a compact prototype, and the TMB/H_2O_2/HRP reaction was adopted as the basis for biomedical applications. This system exhibited a high detection capability of 2.5 μA/pM, a great detection limit of 2.7 pM, a large linear detection range from 2.7

to 212.8 pM, and a low required sample volume of 10 μl. In addition, to investigate the skin whitening mechanisms, three assays were performed: Melanin, MTT, and tyrosinase assays. The effect of the whitening agent kojic acid was also examined. Experimental results demonstrated that the density of 5×10^4 cells/ml can be successfully detected for these assays. Therefore, the miniature CMOS optical biosensing system has great potential toward a practical home care instrument for personalized clinical diagnosis and for evaluating the whitening reagent in the popular cosmetic industry.

6.2 Integrated CMOS Photodetectors for High-Speed Applications

The design, analysis, simulation, and measurement of two kinds of high-speed photodetectors have been presented.

The proposed meshed SMPD could achieve a faster photocurrent response than other reported CMOS photodetectors. This is because it more efficiently subtracts the deferred portion from the immediate portion of the photocurrent, and more efficiently weakens the influences of the diffusion current coming from the neutral N_{well} regions. Among the CMOS photodetectors utilizing various structures and P/N junctions, the N_{well}/P_{sub} meshed SMPD accomplishes the largest GBW, and the measurement results demonstrated a 3-dB bandwidth of 5.5 GHz. This bandwidth will be further improved when using a more advanced CMOS technology.

Another proposed optical receiver, composed of a DNW-based PIN photodiode, a trans-impedance amplifier, and a limiting amplifier, is capable of high speed operation without an equalizer. The proposed lateral PIN photodiode was emulated by a $P^+/P_{well}/N^+$ interleaved architecture, and the increased depletion region indeed improved the responsivity. By connecting the DNW to a positive supply voltage, the slowly diffusive carriers generated in P_{sub} are decoupled from the photocurrent of the PIN detector. Measurement results indicated that this optical receiver is capable of operating up to 2.5 Gbps and delivering 800 mV_{pp} to 50-Ω output loads. This optical receiver manifests potential for the applications of short range optical interconnect.

6.3 Future Work

In the future, the photodetector having both high gain and high bandwidth could be expected. By combining the operating mechanism of the DNW-based photodiode, the spatially modulated photodiode (SMPD), and the phototransistor (PT), a device structure named DNW-based spatially modulated phototransistor (SMPT) is proposed. The top view and cross section are depicted in Figure 6-1. G_i, S_i, and D_i respectively represent the gate, source, and drain of the phototransistor that provides the relatively immediate photocurrent; G_d, S_d, and D_d respectively represent the gate, source, and drain of the phototransistor that provides the relatively deferred photocurrent; B and R represent the common floating bulk and the common outer ring, respectively.

The operating mechanism of this SMPT is described as follows. (i) By connecting the DNW to a positive supply voltage, the slowly diffusive carriers generated in P_{sub} can be decoupled from the photocurrent. (ii) By subtracting the deferred portion from the immediate portion of the photocurrent, the slowly diffusive effect in P_{well} can be alleviated. (iii) Through the internal transistor action under moderate bias, the phototransistor can have a photocurrent amplification. Therefore, the SMPT would be an attractive candidate to achieve a high speed and a high responsivity at the same time.

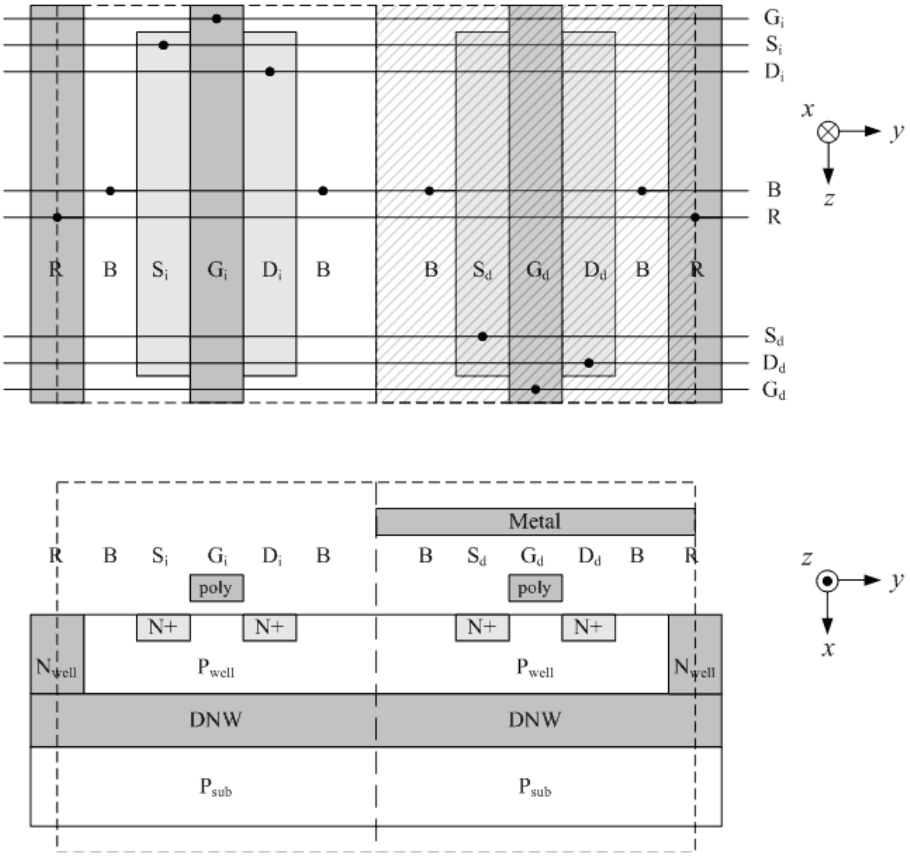

Figure 6-1: The top view and cross section of the proposed SMPT to have a high gain and a high bandwidth.

Bibliography

[1] H. Zimmermamn, *Integrated Silicon Optoelectronics*, Springer, 2000.

[2] S. Donati, *Photodetectors – Devices, Circuits, and Applications*, Prentice-Hall, 2000.

[3] R. F. Wplffenbuttel, *Silicon Sensors and Circuits – On-Chip Compatibility*, Chapman & Hall, 1996.

[4] W.-J. Ho, J.-S. Chen, M.-D. Ker, T.-K. Wu, C.-Y. Wu, Y.-S. Yang, Y.-K. Li, and C.-J. Yuan, "Fabrication of a Miniature CMOS-based Optical Biosensor," *Biosens. Bioelectron.*, vol. 22, pp. 3008–3013, 2007.

[5] U. Lu, B. C.-P. Hu, Y.-C. Shih, C.-Y. Wu, and Y.-S. Yang, "The Design of a Novel Complementary Metal Oxide Semiconductor Detection System for Biochemical Luminescence," *Biosens. Bioelectron.*, vol. 19, pp. 1185–1191, 2004.

[6] R. Eisenthal and M. J. Danson, *Enzyme Assays :A Practical Approach*, 2nd Ed., Oxford University Press, 2002.

[7] R. A. Yotter, L. A. Lee, and D. M. Wilson, "Sensor technologies for monitoring metabolic activity in single cells–part I: optical methods," *IEEE Sensors J.*, vol. 4, pp. 395–411, 2004.

[8] U. Lu, B. C.-P. Hu, Y.-C. Shih, Y.-S. Yang, C.-Y. Wu, C.-J. Yuan, M.-D. Ker, T.-K. Wu, Y.-K. Li, Y.-Z. Hsieh, W. Hsu, and C.-T. Lin, "CMOS chip as luminescent sensor for biochemical reactions," *IEEE Sensors J.*, vol. 3, pp. 310–316, 2003.

[9] R. A. Yotter and D. M. Wilson, "A review of photodetectors for sensing light-emitting reporters in biological systems," *IEEE Sensors J.*, vol. 3, pp. 288–303, 2003.

[10] V. P. Chodavarapu, D. O. Shubin, R. M. Bukowski, E. C. Tehan, A. H. Titus, A. N. Cartwright, and F. V. Bright, "CMOS-based biosensor systems using integrated nanostructured recognition elements," *Proc. SPIE*, vol. 6095, pp. 126–133, 2006.

[11] A. C. Pimentel, A. T. Pereira, V. Chu, D. M. F. Prazeres, and J. P. Conde, "Detection of Chemiluminescence Using an Amorphous Silicon Photodiode," *IEEE Sensors J.*, vol. 7, pp. 415–416, 2007.

[12] S.-H. Huanga, Y.-C. Shih, C.-Y. Wu, C.-J. Yuan, Y.-S. Yang, Y.-K. Li, and T.-K. Wu, "Detection of serum uric acid using the optical polymeric enzyme biochip system," *Biosens. Bioelectron.*, vol. 19, pp. 1627–1633, 2004.

[13] D. A. B. Miller, "Rationale and challenges for optical interconnects to electronic chips," *Proc. IEEE*, vol. 88, pp. 728–749, 2000.

[14] M. Haurylau, G. Chen, H. Chen, J. Zhang, N. A. Nelson, D. H. Albonesi, E. G. Friedman, and P. M. Fauchet, "On-chip optical interconnect roadmap: challenges and critical directions," *IEEE J. Sel. Top. Quantum Electron.*, vol. 12, pp. 1699–1705, 2006.

[15] A. Ghazi, H. Zimmermann, and P. Seegebrecht, "CMOS photodiode with enhanced responsivity for the UV/blue spectral range," *IEEE Trans. Electron Devices*, vol. 49, pp. 1124–1128, 2002.

[16] S. Radovanovic, A. J. Annema, and B. Nauta, "A 3-Gb/s optical detector in standard CMOS for 850-nm optical communication," *IEEE J. Solid-State Circuit*, vol. 40, pp. 1706–1717, 2005.

[17] M. Kuijk, D. Coppee, and R. Vounckx, "Spatially modulated light detector in CMOS with sense-amplifier receiver operating at 180 Mbps for optical data link applications and parallel optical interconnects between chips," *IEEE J. Sel. Top. Quantum Electron.*, vol. 4, p. 1040, 1998.

[18] J. Genoe, D. Coppee, J. H. Stiens, R. A. Vounckx, and M. Kuijk, "Calculation of the current response of the spatially modulated light CMOS detector," *IEEE Trans. Electron Devices*, vol. 48, pp. 1892–1902, 2001.

[19] M. Jutzi, M. Grozing, E. Gaugler, W. Mazioschek, and M. Berroth, “2-gb/s CMOS optical integrated receiver with a spatially Modulated photodetector,” *IEEE Photonics Techn. Letters*, vol. 17, pp. 1268–1270, 2005.

[20] M. Gr̋oing, M. Jutzi, W. Nanz, and M. Berroth, “A 2 Gbit/s 0.18 μm CMOS front-end amplifier for integrated differential photodiodes,” *Topical Meeting on Silicon Monolithic Integrated Circuits in RF Systems*, pp. 361–364, 2006.

[21] Y.-W. Chang, P.-C. Yu, Y.-T. Huang, and Y.-S. Yang, “A high-sensitivity CMOS-compatible biosensing system based on absorption photometry,” *IEEE Sensors J.*, vol. 9, pp. 120-127, 2009.

[22] P. N. Campbell, A. D. Smith, T. J. Peters, *Biochemistry illustrated :biochemistry and molecular biology in the post-genomic era*, 5th Ed., Elsevier Churchill Livingstone, 2005.

[23] R. Bourbonnais, D. Leech, and M.G. Paice, “Electrochemical analysis of the interactions of laccase mediators with lignin model compounds,” *Biochimica et Biophysica Acta*, vol. 1379, pp. 381–390, 1998.

[24] E. C. Webb, *Enzyme nomenclature 1992*, Academic Press, 1992.

[25] A. Ghazi, H. Zimmermann, and P. Seegebrecht, “CMOS photodiode with enhanced responsivity for the UV/blue spectral range,” *IEEE Trans. Electron Devices*, vol. 49, pp. 1124–1128, 2002.

[26] M.-D. Ker and W.-Y. Lo, “Methodology on extracting compact layout rules for latchup prevention in deep-submicron bulk CMOS technology,” *IEEE Trans. Semicond. Manuf.*, vol. 16, pp. 319–334, 2003.

[27] D. K. Cheng, *Field and Wave Electronmagnetics*, Addison-Wesley, 1989.

[28] B. Razavi, *Design of Integrated Circuits for Optical Communications*, McGrw-Hill, 2003.

[29] L. Zhu, R. Yang, J. Zhai, and C. Tian, “Bienzymatic glucose biosensor based on co-immobilization of peroxidase and glucose oxidase on a carbon nanotubes electrode,” *Biosens. Bioelectron.*, vol. 23, pp. 528–535, 2007.

[30] D. L. Sherman, J. F. Keaney, E. S. Biegelsen, S. J. Duffy, J. D. Coffman, and J. A. Vita, “Pharmacological Concentrations of Ascorbic Acid Are Required for the Beneficial Effect on Endothelial Vasomotor Function in Hypertension,” *J. American Heart Association*, vol. 35, pp. 936–941, 2000.

[31] S. M. Sze and K. K. NG, *Physics of Semiconductor Devices*, 3rd ed., John Wiley & Sons, 2007.

[32] Y.-W. Chang, Y.-T. Tai, Y.-T. Huang, and Y.-S. Yang, “A phototransistor-based high-sensitivity biosensing system using 650-nm light,” *IEEE Sensors J.*, vol. 9, pp. 673-677, 2009.

[33] N. C. Veitch, “Horseradish peroxidase: a modern view of a classic enzyme,” *Phytochemistry*, vol. 65, pp. 249–259, 2004.

[34] P. D. Josephy, T. Eling and R. P. Mason, “The horseradish peroxidase-catalyzed oxidation of 3,5,3’,5’-tetramethylbenzidine”, *J. Biological Chemistry*, vol. 257, pp. 3669–3675, 1982.

[35] E. S. Bos, A. A. van der Doelen, N. van Rooy, and A. H. W. M. Schuurs, “3,3’,5,5’-tetramethylbenzidine as an ames test negative chromogen for horse-radish peroxidase in enzyme-immunoassay,” *J. Immunoassay and Immunochemistry*, vol. 2, pp. 187–204, 1981.

[36] P. Fanjul-Bolado, M. B. Gonzălez-Garcĭa, and A. Costa-Garcĭa, “Amperometric detection in TMB/HRP-based assays”, *Analytical and Bioanalytical Chemistry*, vol. 382, pp. 297–302, 2005.

[37] B. Mecheri, L. Piras, L. Ciotti, and G. Caminati, “Electrode coating with ultrathin films containing electroactive molecules for biosensor applications,” *IEEE Sensors J.*, vol. 4, pp. 171–179, 2004.

[38] M. Schanz, W. Brockherde, R. Hauschild, B. J. Hosticka, and A. Teuner, “CMOS photosensor arrays with on-chip signal processing,” in *Proc. European Solid-State Circuits Conf.*, 1997, pp. 236–239.

[39] N. Wang and D. N. Hebert, “Tyrosinase maturation through the mammalian secretory pathway: bringing color to life,” *Pigment Cell Res.*, vol. 19, pp. 3-18, 2006.

[40] Y. J. Kim, "Antimelanogenic and antioxidant properties of gallic acid," *Biol. Pharm. Bull.*, vol. 30, pp. 1052-1055, 2007.

[41] J. Sturm, M. Leifhelm, H. Schatzmayr, S. Groiß, and H. Zimmermann,"Optical Receiver IC for CD/DVD/Blue-Laser Application," *IEEE J. Solid-State Circuits*, vol. 40, pp. 1406–1413, 2005.

[42] A. Nemecek, G. Zach, R. Swoboda, K. Oberhauser, and H. Zimmermann, "Integrated BiCMOS p-i-n photodetectors with high bandwidth and high responsivity," *IEEE J. Selected Topics in Quantum Electronics*, vol. 12, pp. 1469–1475, 2006.

[43] W. Zhang, M. Chan, S. K. H. Fung, and P. K. Ko, "Performance of a CMOS compatible lateral bipolar photodetector on SOI substrate," *IEEE Electron Device Letters*, vol. 19, pp. 435–437, 1998.

[44] M. A. Marwick and A. G. Andreou, "A UV photodetector with internal gain fabricated in silicon on sapphire CMOS," *IEEE Sensors conf.*, pp. 535–538, 2007.

[45] W. Zhang and M. Chan, "A high gain n-well/gate tied PMOSFET image sensor fabricated from a standard CMOS process," *IEEE Trans. Electron Devices*, vol. 48, pp. 1097–1102, 2001.

[46] M. Schanz, W. Brockherde, R. Hauschild, B. J. Hosticka, and A. Teuner, "CMOS photosensor arrays with on-chip signal processing," in *Proc. 23rd European Solid-State Circuits Conf.*, pp. 236–239, 1997.

[47] A. Ghazi, H. Zimmermann, P. Seegebrecht, "CMOS photodiode with enhanced responsivity for the UV/blue spectral range," *IEEE Trans. Electron Devices*, vol. 49, pp. 1124–1128, 2002.

[48] A. Tibuzzi, G.-F. D. Bettaa, C. Piemontea, C. D. Natalea, A. D' Amicoa, and G. Soncinia, "High gain bipolar junction phototransistors with finger-shaped emitter for improved optical gas sensing in the blue spectral region," *Sensors and Actuators A: Physical*, vol. 136, pp. 588-596, 2007.

[49] A. R. Pauchard, P.-A. Besse, and R. S. Popovic, "Dead space effect on the wavelength dependence of gain and noise in avalanche photodiodes," *IEEE Trans. Electron Devices*, vol. 47, pp. 1685–1693, 2000.

[50] W. J. Liu, O. T. C. Chen, L. K. Dai, P. K. Weng, K. H. Huang, and F. W. Jih, "A CMOS photodiode model," in *Proc. Fifth IEEE International Workshop Behavioral Modeling and Simulation*, pp. 102-105, 2001.

[51] B. L. Anderson and R. L . Anderson, *Fundamentals of Semiconductor Device*, McGraw-Hill, 2005.

[52] W. Z. Chen, Y. L. Cheng, and D. S. Lin, "A 1.8-V 10-Gb/s fully integrated CMOS optical receiver analog front-end," *IEEE J. Solid-State Circuits*, vol. 40, pp. 1388–1396, 2005.

[53] C. Hermans and M. S. J. Steyaert, "A High-Speed 850-nm Optical Receiver Front-end in 0.18-μm CMOS," *IEEE J. Solid-State Circuits*, vol. 41, no. 7, pp. 1606-1614, 2006.

[54] C. Rooman, D. Coppee, and M. Kuijk, "Asynchronous 250 Mb/s Optical Receivers with Integrated Detector in Standard CMOS Technology," *IEEE J. Solid-State Circuits*, vol. 35, no., 7, pp. 953-958, 2000.

[55] T. K Woodward and A. V. Krishnamoorthy, " 1-Gb/s integrated optical detectoprs and receivers in commercial CMOS technologies," *IEEE J. Sel. Topics Quantum Electron.*, vol. 5, no. 2, pp.146-156, 1999.

[56] M. Ghioni, F. Zappa, V. P. Kesan, and J. Warnock, "A VLSI compatible high speed silicon photo detector for optical datalink application," *IEEE Trans. Electron Devices*, vol. 43, no. 7, pp. 1054-1060, 1996.

[57] S. M. Csutak, J. D. Schaub, W. E. Wu, and J. C. Champbell, "High-speed monolithically integrated silicon photoreceivers fabricated in 130-nm CMOS technology," *IEEE Photon. Technol. Lett.*, vol. 14, no. 4, pp. 516-518, 2002.

[58] S. Radovanović, A.-J. Annema, and B. Nauta, " A 3-Gb/s Optical Receiver Front-end in 0.18 μm CMOS," *IEEE J. Solid-State Circuits*, vol. 40, no. 8, pp. 1706-1717, 2005.

[59] J.-G. Su, H.-M. Hsu, S.-C. Wong, C.-Y. Chang, T.-Y. Huang, and J. Y.-C. Sun, "Improving the RF performance of 0.18 μm CMOS with deep n-well implantation," *IEEE Electron Device Lett.*, vol. 22, pp. 481-483, 2001.

[60] S. M. Park and H.-J. Yoo, “1.25 Gb/s regulated cascode CMOS transimpedance amplifier for gigabit ethernet applications,” *IEEE J. Solid-State Circuits*, pp.112–121, 2004.

Appendix

Theoretical Derivation of the Photocurrent

1 Basic Equations

For the unshaded area, the incident photon flux density in the frequncy domain ($s = jw$) is given by

$$\Phi_0(s) = \frac{P_{opt}(s)}{A}\frac{\lambda}{hc}(1 - R), \tag{1}$$

where $P_{opt}(s)$ is the input optical power, A is the device area, λ is the wavelength of the incident light, h is the Plank's constant, c is the speed of light, and R is the reflectance. The electron-hole generation rate from optical excitation is given by

$$G(x, s) = \alpha\Phi_0(s)e^{-\alpha x}, \tag{2}$$

where α is the absorption coefficient. The total photocurrent is contributed from two different regions: the depletion regions and the neutral regions. In a depletion region, the photocurrent density is mainly contributed by the drift current density, given by

$$\mathbf{J}_{dr}(\mathbf{s}) = q\int G(x, s)d\mathbf{r}. \tag{3}$$

Then the drift current can be obtained by taking surface integrals as

$$I_{dr}(s) = \int \mathbf{J}_{dr}(\mathbf{s}) \cdot d\mathbf{s}. \tag{4a}$$

In a neutral region, the electric field is negligible and thus the photocurrent density is mainly contributed by the diffusion current density. Therefore, the continuity equations of these photogenerated carriers in the frequency domain can be written as

$$\begin{aligned} sN_p &= G - \frac{N_p}{\tau_n} + D_n\nabla^2 N_p, && \text{(5a)} \\ sP_n &= G - \frac{P_n}{\tau_p} + D_p\nabla^2 P_n, && \text{(5b)} \end{aligned}$$

where N_p is the electron concentration in the p-type material, and P_n is the hole concentration in teh n-type material; τ_p and τ_n are the carrier lifetimes for electrons and holes,

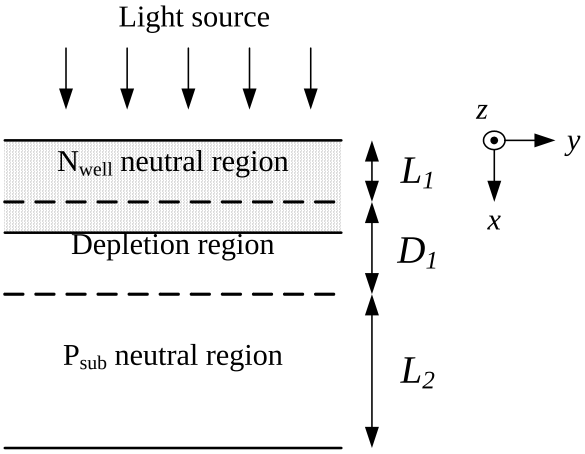

Figure 1: Cross section of a single photodiode.

respectively; D_n and D_p are the diffusion constants for electrons and holes, respectively. Combining the continuity equations in Eqs. (5a) and (5b) with the boundary conditions yields the minority carrier concentrations N_p and P_n, and the electron and hole diffusion current density can be obtained as

$$\mathbf{J}_n(s) = qD_n\nabla N_p, \tag{6a}$$

$$\mathbf{J}_p(s) = -qD_p\nabla P_n. \tag{6b}$$

Then the electron and hole diffusion currents can be obtained by taking surface integrals as

$$I_n(s) = \int \mathbf{J}_n(s)\cdot d\mathbf{s}, \tag{7a}$$

$$I_p(s) = \int \mathbf{J}_p(s)\cdot d\mathbf{s}. \tag{7b}$$

2 Single Photodiode

Consider a single photodiode structure shown in Fig. 1. The generation rates of carriers per unit volume in the time-domain and frequency-domain are

$$g(x,t) = \alpha\Phi_0(t)e^{-\alpha x}, \tag{8}$$

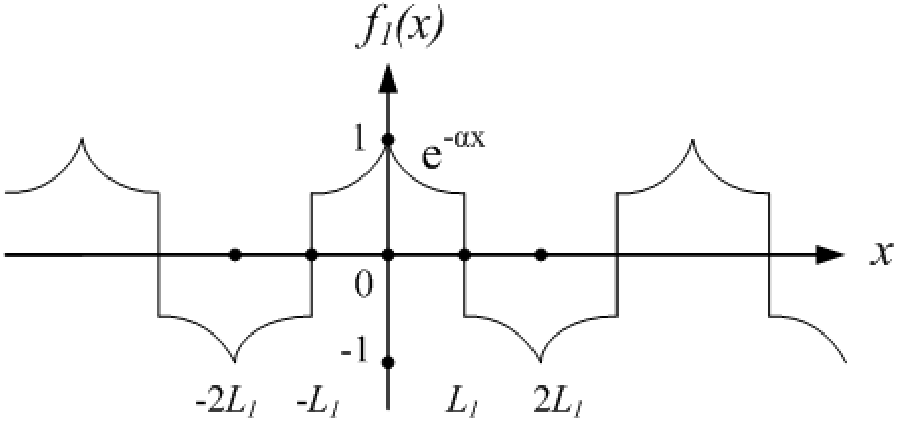

Figure 2: Waveform of $f_1(x)$

$$G(x,s) = \alpha\Phi_0(s)e^{-\alpha x}. \tag{9}$$

2.1 N-type Neutral Region

In the N-type neutral region, the continuity equations for holes in the time-domain and frequency-domain are

$$\frac{\partial p_n(x,t)}{\partial t} = D_p\frac{\partial^2 p_n(x,t)}{\partial x^2} - \frac{p_n(x,t)}{\tau_p} + g(x,t), \tag{10}$$

$$sP_n(x,s) = D_p\frac{\partial^2 P_n(x,s)}{\partial x^2} - \frac{P_n(x,s)}{\tau_p} + G(x,s), \tag{11}$$

and the boundary conditions are

$$\left.\frac{\partial p_n}{\partial x}\right|_{x=0} = 0, \quad p_n|_{x=L_1} = 0. \tag{12}$$

A function $f_1(x)$ shown in Fig. 2 can satisfy the boundary conditions and is equal to $e^{-\alpha x}$ for $0 \le x \le L_1$.

Since the Fourier series coefficeint A_m can be evaluated as

$$
\begin{aligned}
A_m &= \frac{2}{2L_1}\int_0^{2L_1} f_1(x)\cos\left[\frac{m\pi}{2L_1}x\right]dx \\
&= \frac{(2m-1)\pi(-1)^{m+1}e^{-\alpha L_1}+2\alpha L_1}{(\alpha L_1)^2+\left[\frac{(2m-1)\pi}{2}\right]^2},
\end{aligned}
\tag{13}
$$

$e^{-\alpha x}$ can be expressed as

$$
e^{-\alpha x} = \sum_{m=1}^{\infty} A_m \cos\left[\frac{(2m-1)\,\pi}{2L_1}x\right],\ \text{for } 0 \leq x \leq L_1, \tag{14}
$$

and then $G(x,s)$ can be expressed as

$$
G(x,s) = \alpha\Phi_0(s)\sum_{m=1}^{\infty} A_m \cos\left[\frac{(2m-1)\,\pi}{2L_1}x\right], for 0 \leq x \leq L_1. \tag{15}
$$

Thus, $P_n(x,s)$ can be expressed as

$$
P_n(x,s) = \alpha\Phi_0(s)\sum_{m=1}^{\infty} a_m \cos\left[\frac{(2m-1)\,\pi}{2L_1}x\right],\ \text{for } 0 \leq x \leq L_1, \tag{16}
$$

where a_m can be evaluated as

$$
a_m = \frac{A_m}{s + D_p\left[\frac{(2m-1)\pi}{2L_1}\right]^2 + \frac{1}{\tau_p}}. \tag{17}
$$

The diffusion current in the N-type neutral region is then obtained as

$$
\begin{aligned}
I_p(s) &= -AqD_p\left.\frac{\partial P_n(x,s)}{\partial x}\right|_{x=L_1} \\
&= \sum_{m=1}^{\infty} AqD_p\alpha\Phi_0(s)a_m\frac{(2m-1)\,\pi}{2L_1}(-1)^{m+1} \\
&= \sum_{m=1}^{\infty} AqD_p\alpha\Phi_0(s)\frac{1}{s + D_p\left[\frac{(2m-1)\pi}{2L_1}\right]^2 + \frac{1}{\tau_p}} \\
&\quad \times\frac{(2m-1)\pi(-1)^{m+1}e^{-\alpha L_1}+2\alpha L_1}{(\alpha L_1)^2+\left[\frac{(2m-1)\pi}{2}\right]^2}\times\frac{(2m-1)\,\pi}{2L_1}(-1)^{m+1}.
\end{aligned}
\tag{18}
$$

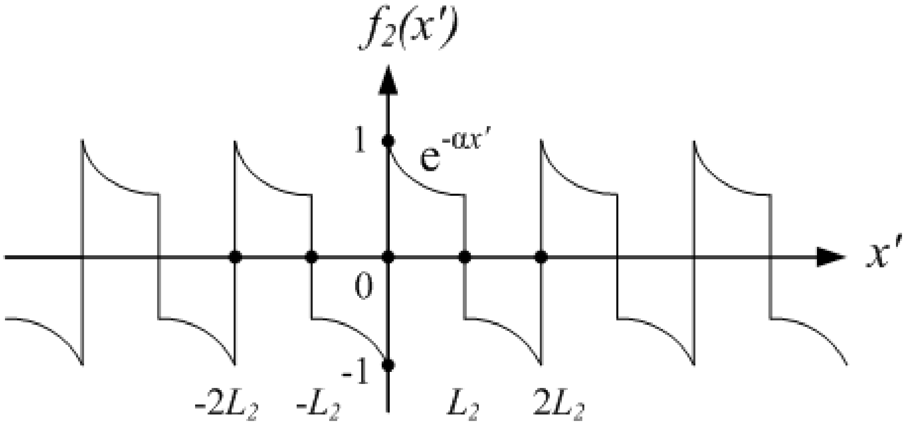

Figure 3: Waveform of $f_2(x')$

2.2 P-type Neutral Region

In the P-type neutral region, the continuity equation for electrons in the time-domain and frequency-domain are

$$\frac{\partial n_p(x',t)}{\partial t} = D_n \frac{\partial^2 n_p(x',t)}{\partial x'^2} - \frac{n_p(x',t)}{\tau_n} + g(x',t), \tag{19}$$

$$sN_p(x',s) = D_n \frac{\partial^2 N_p(x',s)}{\partial x'^2} - \frac{N_p(x',s)}{\tau_n} + G(x',s), \tag{20}$$

and the boundary conditions are

$$n_p|_{x'=0} = 0, \quad n_p|_{x'=L_2} = 0, \tag{21}$$

where $x' = x - (L_1 + D_1)$.

A function $f_2(x')$ shown in Fig. 3 can satisfy the boundary conditions and is equal to $e^{-\alpha x'}$ for $0 \leq x' \leq L_2$.

Since the Fourier series coefficeint B_m can be evaluated as

$$\begin{aligned} B_m &= \frac{2}{L_2} \int_0^{L_2} f_2(x') \sin\left(\frac{m\pi}{L_2} x\right) dx' \\ &= \frac{2m\pi\left[1 - (-1)^m e^{-\alpha L_2}\right]}{(\alpha L_2)^2 + (m\pi)^2}, \end{aligned} \tag{22}$$

$e^{-\alpha x'}$ can be expressed as

$$e^{-\alpha x'} = \sum_{m=1}^{\infty} B_m \sin\left(\frac{m\pi}{L_2} x'\right), \text{ for } 0 \leq x' \leq L_2, \tag{23}$$

and then $G(x', s)$ can be expressed as

$$G(x', s) = \alpha \Phi_0(s) e^{-\alpha(L_1+D_1)} \sum_{m=1}^{\infty} B_m \sin\left(\frac{m\pi}{L_2} x'\right), \text{ for } 0 \leq x' \leq L_2. \tag{24}$$

Thus, $N_p(x', s)$ can be expressed as

$$N_p(x', s) = \alpha \Phi_0(s) e^{-\alpha(L_1+D_1)} \sum_{m=1}^{\infty} b_m \sin\left(\frac{m\pi}{L_2} x'\right), \text{ for } 0 \leq x' \leq L_2, \tag{25}$$

where b_m can be evaluated as

$$b_m = \frac{B_m}{s + D_n \left(\frac{m\pi}{L_2}\right)^2 + \frac{1}{\tau_n}}. \tag{26}$$

The diffusion current in the P-type neutral region is then obtained as

$$\begin{aligned}
I_n(s) &= AqD_n \left.\frac{\partial N_p(x', s)}{\partial x'}\right|_{x'=0} \\
&= \sum_{m=1}^{\infty} AqD_n \alpha \Phi_0(s) e^{-\alpha(L_1+D_1)} b_m \frac{m\pi}{L_2} \\
&= \sum_{m=1}^{\infty} AqD_n \alpha \Phi_0(s) e^{-\alpha(L_1+D_1)} \frac{1}{s + D_n \left(\frac{m\pi}{L_2}\right)^2 + \frac{1}{\tau_n}} \\
&\quad \times \frac{2m\pi \left[1 - (-1)^m e^{-\alpha L_2}\right]}{(\alpha L_2)^2 + (m\pi)^2} \times \frac{m\pi}{L_2}.
\end{aligned} \tag{27}$$

2.3 Depletion Region

In the depletion region, the drift current is

$$\begin{aligned}
I_{dr}(s) &= A \int_{L_1}^{L_1+D_1} qG(x, s) dx \\
&= Aq\Phi_0(s) \left[e^{-\alpha L_1} - e^{-\alpha(L_1+D_1)}\right].
\end{aligned} \tag{28}$$

2.4 Total Current

The output current $I_o(s)$ is

$$I_o(s) = I_p(s) + I_n(s) + I_{dr}(s). \tag{29}$$

3 Finger Photodiode

Consider a figer photodiode shown in Fig. 4. The generation rates of carriers per unit volume in the time-domain and frequency-domain are

$$g(x,y,t) = \alpha\Phi_0(t)e^{-\alpha x}f(y), \tag{30}$$

$$G(x,y,s) = \alpha\Phi_0(s)e^{-\alpha x}f(y). \tag{31}$$

3.1 N-type Neutral Region

In the N-type neutral region, the continuity equations for holes in the time-domain and frequency-domain are

$$\frac{\partial p_n(x,y,t)}{\partial t} = D_p\frac{\partial^2 p_n(x,y,t)}{\partial x^2} + D_p\frac{\partial^2 p_n(x,y,t)}{\partial y^2} - \frac{p_n(x,y,t)}{\tau_p} + g(x,y,t), \tag{32}$$

$$sP_n(x,y,s) = D_p\frac{\partial^2 P_n(x,y,s)}{\partial x^2} + D_p\frac{\partial^2 P_n(x,y,s)}{\partial y^2} - \frac{P_n(x,y,s)}{\tau_p} + G(x,y,s), \tag{33}$$

and the boundary conditions are

$$\begin{aligned} \left.\frac{\partial p_n}{\partial x}\right|_{x=0} &= 0, \quad p_n|_{x=L_1} = 0, & (34)\\ p_n|_{y=0} &= 0, \quad p_n|_{y=L'_Y} = 0, \text{ for } 0 \le x \le L_1. & (35) \end{aligned}$$

A function $f_3(y)$ shown in Fig. 5 can satisfy the boundary conditions for $0 \le x \le L_1$.Since

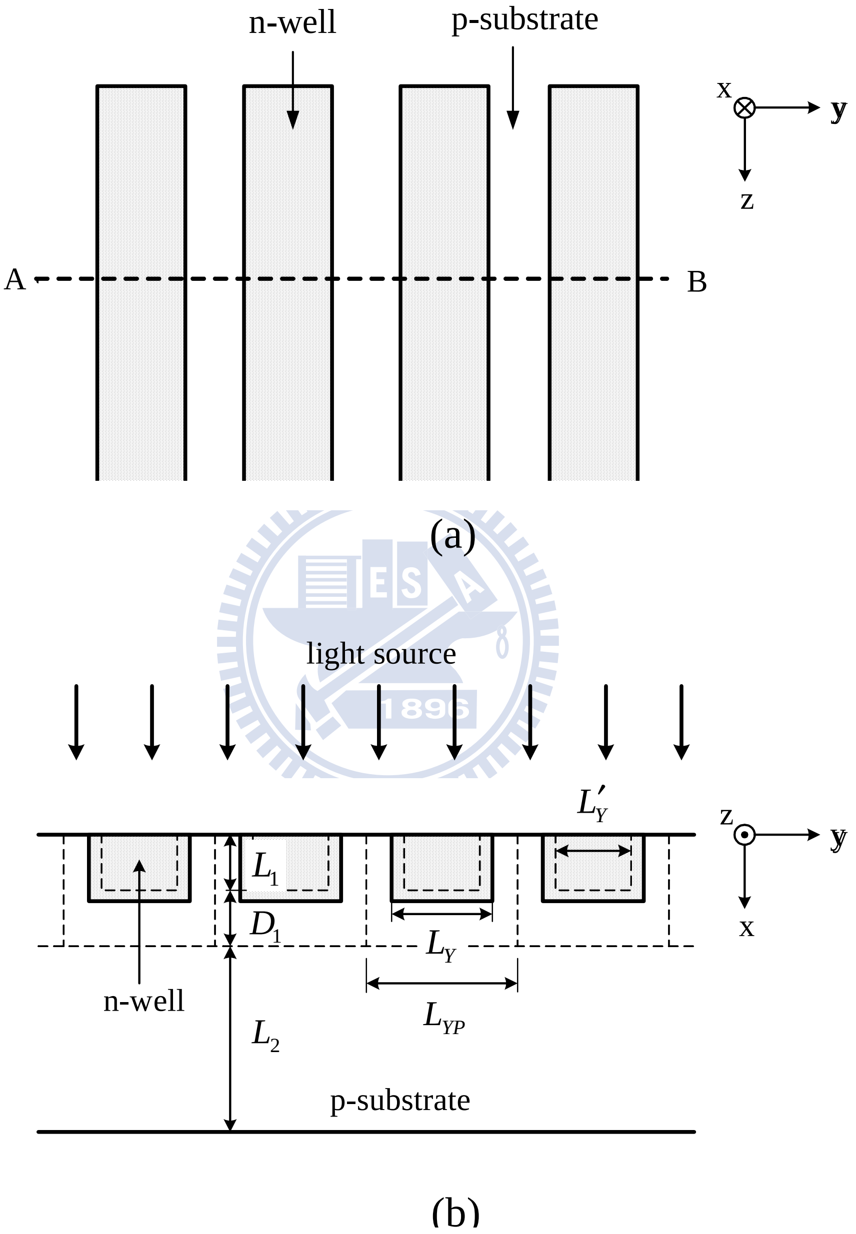

Figure 4: Finger photodiode, (a) top view, (b) cross section along line $\overline{AB}$.

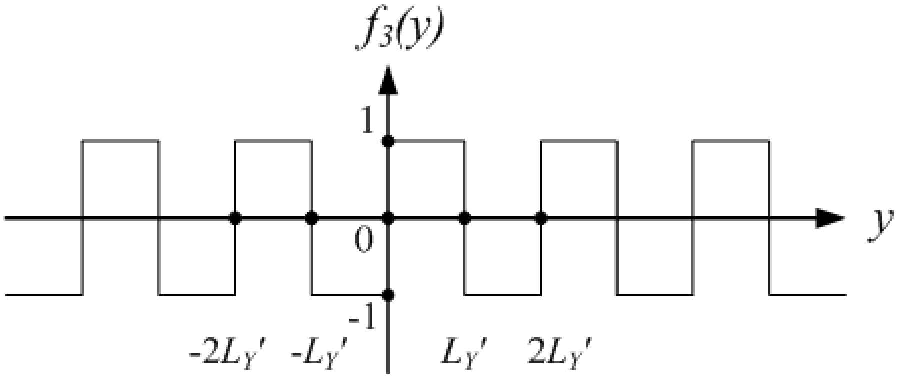

Figure 5: Waveform of $f_3(y)$

the Fourier series coefficeint A_n can be evaluated as

$$\begin{aligned} A_n &= \frac{2}{L'_y}\int_0^{L'_Y} f_3(y)\sin\left[\frac{n\pi}{L'_y}y\right]dy \\ &= \frac{4}{(2n-1)\pi}, \end{aligned} \tag{36}$$

$f_3(y)$ can be expressed as

$$f_3(y) = \sum_{n=1}^{\infty} A_n \sin\left[\frac{(2n-1)\pi}{L'_Y}y\right], \text{ for } 0 \le x \le L_1, \tag{37}$$

and then $G(x,y,s)$ can be expressed as

$$G(x,y,s) = \alpha\Phi_0(s)\sum_{m=1}^{\infty} A_m \cos\left[\frac{(2m-1)\,\pi}{2L_1}x\right] f_3(y), \text{ for } 0 \le x \le L_1. \tag{38}$$

Thus, $P_n(x,y,s)$ can be expressed as

$$P_n(x,y,s) = \alpha\Phi_0(s)\sum_{m=1}^{\infty}\sum_{n=1}^{\infty} a_{mn}\cos\left[\frac{(2m-1)\,\pi}{2L_1}x\right]\sin\left[\frac{(2n-1)\pi}{L'_Y}y\right], \text{for } 0 \le x \le L_1, \tag{39}$$

where a_{mn} can be evaluated as

$$a_{mn} = \frac{A_m A_n}{s + D_p\left[\frac{(2m-1)\pi}{2L_1}\right]^2 + D_p\left[\frac{(2n-1)\pi}{L'_Y}\right]^2 + \frac{1}{\tau_p}}. \tag{40}$$

The diffusion current $I_p(s)$ in the N-type neutral region is then obtained as

$$\begin{aligned} I_p(s) &= -AqD_p\frac{1}{L_{YP}}\left[\int_0^{L_Y'}\left.\frac{\partial P_n}{\partial x}\right|_{x=L_1}dy+\int_0^{L_1}-\left.\frac{\partial P_n}{\partial y}\right|_{y=0}dx+\int_0^{L_1}\left.\frac{\partial P_n}{\partial y}\right|_{y=L_Y'}dx\right] \\ &= \sum_{m=1}^{\infty}\sum_{n=1}^{\infty}\frac{A}{L_{YP}}qD_p\alpha\Phi_0(s)a_{mn}(-1)^{m+1}\left[\frac{L_Y'}{L_1}\frac{2m-1}{2n-1}+\frac{L_1}{L_Y'}\frac{4\,(2n-1)}{2m-1}\right] \\ &= \sum_{m=1}^{\infty}\sum_{n=1}^{\infty}\frac{A}{L_{YP}}qD_p\alpha\Phi_0(s)\frac{1}{s+D_p\left[\frac{(2m-1)\pi}{2L_1}\right]^2+D_p\left[\frac{(2n-1)\pi}{L_Y'}\right]^2+\frac{1}{\tau_p}}\times\frac{4(-1)^{m+1}}{(2n-1)\pi} \\ &\quad\times\frac{(2m-1)\pi(-1)^{m+1}e^{-\alpha L_1}+2\alpha L_1}{(\alpha L_1)^2+\left[\frac{(2m-1)\pi}{2}\right]^2}\times\left[\frac{L_Y'}{L_1}\frac{2m-1}{2n-1}+\frac{L_1}{L_Y'}\frac{4\,(2n-1)}{2m-1}\right]. \qquad (41) \end{aligned}$$

3.2 P-type Neutral Region

In the P-type neutral region, the boundary conditions are similar to the case in a single photodiode. Therefore, the diffusion current in the P-type neutral region is obtained as

$$I_n(s)=\sum_{m=1}^{\infty}AqD_n\alpha\Phi_0(s)e^{-\alpha(L_1+D_1)}\frac{1}{s+D_n\left(\frac{m\pi}{L_2}\right)^2+\frac{1}{\tau_n}}\times\frac{2m\pi\left[1-(-1)^m e^{-\alpha L_2}\right]}{(\alpha L_2)^2+(m\pi)^2}\times\frac{m\pi}{L_2}. \qquad (42)$$

3.3 Depletion Region

In the depletion region, the drift current $I_{dr}(s)$ is

$$\begin{aligned} I_{dr}(s) &= A\frac{1}{L_{YP}}\left\{L_{YP}\int_{L_1}^{L_1+D_1}qG(x,s)dx+\left(L_{YP}-L_Y'\right)\int_0^{L_1}qG(x,s)dx\right\} \\ &= \frac{A}{L_{YP}}q\Phi_0(s)\left\{L_{YP}\left[e^{-\alpha L_1}-e^{-\alpha(L_1+D_1)}\right]+\left(L_{YP}-L_Y'\right)\left(1-e^{-\alpha L_1}\right)\right\}. \end{aligned}$$

3.4 Total Current

The output current $I_o(s)$ is

$$I_o(s)=I_p(s)+I_n(s)+I_{dr}(s). \qquad (43)$$

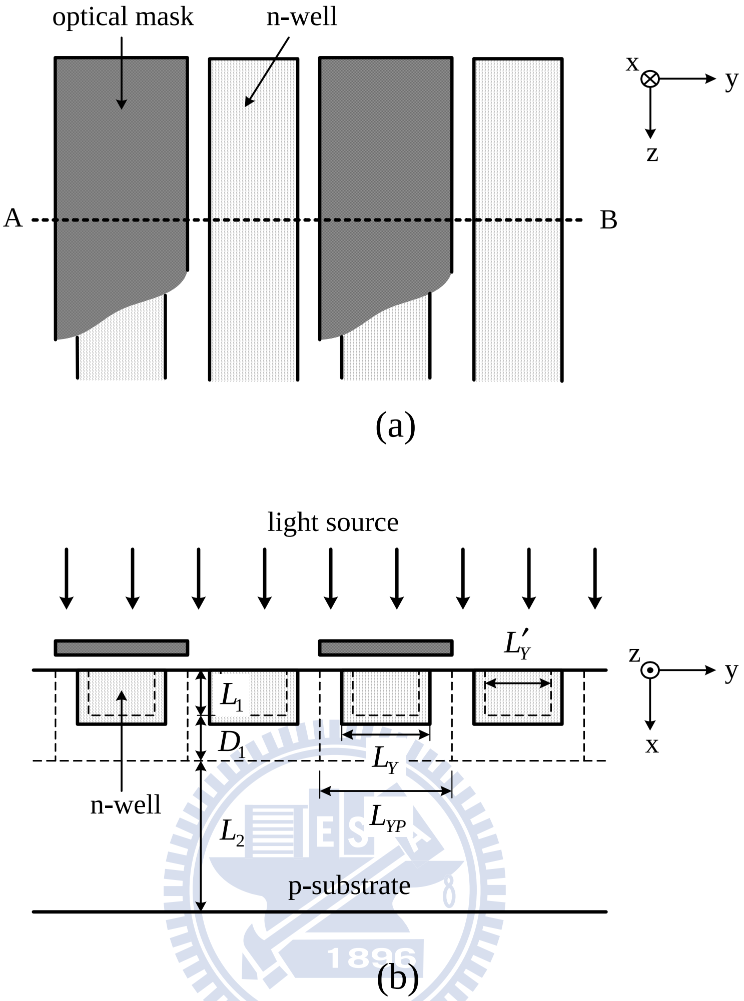

Figure 6: Finger-shaped SMPD, (a) top view, (b) cross section along line $\overline{AB}$.

4 Finger-Shaped SMPD

Consider a finger-shaped SMPD shown in Fig. 6. The generation rates of carriers per unit volume in the time-domain and frequency-domain are

$$g(x, y, t) = \alpha\Phi_0(t)e^{-\alpha x}f(y), \tag{44}$$

$$G(x, y, s) = \alpha\Phi_0(s)e^{-\alpha x}f(y). \tag{45}$$

4.1 N-type Neutral Region

In the N-type neutral region, the boundary conditions are similar to the case in a finger photodiode. Therefore, the diffusion current $I_p(s)$ in the N-type neutral region is obtained as

$$\begin{aligned}
I_p(s) &= -AqD_p\frac{1}{2L_{YP}}\left[\int_0^{L_Y'}\left.\frac{\partial P_n}{\partial x}\right|_{x=L_1}dy+\int_0^{L_1}-\left.\frac{\partial P_n}{\partial y}\right|_{y=0}dx+\int_0^{L_1}\left.\frac{\partial P_n}{\partial y}\right|_{y=L_Y'}dx\right] \\
&= \sum_{m=1}^{\infty}\sum_{n=1}^{\infty}\frac{A}{2L_{YP}}qD_p\alpha\Phi_0(s)\frac{1}{s+D_p\left[\frac{(2m-1)\pi}{2L_1}\right]^2+D_p\left[\frac{(2n-1)\pi}{L_Y'}\right]^2+\frac{1}{\tau_p}}\times\frac{4(-1)^{m+1}}{(2n-1)\pi} \\
&\quad\times\frac{(2m-1)\pi(-1)^{m+1}e^{-\alpha L_1}+2\alpha L_1}{(\alpha L_1)^2+\left[\frac{(2m-1)\pi}{2}\right]^2}\times\left[\frac{L_Y'}{L_1}\frac{2m-1}{2n-1}+\frac{L_1}{L_Y'}\frac{4\,(2n-1)}{2m-1}\right]. \qquad (46)
\end{aligned}$$

4.2 P-type Neutral Region

In the P-type neutral region, the continuity equation for electrons in the time-domain and frequency-domain are

$$\frac{\partial n_p(x',y,t)}{\partial t}=D_n\frac{\partial^2 n_p(x',y,t)}{\partial x'^2}+D_n\frac{\partial^2 n_p(x',y,t)}{\partial y^2}-\frac{n_p(x',y,t)}{\tau_n}+g(x',y,t), \qquad (47)$$

$$sN_p(x',y,s)=D_n\frac{\partial^2 N_p(x',y,s)}{\partial x'^2}+D_n\frac{\partial^2 N_p(x',y,s)}{\partial y^2}-\frac{N_p(x',y,s)}{\tau_n}+G(x',y,s), \qquad (48)$$

and the boundary conditions are

$$\begin{aligned}
n_p\big|_{x'=0} &= 0, \quad n_p\big|_{x'=L_2}=0, && (49)\\
n_p\left(x',y\right) &= n_p\left(x',y+L_{YP}\right),\ \text{for } 0\le x'\le L_2. && (50)
\end{aligned}$$

A function $f_4(y)$ shown in Fig. 7 can satisfy the boundary conditions for $0 \le x' \le L_2$.

Since the Fourier series coefficeint B_n can be evaluated as

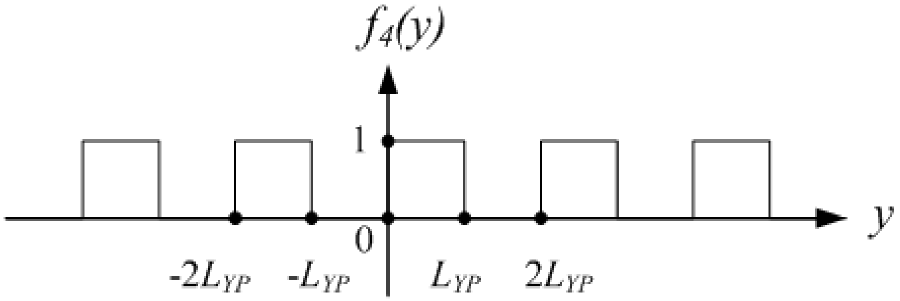

Figure 7: Waveform of $f_4(y)$

$$\begin{aligned} B_n &= \frac{2}{L_{YP}} \int_0^{L_{YP}} f_4(y) \sin\left[\frac{n\pi}{L_{YP}} y\right] dy \\ &= \frac{2}{(2n-1)\pi}, \end{aligned} \tag{51}$$

$f_4(y)$ can be expressed as

$$f_4(y) = \frac{1}{2} + \sum_{n=1}^{\infty} B_n \sin\left[\frac{(2n-1)\pi}{L_{YP}} y\right], \text{ for } 0 \le x' \le L_2, \tag{52}$$

and then $G(x', y, s)$ can be expressed as

$$G(x', y, s) = \alpha\Phi_0(s) e^{-\alpha(L_1+D_1)} \left[\sum_{m=1}^{\infty} B_m \sin\left(\frac{m\pi}{L_2} x'\right)\right] f_4(y), \text{ for } 0 \le x' \le L_2. \tag{53}$$

Thus, $N_p(x', y, s)$ can be expressed as

$$\begin{aligned} N_p(x', y, s) &= \alpha\Phi_0(s) e^{-\alpha(L_1+D_1)} \left\{ \sum_{m=1}^{\infty} b_m \sin\left(\frac{m\pi}{L_2} x'\right) \right. \\ &\left. + \sum_{m=1}^{\infty} \sum_{n=1}^{\infty} b_{mn} \sin\left(\frac{m\pi}{L_2} x'\right) \sin\left[\frac{(2n-1)\pi}{L_{YP}} y\right] \right\}, \end{aligned} \tag{54}$$

where b_m and b_{mn} can be evaluated as

$$
\begin{aligned}
b_m &= \frac{B_m}{2\left[s + D_n\left(\frac{m\pi}{L_2}\right)^2 + \frac{1}{\tau_n}\right]} && (55)\\
b_{mn} &= \frac{B_m B_n}{s + D_n\left(\frac{m\pi}{L_2}\right)^2 + D_n\left[\frac{(2n-1)\pi}{L_{YP}}\right]^2 + \frac{1}{\tau_n}}. && (56)
\end{aligned}
$$

In the P-type neutral region, the immediate diffusion current $J_{nI}(s)$ (collected by the unblocked diode) and the deferred diffusion current $J_{nD}(s)$ (collected by the blocked diode) are then obtained as

$$
\begin{aligned}
I_{nI}(s) &= AqD_n\frac{1}{2L_{YP}}\int_0^{L_{YP}} \left.\frac{\partial N_p}{\partial x'}\right|_{x'=0} dy\\
&= \frac{A}{2}qD_n\alpha\Phi_0(s)e^{-\alpha(L_1+D_1)}\frac{m\pi}{L_2}\left[\sum_{m=1}^{\infty} C_m(s) + \sum_{m=1}^{\infty}\sum_{n=1}^{\infty} C_{mn}(s)\right], && (57)\\
I_{nD}(s) &= AqD_n\frac{1}{2L_{YP}}\int_{L_{YP}}^{2L_{YP}} \left.\frac{\partial N_p}{\partial x'}\right|_{x'=0} dy\\
&= \frac{A}{2}qD_n\alpha\Phi_0(s)e^{-\alpha(L_1+D_1)}\frac{m\pi}{L_2}\left[\sum_{m=1}^{\infty} C_m(s) - \sum_{m=1}^{\infty}\sum_{n=1}^{\infty} C_{mn}(s)\right], && (58)
\end{aligned}
$$

where

$$
\begin{aligned}
C_m(s) &= b_m\\
&= \frac{1}{2\left[s + D_n\left(\frac{m\pi}{L_2}\right)^2 + \frac{1}{\tau_n}\right]} \times \frac{2m\pi\left[1-(-1)^m e^{-\alpha L_2}\right]}{(\alpha L_2)^2 + (m\pi)^2},\\
C_{mn}(s) &= b_{mn}\frac{2}{(2n-1)\pi}\\
&= \frac{1}{s + D_n\left(\frac{m\pi}{L_2}\right)^2 + D_n\left[\frac{(2n-1)\pi}{L_{YP}}\right]^2 + \frac{1}{\tau_n}} \times \frac{2m\pi\left[1-(-1)^m e^{-\alpha L_2}\right]}{(\alpha L_2)^2 + (m\pi)^2} \times \left[\frac{2}{(2n-1)\pi}\right]^2.
\end{aligned}
$$

4.3 Depletion Region

In the depletion region, the drift current $I_{dr}(s)$ is

$$\begin{aligned} I_{dr}(s) &= A\frac{1}{2L_{YP}}\left\{L_{YP}\int_{L_1}^{L_1+D_1} qG(x,s)dx + \left(L_{YP}-L_Y^{'}\right)\int_0^{L_1} qG(x,s)dx\right\} \\ &= \frac{A}{2L_{YP}}q\Phi_0(s)\left\{L_{YP}\left[e^{-\alpha L_1}-e^{-\alpha(L_1+D_1)}\right] + \left(L_{YP}-L_Y^{'}\right)\left(1-e^{-\alpha L_1}\right)\right\}. \end{aligned}$$

4.4 Total Current

Therefore, the differential output current $I_{od}(s)$ is

$$I_{od}(s) = I_p(s) + I_{nI}(s) + I_{dr}(s) - I_{nD}(s). \tag{59}$$

where

$$\begin{aligned} C_m(s) &= b_m \\ &= \frac{1}{2\left[s + D_n\left(\frac{m\pi}{L_2}\right)^2 + \frac{1}{\tau_n}\right]} \times \frac{2m\pi\left[1-(-1)^m e^{-\alpha L_2}\right]}{(\alpha L_2)^2 + (m\pi)^2}, \\ C_{mn}(s) &= b_{mn}\frac{2}{(2n-1)\pi} \\ &= \frac{1}{s + D_n\left(\frac{m\pi}{L_2}\right)^2 + D_n\left[\frac{(2n-1)\pi}{L_{YP}}\right]^2 + \frac{1}{\tau_n}} \times \frac{2m\pi\left[1-(-1)^m e^{-\alpha L_2}\right]}{(\alpha L_2)^2 + (m\pi)^2} \times \left[\frac{2}{(2n-1)\pi}\right]^2. \end{aligned}$$

5 Rectangle-Shaped SMPD

Consider a jag-type rectangle-shaped SMPD shown in Fig. 8. The generation rates of carriers per unit volume in the time-domain and frequency-domain are

$$g(x,y,z,t) = \alpha\Phi_0(t)e^{-\alpha x}f(y)f(z). \tag{60}$$

$$G(x,y,z,s) = \alpha\Phi_0(s)e^{-\alpha x}f(y)f(z). \tag{61}$$

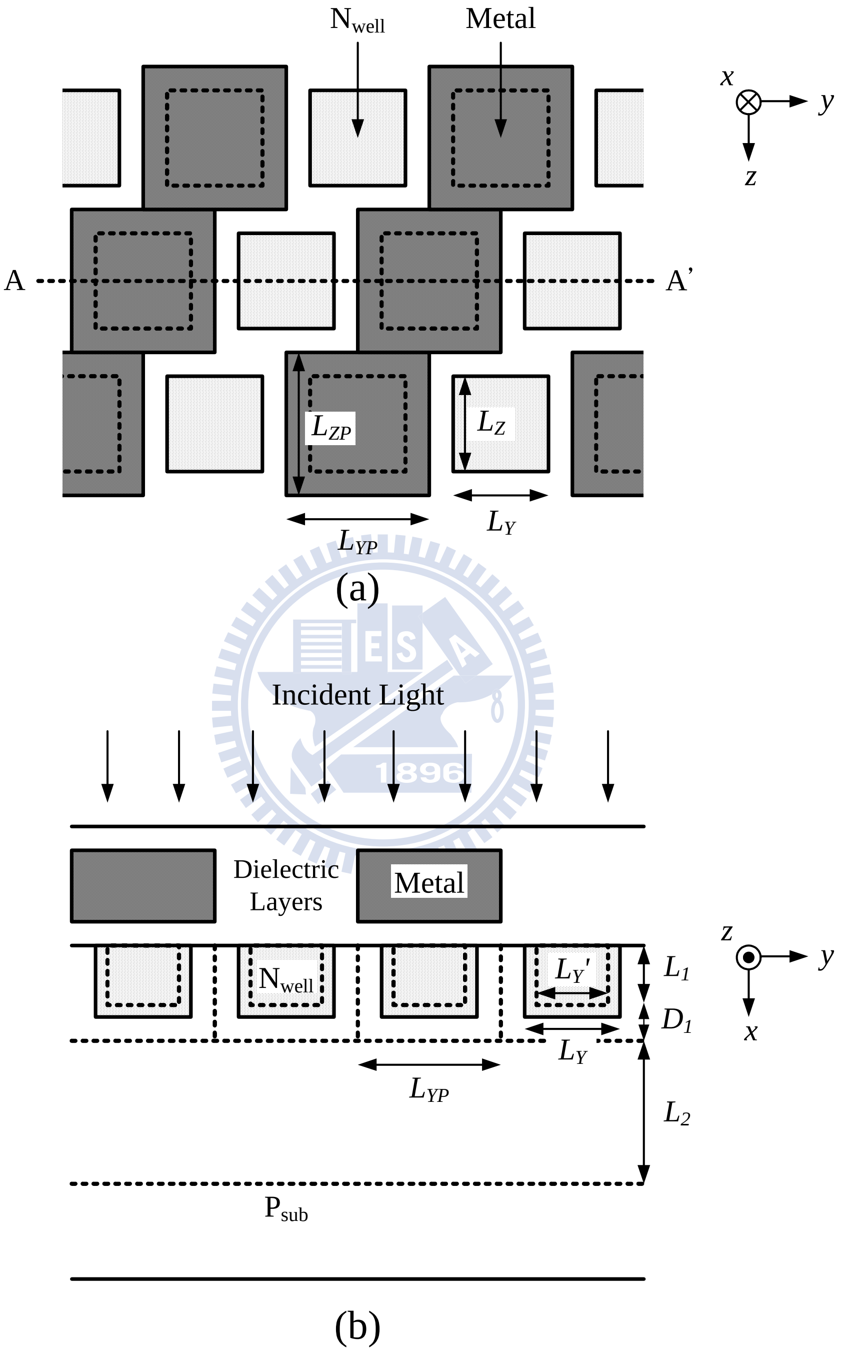

Figure 8: Rectangle-shaped SMPD, (a) top view, (b) cross section along line $\overline{AA'}$.

5.1 N-type Neutral Region

In the N-type neutral region, the continuity equations for holes in the time-domain and frequency-domain are

$$\frac{\partial p_n}{\partial t} = D_p \frac{\partial^2 p_n}{\partial^2 x} + D_p \frac{\partial^2 p_n}{\partial^2 y} + D_p \frac{\partial^2 p_n}{\partial^2 z} - \frac{p_n}{\tau_p} + g(x, y, z, t), \tag{62}$$

$$sP_n = D_p \frac{\partial^2 P_n}{\partial^2 x} + D_p \frac{\partial^2 P_n}{\partial^2 y} + D_p \frac{\partial^2 P_n}{\partial^2 z} - \frac{P_n}{\tau_p} + G(x, y, z, s), \tag{63}$$

and the boundary conditions are

$$\begin{aligned} \left.\frac{\partial p_n}{\partial x}\right|_{x=0} &= 0, \quad p_n|_{x=L_1} = 0, & (64) \\ p_n|_{y=0} &= 0, \quad p_n|_{y=L'_Y} = 0, \text{ for } 0 \le x \le L_1, & (65) \\ p_n|_{z=0} &= 0, \quad p_n|_{z=L'_Z} = 0, \text{ for } 0 \le x \le L_1. & (66) \end{aligned}$$

Functions $f_3(y)$ and $f_5(z)$ can satisfy the boundary conditions for $0 \le x \le L_1$, and can be expressed as

$$f_3(y) = \sum_{j=1}^{\infty} A_n \sin\left[\frac{(2n-1)\pi}{L'_Y} y\right] = \sum_{j=1}^{\infty} \frac{4}{(2n-1)\pi} \sin\left[\frac{(2n-1)\pi}{L'_Y} y\right], \tag{67}$$

$$f_5(z) = \sum_{k=1}^{\infty} A_k \sin\left[\frac{(2k-1)\pi}{L'_Z} z\right] = \sum_{k=1}^{\infty} \frac{4}{(2k-1)\pi} \sin\left[\frac{(2k-1)\pi}{L'_Z} z\right]. \tag{68}$$

Thus, $G(x, y, z, s)$ and $P_n(x, y, z, s)$can be expressed as

$$G(x, y, z, s) = \alpha\Phi_0(s) \left\{ \sum_{m=1}^{\infty} A_m \cos\left[\frac{(2m-1)\,\pi}{2L_1} x\right] \right\} f_3(y) f_5(z), \tag{69}$$

$$P_n(x, y, z, s) = \alpha\Phi_0(s) \sum_{m=1}^{\infty} \sum_{n=1}^{\infty} \sum_{k=1}^{\infty} a_{mnk} \cos\left[\frac{(2m-1)\,\pi}{2L_1} x\right] \sin\left[\frac{(2n-1)\pi}{L'_Y} y\right] \sin\left[\frac{(2k-1)\pi}{L'_Z} z\right], \tag{70}$$

where a_{mnk} can be evaluated as

$$a_{mnk} = \frac{A_m A_n A_k}{s + D_p \left[\frac{(2m-1)\pi}{2L_1}\right]^2 + D_p \left[\frac{(2n-1)\pi}{L'_Y}\right]^2 + D_p \left[\frac{(2k-1)\pi}{L'_Z}\right]^2 + \frac{1}{\tau_p}}. \tag{71}$$

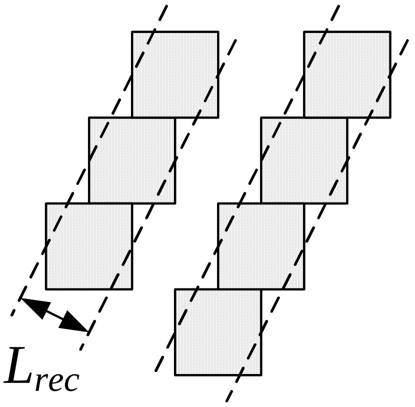

Figure 9: Boundary conditions in the P-type neutral region of rec-type SMPD.

The diffusion current $I_p(s)$ in the N-type neutral region is then obtained as

$$\begin{aligned}
I_p(s) &= -AqD_p\frac{1}{2L_{YP}L_{ZP}}\left[\int_{z=0}^{L_Z^{'}}\int_{y=0}^{L_Y^{'}}\left.\frac{\partial P_n}{\partial x}\right|_{x=L_1}dydz\right.\\
&\quad\left.+2\int_{z=0}^{L_Z^{'}}\int_{x=0}^{L_1}\left.\frac{\partial P_n}{\partial y}\right|_{y=L_Y^{'}}dxdz+2\int_{y=0}^{L_Y^{'}}\int_{x=0}^{L_1}\left.\frac{\partial P_n}{\partial z}\right|_{z=L_Z^{'}}dxdy\right]\\
&= AqD_p\alpha\Phi_0(s)\frac{1}{2L_{YP}L_{ZP}}\sum_{m=1}^{\infty}\sum_{n=1}^{\infty}\sum_{k=1}^{\infty}a_{mnk}(-1)^{m+1}\left[\frac{L_Y^{'}L_Z^{'}}{L_1}\frac{2\,(2m-1)}{(2n-1)(2k-1)\pi}\right.\\
&\quad\left.+\frac{L_1L_Z^{'}}{L_Y^{'}}\frac{8(2n-1)}{(2m-1)\,(2k-1)\pi}+\frac{L_1L_Y^{'}}{L_Z^{'}}\frac{8(2k-1)}{(2m-1)\,(2n-1)\pi}\right]\\
&= \frac{AqD_p\alpha\Phi_0(s)}{2L_{YP}L_{ZP}}\sum_{m=1}^{\infty}\sum_{n=1}^{\infty}\sum_{k=1}^{\infty}\frac{1}{s+D_p\left[\frac{(2m-1)\pi}{2L_1}\right]^2+D_p\left[\frac{(2n-1)\pi}{L_Y^{'}}\right]^2+D_p\left[\frac{(2k-1)\pi}{L_Z^{'}}\right]^2+\frac{1}{\tau_p}}\\
&\quad\times\frac{(2m-1)\pi(-1)^{m+1}e^{-\alpha L_1}+2\alpha L_1}{(\alpha L_1)^2+\left[\frac{(2m-1)\pi}{2}\right]^2}\times\frac{4}{(2n-1)\pi}\times\frac{4}{(2k-1)\pi}\times(-1)^{m+1}\\
&\quad\times\left[\frac{L_Y^{'}L_Z^{'}}{L_1}\frac{2\,(2m-1)}{(2n-1)(2k-1)\pi}+\frac{L_1L_Z^{'}}{L_Y^{'}}\frac{8(2n-1)}{(2m-1)\,(2k-1)\pi}\right.\\
&\quad\left.+\frac{L_1L_Y^{'}}{L_Z^{'}}\frac{8(2k-1)}{(2m-1)\,(2n-1)\pi}\right]. \qquad (72)
\end{aligned}$$

5.2 P-type Neutral Region

In the P-type neutral region, the boundary conditions can be approximated to the case in Line-type SML-detector, as shown in Fig. 9, except that L_{YP} is substituded by $L_{rec}=2\sqrt{5}\frac{L_{YP}L_{YP}}{L_{YP}+4L_{YP}}$.

Therefore, in the P-type neutral region, the immediate diffusion current $I_{nI}(s)$ (collected by the unblocked diode) and the deferred diffusion current $I_{nD}(s)$ (collected by the blocked diode) are obtained as

$$\begin{aligned} I_{nI}(s) &= AqD_n\alpha\Phi_0(s)e^{-\alpha(L_1+D_1)}\frac{m\pi}{2L_2}\left[\sum_{m=1}^{\infty}C_m(s)+\sum_{m=1}^{\infty}\sum_{n=1}^{\infty}C_{mn}(s)\right], \qquad (73) \\ I_{nD}(s) &= AqD_n\alpha\Phi_0(s)e^{-\alpha(L_1+D_1)}\frac{m\pi}{2L_2}\left[\sum_{m=1}^{\infty}C_m(s)-\sum_{m=1}^{\infty}\sum_{n=1}^{\infty}C_{mn}(s)\right], \qquad (74) \end{aligned}$$

where

$$\begin{aligned} C_m(s) &= \frac{1}{2\left[s+D_n\left(\frac{m\pi}{L_2}\right)^2+\frac{1}{\tau_n}\right]}\times\frac{2m\pi\left[1-(-1)^m e^{-\alpha L_2}\right]}{(\alpha L_2)^2+(m\pi)^2}, \\ C_{mn}(s) &= \frac{1}{s+D_n\left(\frac{m\pi}{L_2}\right)^2+D_n\left[\frac{(2n-1)\pi}{L_{rect}}\right]^2+\frac{1}{\tau_n}}\times\frac{2m\pi\left[1-(-1)^m e^{-\alpha L_2}\right]}{(\alpha L_2)^2+(m\pi)^2}\times\left[\frac{2}{(2n-1)\pi}\right]^2. \end{aligned}$$

5.3 Depletion Region

In the depletion region, the drift current is

$$\begin{aligned} I_{dr}(s) &= A\frac{1}{2L_{YP}L_{ZP}}\left\{L_{YP}L_{ZP}\int_{L_1}^{L_1+D_1}qG(x,s)dx+\left(L_{YP}L_{ZP}-L_Y^{'}L_Z^{'}\right)\int_0^{L_1}qG(x,s)dx\right\} \\ &= \frac{Aq\Phi_0(s)}{2L_{YP}L_{ZP}}\left\{L_{YP}L_{ZP}\left[e^{-\alpha L_1}-e^{-\alpha(L_1+D_1)}\right]+\left(L_{YP}L_{ZP}-L_Y^{'}L_Z^{'}\right)\left(1-e^{-\alpha L_1}\right)\right\}. \end{aligned}$$

5.4 Total Current

Therefore, the differential output current $I_{od}(s)$ is

$$I_{od}(s)=I_p(s)+I_{nI}(s)+I_{dr}(s)-I_{nD}(s). \qquad (75)$$

6 Meshed SMPD

Consider a meshed SMPD shown in Fig. 10. The generation rates of carriers per unit volume in the time-domain and frequency-domain are

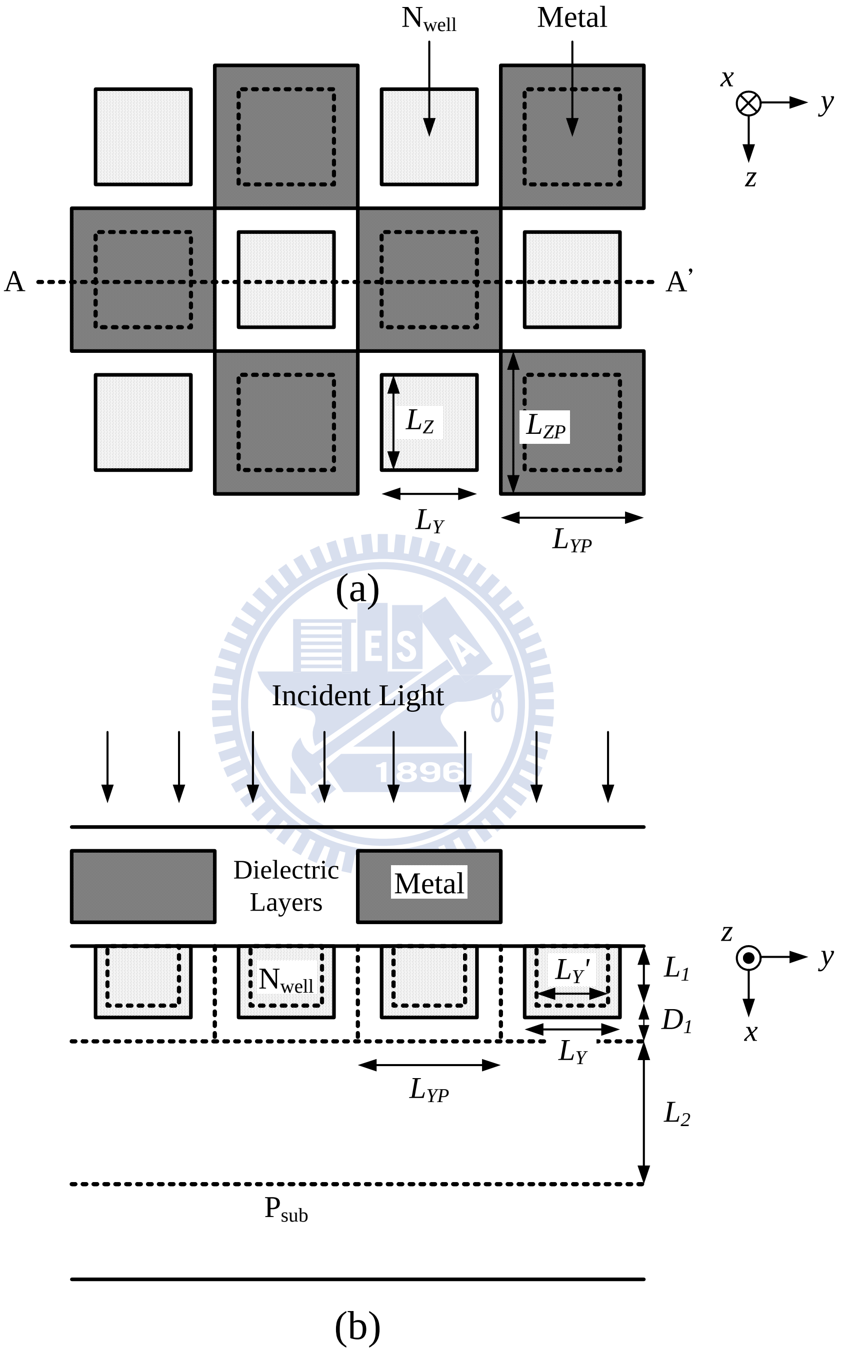

Figure 10: Meshed SMPD, (a) top view, (b) cross section along line $\overline{AA'}$.

$$g(x,y,z,t) = \alpha\Phi_0(t)e^{-\alpha x}f(y)f(z). \tag{76}$$

$$G(x,y,z,s) = \alpha\Phi_0(s)e^{-\alpha x}f(y)f(z). \tag{77}$$

6.1 N-type Neutral Region

In the N-type neutral region, the continuity equations for holes in the time-domain and frequency-domain are

$$\frac{\partial p_n}{\partial t} = D_p\frac{\partial^2 p_n}{\partial^2 x} + D_p\frac{\partial^2 p_n}{\partial^2 y} + D_p\frac{\partial^2 p_n}{\partial^2 z} - \frac{p_n}{\tau_p} + g(x,y,z,t), \tag{78}$$

$$sP_n = D_p\frac{\partial^2 P_n}{\partial^2 x} + D_p\frac{\partial^2 P_n}{\partial^2 y} + D_p\frac{\partial^2 P_n}{\partial^2 z} - \frac{P_n}{\tau_p} + G(x,y,z,s), \tag{79}$$

and the boundary conditions are

$$\begin{aligned} \left.\frac{\partial p_n}{\partial x}\right|_{x=0} &= 0, \quad p_n|_{x=L_1} = 0, & (80)\\ p_n|_{y=0} &= 0, \quad p_n|_{y=L'_Y} = 0, \text{ for } 0 \le x \le L_1, & (81)\\ p_n|_{z=0} &= 0, \quad p_n|_{z=L'_Z} = 0, \text{ for } 0 \le x \le L_1. & (82) \end{aligned}$$

Functions $f_3(y)$ and $f_5(z)$ can satisfy the boundary conditions for $0 \le x \le L_1$, and can be expressed as

$$f_3(y) = \sum_{j=1}^{\infty} A_n \sin\left[\frac{(2n-1)\pi}{L'_Y}y\right] = \sum_{j=1}^{\infty} \frac{4}{(2n-1)\pi}\sin\left[\frac{(2n-1)\pi}{L'_Y}y\right], \tag{83}$$

$$f_5(z) = \sum_{k=1}^{\infty} A_k \sin\left[\frac{(2k-1)\pi}{L'_Z}z\right] = \sum_{k=1}^{\infty} \frac{4}{(2k-1)\pi}\sin\left[\frac{(2k-1)\pi}{L'_Z}z\right]. \tag{84}$$

Thus, $G(x,y,z,s)$ and $P_n(x,y,z,s)$can be expressed as

$$G(x,y,z,s) = \alpha\Phi_0(s)\left\{\sum_{m=1}^{\infty} A_m \cos\left[\frac{(2m-1)\,\pi}{2L_1}x\right]\right\} f_3(y)f_5(z), \tag{85}$$

$$P_n(x,y,z,s) = \alpha\Phi_0(s)\sum_{m=1}^{\infty}\sum_{n=1}^{\infty}\sum_{k=1}^{\infty} a_{mnk}\cos\left[\frac{(2m-1)\,\pi}{2L_1}x\right]\sin\left[\frac{(2n-1)\pi}{L_Y^{'}}y\right]\sin\left[\frac{(2k-1)\pi}{L_Z^{'}}z\right], \tag{86}$$

where a_{mnk} can be evaluated as

$$a_{mnk} = \frac{A_m A_n A_k}{s + D_p\left[\frac{(2m-1)\pi}{2L_1}\right]^2 + D_p\left[\frac{(2n-1)\pi}{L_Y^{'}}\right]^2 + D_p\left[\frac{(2k-1)\pi}{L_Z^{'}}\right]^2 + \frac{1}{\tau_p}}. \tag{87}$$

The diffusion current $I_p(s)$ in the N-type neutral region is then obtained as

$$\begin{aligned}
I_p(s) &= -AqD_p\frac{1}{2L_{YP}L_{ZP}}\left[\int_{z=0}^{L_Z^{'}}\int_{y=0}^{L_Y^{'}}\left.\frac{\partial P_n}{\partial x}\right|_{x=L_1}dydz\right. \\
&\quad \left.+2\int_{z=0}^{L_Z^{'}}\int_{x=0}^{L_1}\left.\frac{\partial P_n}{\partial y}\right|_{y=L_Y^{'}}dxdz + 2\int_{y=0}^{L_Y^{'}}\int_{x=0}^{L_1}\left.\frac{\partial P_n}{\partial z}\right|_{z=L_Z^{'}}dxdy\right] \\
&= AqD_p\alpha\Phi_0(s)\frac{1}{2L_{YP}L_{ZP}}\sum_{m=1}^{\infty}\sum_{n=1}^{\infty}\sum_{k=1}^{\infty}a_{mnk}(-1)^{m+1}\left[\frac{L_Y^{'}L_Z^{'}}{L_1}\frac{2\,(2m-1)}{(2n-1)(2k-1)\pi}\right. \\
&\quad \left.+\frac{L_1L_Z^{'}}{L_Y^{'}}\frac{8(2n-1)}{(2m-1)\,(2k-1)\pi}+\frac{L_1L_Y^{'}}{L_Z^{'}}\frac{8(2k-1)}{(2m-1)\,(2n-1)\pi}\right] \\
&= \frac{AqD_p\alpha\Phi_0(s)}{2L_{YP}L_{ZP}}\sum_{m=1}^{\infty}\sum_{n=1}^{\infty}\sum_{k=1}^{\infty}\frac{1}{s + D_p\left[\frac{(2m-1)\pi}{2L_1}\right]^2 + D_p\left[\frac{(2n-1)\pi}{L_Y^{'}}\right]^2 + D_p\left[\frac{(2k-1)\pi}{L_Z^{'}}\right]^2 + \frac{1}{\tau_p}} \\
&\quad \times\frac{(2m-1)\pi(-1)^{m+1}e^{-\alpha L_1}+2\alpha L_1}{(\alpha L_1)^2+\left[\frac{(2m-1)\pi}{2}\right]^2}\times\frac{4}{(2n-1)\pi}\times\frac{4}{(2k-1)\pi}\times(-1)^{m+1} \\
&\quad \times\left[\frac{L_Y^{'}L_Z^{'}}{L_1}\frac{2\,(2m-1)}{(2n-1)(2k-1)\pi}+\frac{L_1L_Z^{'}}{L_Y^{'}}\frac{8(2n-1)}{(2m-1)\,(2k-1)\pi}\right. \\
&\quad \left.+\frac{L_1L_Y^{'}}{L_Z^{'}}\frac{8(2k-1)}{(2m-1)\,(2n-1)\pi}\right].
\end{aligned} \tag{88}$$

6.2 P-type Neutral Region

In the P-type neutral region, the continuity equation for electrons in the time-domain and frequency-domain are

$$\frac{\partial n_p(x',y,t)}{\partial t} = D_n\frac{\partial^2 n_p(x',y,t)}{\partial x'^2} + D_n\frac{\partial^2 n_p(x',y,t)}{\partial y^2} - \frac{n_p(x',y,t)}{\tau_n} + g(x',y,t), \tag{89}$$

$$sN_p(x',y,s) = D_n\frac{\partial^2 N_p(x',y,s)}{\partial x'^2} + D_n\frac{\partial^2 N_p(x',y,s)}{\partial y^2} - \frac{N_p(x',y,s)}{\tau_n} + G(x',y,s), \tag{90}$$

and the boundary conditions are

$$\begin{aligned} n_p\big|_{x'=0} &= 0, \quad n_p\big|_{x'=L_2} = 0, && (91)\\ n_p\left(y=0\right) &= n_p\left(y=L_{YP}\right), \text{ for } 0 \le x' \le L_2, && (92)\\ n_p\left(z=0\right) &= n_p\left(z=L_{ZP}\right), \text{ for } 0 \le x' \le L_2. && (93)\end{aligned}$$

The function $f_4(y)$ and $f_4(z)$ can satisfy the boundary conditions for $0 \le x' \le L_2$.

Since the Fourier series coefficeints B_n and B_k can be evaluated as

$$\begin{aligned} B_n &= \frac{2}{L_{YP}}\int_0^{L_{YP}} f_4(y)\sin\left[\frac{n\pi}{L_{YP}}y\right]dy && (94)\\ &= \frac{2}{(2n-1)\pi}, && (95)\end{aligned}$$

$$\begin{aligned} B_k &= \frac{2}{L_{ZP}}\int_0^{L_{ZP}} f_4(z)\sin\left[\frac{k\pi}{L_{ZP}}y\right]dz \\ &= \frac{2}{(2k-1)\pi}, && (96)\end{aligned}$$

$f_4(y)$ and $f_4(z)$ can be expressed as

$$f_4(y) = \frac{1}{2} + \sum_{n=1}^{\infty} B_n \sin\left[\frac{(2n-1)\pi}{L_{YP}}y\right], \text{ for } 0 \le x' \le L_2, \tag{97}$$

$$f_4(z) = \frac{1}{2} + \sum_{k=1}^{\infty} B_k \sin\left[\frac{(2k-1)\pi}{L_{ZP}}z\right], \text{ for } 0 \le x' \le L_2, \tag{98}$$

and then $G(x',y,s)$ can be expressed as

$$G(x', y, s) = \alpha \Phi_0(s) e^{-\alpha(L_1+D_1)} \left[\sum_{m=1}^{\infty} B_m \sin\left(\frac{m\pi}{L_2}x'\right)\right] f_4(y) f_4(z), \text{ for } 0 \le x' \le L_2. \quad (99)$$

Thus, $N_p(x', y, s)$ can be expressed as

$$\begin{aligned} N_p(x', y, s) &= \alpha \Phi_0(s) e^{-\alpha(L_1+D_1)} \left\{ \sum_{m=1}^{\infty} b_m \sin\left(\frac{m\pi}{L_2}x'\right) \right. \\ &+ \sum_{m=1}^{\infty}\sum_{n=1}^{\infty} b_{mn} \sin\left(\frac{m\pi}{L_2}x'\right) \sin\left[\frac{(2n-1)\pi}{L_{YP}}y\right] \\ &+ \sum_{m=1}^{\infty}\sum_{k=1}^{\infty} b_{mk} \sin\left(\frac{m\pi}{L_2}x'\right) \sin\left[\frac{(2k-1)\pi}{L_{ZP}}z\right] \\ &+ \left. \sum_{m=1}^{\infty}\sum_{n=1}^{\infty}\sum_{k=1}^{\infty} b_{mnk} \sin\left(\frac{m\pi}{L_2}x'\right) \sin\left[\frac{(2n-1)\pi}{L_{YP}}y\right] \sin\left[\frac{(2k-1)\pi}{L_{ZP}}z\right] \right\}, \end{aligned}$$

where b_m, b_{mn}, b_{mk}, and b_{mnk} can be evaluated as

$$b_m = \frac{B_m}{4\left[s + D_n\left(\frac{m\pi}{L_2}\right)^2 + \frac{1}{\tau_n}\right]} \quad (100)$$

$$b_{mn} = \frac{B_m B_n}{2\left\{s + D_n\left(\frac{m\pi}{L_2}\right)^2 + D_n\left[\frac{(2n-1)\pi}{L_{YP}}\right]^2 + \frac{1}{\tau_n}\right\}} \quad (101)$$

$$b_{mk} = \frac{B_m B_k}{2\left\{s + D_n\left(\frac{m\pi}{L_2}\right)^2 + D_n\left[\frac{(2k-1)\pi}{L_{ZP}}\right]^2 + \frac{1}{\tau_n}\right\}} \quad (102)$$

$$b_{mnk} = \frac{B_m B_n B_k}{s + D_n\left(\frac{m\pi}{L_2}\right)^2 + D_n\left[\frac{(2n-1)\pi}{L_{YP}}\right]^2 + D_n\left[\frac{(2k-1)\pi}{L_{ZP}}\right]^2 + \frac{1}{\tau_n}}. \quad (103)$$

In the P-type neutral region, the immediate diffusion current $J_{nI}(s)$ (collected by the unblocked diode) and the deferred diffusion current $J_{nD}(s)$ (collected by the blocked diode) are then obtained as

$$
\begin{aligned}
I_{nI}(s) &= \frac{A}{4L_{YP}L_{YP}} qD_n \left[\int_0^{L_{ZP}} \int_0^{L_{YP}} \left. \frac{\partial N_p}{\partial x'} \right|_{x'=0} dydz + \int_{L_{ZP}}^{2L_{ZP}} \int_{L_{YP}}^{2L_{YP}} \left. \frac{\partial N_p}{\partial x'} \right|_{x'=0} dydz \right] \\
&= \frac{A}{4L_{YP}L_{YP}} qD_n \alpha \Phi_0(s) e^{-\alpha(L_1+D_1)} \frac{m\pi}{L_2} \left[\sum_{m=1}^{\infty} C_m(s) + \sum_{m=1}^{\infty}\sum_{n=1}^{\infty} C_{mnk}(s) \right], \\
I_{nD}(s) &= \frac{A}{4L_{YP}L_{YP}} qD_n \left[\int_0^{L_{ZP}} \int_{L_{YP}}^{2L_{YP}} \left. \frac{\partial N_p}{\partial x'} \right|_{x'=0} dydz + \int_{L_{ZP}}^{2L_{ZP}} \int_0^{L_{YP}} \left. \frac{\partial N_p}{\partial x'} \right|_{x'=0} dydz \right] \\
&= \frac{A}{4L_{YP}L_{YP}} qD_n \alpha \Phi_0(s) e^{-\alpha(L_1+D_1)} \frac{m\pi}{L_2} \left[\sum_{m=1}^{\infty} C_m(s) - \sum_{m=1}^{\infty}\sum_{n=1}^{\infty} C_{mnk}(s) \right],
\end{aligned}
$$

where

$$
\begin{aligned}
C_m(s) &= 2b_m L_{YP} L_{ZP} \\
&= \frac{L_{YP}L_{ZP}}{2\left[s + D_n \left(\frac{m\pi}{L_2}\right)^2 + \frac{1}{\tau_n} \right]} \times \frac{2m\pi\left[1-(-1)^m e^{-\alpha L_2}\right]}{(\alpha L_2)^2 + (m\pi)^2}, \\
C_{mnk}(s) &= 8b_{mnk} \frac{L_{YP}}{(2n-1)\pi} \frac{L_{ZP}}{(2k-1)\pi} \\
&= \frac{8L_{YP}L_{ZP}}{s + D_n\left(\frac{m\pi}{L_2}\right)^2 + D_n\left[\frac{(2n-1)\pi}{L_{YP}}\right]^2 + D_n\left[\frac{(2k-1)\pi}{L_{ZP}}\right]^2 + \frac{1}{\tau_n}} \\
&\quad \times \frac{2m\pi\left[1-(-1)^m e^{-\alpha L_2}\right]}{(\alpha L_2)^2 + (m\pi)^2} \times \frac{2}{[(2n-1)\pi]^2} \times \frac{2}{[(2k-1)\pi]^2}.
\end{aligned}
$$

6.3 Depletion Region

In the depletion region, the drift current is

$$
\begin{aligned}
I_{dr}(s) &= A\frac{1}{2L_{YP}L_{ZP}} \left\{ L_{YP}L_{ZP} \int_{L_1}^{L_1+D_1} qG(x,s)dx + \left(L_{YP}L_{ZP} - L_Y^{'}L_Z^{'}\right) \int_0^{L_1} qG(x,s)dx \right\} \\
&= \frac{A}{2L_{YP}L_{ZP}} q\Phi_0(s) \left\{ L_{YP}L_{ZP}\left[e^{-\alpha L_1} - e^{-\alpha(L_1+D_1)}\right] + \left(L_{YP}L_{ZP} - L_Y^{'}L_Z^{'}\right)\left(1-e^{-\alpha L_1}\right) \right\}.
\end{aligned}
$$

6.4 Total Current

Therefore, the differential output current $I_{od}(s)$ is

$$I_{od}(s) = I_p(s) + I_{nI}(s) + I_{dr}(s) - I_{nD}(s). \tag{104}$$

Abbreviations

AA	ascorbic acid
ABTS	2,2’-azino-bis(3-ethylbenzthiazoline-6-sulphonic acid)
BER	bit-error-rate
BW	bandwidth
CMOS	complementary metal-oxide-semiconductor
Conc.	concentration
DAO	diamine oxidase
ddH$_2$O	double distilled water
DMEM	Dulbecco’s modified Eagle’s medium
DMSO	dimethyl sulfoxid
DNW	deep-N$_{well}$
EDTA	ethylene-diamine-tetraacetic acid
ELISA	enzyme-linked immuno-sorbent assay
FWHM	full width at half maximum
GBW	gain-bandwidth product
GOx	glucose oxidase
GPIB	general purpose interface bus
HRP	horseradish peroxidase
IC	integrated circuits
ICS	interactive characterization software
ImAA	imidazole acetic acid
incr. conc.	increasing concentration
MMF	multimode fibers
MOSFET	metal-oxide-semiconductor field-effect transistor
MTT	3-(4,5-dimethyl-2-thiazolyl)-2,5-diphenyltetrazolium-bromide]
NMOS	n-channel MOSFET
OEIC	optoelectronic integrated circuits
PA	post limiting amplifier
PASS	passivation layers
PBS	phosphate buffered saline

PD	photodiode
PMOS	p-channel MOSFET
PP	peak-to-peak
PRBS	pseudo-random binary sequence
PT	phototransistor
RGC	regulated cascode
RMS	root-mean-square
SD	standard deviation
SMPD	spatially modulated photodiode
SMPT	spatially modulated phototransistor
TIA	transimpedance amplifier
TMB	3,3’,5,5’-tetramethyl-benzidine
TSMC	Taiwan semiconductor manufacturing company

生化名詞中英對照

ABTS, 2,2’-azino-bis(3-ethylbenzthiazoline-6-sulphonic acid)	2,2’-連氮基-雙(3-乙基苯並二氫噻唑啉-6-磺酸)
acetaminophen	乙醯胺酚
antibiotic	抗生素
ascorbic acid	抗壞血酸
DAO, diamine oxidase	二氨氧化酶
DMEM, Dulbecco’s modified Eagle’s medium	經 Dulbecco 改良之 Eagle 培養基
DMSO, dimethyl sulfoxid	二甲基亞碸
DOPA	多巴
dopaquinone	多巴醌
EDTA, ethylene-diamine-tetraacetic acid	乙二胺四乙酸
ELISA, enzyme-linked immuno-sorbent assay	酶聯免疫吸附分析
fetal bovine serum	胎牛血清
formazan	甲臘
GOx, glucose oxidase	葡萄糖氧化酶
Gluconic Acid	葡萄糖酸
glucose	葡萄糖
histamine	組織胺
HRP, horseradish peroxidase	辣根過氧化酶
ImAA, imidazole acetic acid	咪唑醋酸
kojic acid	麴酸
lactate	乳酸
melanin	黑色素

melanocyte	黑素細胞
melanogenesis	黑素生成
mitochondrial enzyme	線粒體酶
MTT, 3-(4,5-dimethyl-2-thiazolyl)-2,5-diphenyltetrazolium-bromide]	3-(4,5-二甲基-2-噻唑基)-2,5-二苯基四氮唑溴鹽
murine melanoma cells	小鼠黑色素瘤細胞
PBS	磷酸鹽緩衝劑
sodium bicarbonate	重碳酸鈉
TMB, 3,3’,5,5’-tetramethyl-benzidine	3,3’,5,5’-四甲基聯苯胺
trypsin	胰蛋白酶
tyrosinase	酪氨酸酶
uric acid	尿酸

簡　歷

一、基本資料

姓　　名：張 育 維
英文姓名：Chang, Yu-Wei
姓　　別：男
出生日期：民國六十九年三月九日
籍　　貫：台灣

二、主要學歷

國立交通大學電子工程學系	1998/09－2002/06
國立陽明大學生醫光電研究所碩士班	2002/09－2004/06
國立交通大學電子研究所博士班	2004/09－2009/07

三、博士論文：應用於生醫感測與高速網路之互補式金氧半光偵測器

CMOS Photodetectors for Applications in Biomedical Detection and High-Speed Networks

四、著作

A. 期刊論文

1. W.-Z. Chen, S.-H. Huang, Y.-W. Chang, and Y.-T. Huang, “A 2.5 Gbps CMOS fully integrated optical receiver with lateral PIN detector,” *International Journal of Electrical Engineering*, vol. 15, no. 2, pp. 79-86, 2008.
2. Y.-W. Chang, P.-C. Yu, Y.-T. Huang, and Y.-S. Yang, “A high-sensitivity CMOS-compatible biosensing system based on absorption photometry,” *IEEE Sensors Journal*, vol. 9, no. 2, pp. 120-127, 2009.
3. Y.-W. Chang, Y.-T. Tai, Y.-T. Huang, and Y.-S. Yang, “A phototransistor-based high-sensitivity biosensing system using 650-nm light,” *IEEE Sensors Journal*, vol. 9, no. 6, pp. 673-677, 2009.
4. Y.-W. Chang and Y.-T. Huang, “The ring-shaped CMOS-based phototransistor with high responsivity for the UV/blue spectral range,” *IEEE Photonics Technology Letters*, vol. 21, no. 13, pp. 899-901, 2009.
5. Y.-W. Chang, S.-H. Huang, C.-C. Liu, Y.-T. Huang, and W.-Z. Chen, “Design and analysis of enhanced spatially-modulated photodetectors in a standard CMOS

technology," submitted to *IEEE Transactions on Electron Devices.*

B. 國際會議論文

1. Y.-W. Chang, P.-C. Yu, Y.-T. Huang, and Y.-S. Yang, "A CMOS-compatible optical biosensing system based on visible absorption spectroscopy," in *IEEE International Conference on Electron Devices and Solid-State Circuits*, Tainan, Taiwan, Dec. 20-22, 2007, vol. 2, pp. 1099-1101.
2. Y.-W. Chang, Y.-T. Tai, Y.-T. Huang, and Y.-S. Yang, "A CMOS-based phototransistor for high-sensitivity biochemical detection using absorption photometry," in *IEEE International Conference on Sensing Technology*, Tainan, Taiwan, Dec. 1-3, 2008, pp. 82-85.
3. M.-Y. Lin, Y.-W. Chang, Y.-T. Tai, Y.-T. Huang, and Y.-S. Yang, "A CMOS-compatible colorimetric biosensor based on an *in situ* isothermal nucleic acid amplification technology for protein detection," in *IEEE International Conference on Sensing Technology*, Tainan, Taiwan, Dec. 1-3, 2008, pp. 86-89.
4. Y.-T. Tai, Y.-W. Chang, M.-Y. Lin, Y.-S. Yang, and Y.-T. Huang, "A high-sensitivity CMOS-compatible immunosensor based on the HRP/TMB/streptavidin system," in *IEEE International Conference on Sensing Technology*, Tainan, Taiwan, Dec. 1-3, 2008, pp. 297-300.
5. Y.-W. Chang, Y.-P. Lu, M.-Y. Lin, Y.-T. Huang, and Y.-S. Yang, "A miniature CMOS Optoelectronic Biosensor for Screening Skin-Whitening Agents," in *35th Annual Northeast Bioengineering Conference*, Massachusetts, USA, April 3-5, 2009.
6. Y.-P. Lu, Y.-W. Chang, M.-Y. Lin, Y.-S. Yang, and Y.-T. Huang, "A Versatile, Portable CMOS Optoelectronic Platform for Screening Whitening Agents in Medical Cosmetics," in *9th IEEE International Conference on Bioinformatics and Bioengineering*, Taichung, Taiwan, June 22-24, 2009.
7. Y.-P. Lu, Y.-W. Chang, M.-Y. Lin, J.-S. Kao, Y.-S. Yang, and Y.-T. Huang, "CMOS Phototransistor Device: A total solution for Skin whitening Assays," in *3rd IEEE International Conference on Nano/Molecular Medicine and Engineering*, Tainan, Taiwan, Oct. 18-21, 2009.

五、榮譽

斐陶斐榮譽學會(The Phi Tau Phi Scholastic Honor Society)會員

國立交通大學電子研究所博士論文獎(Ph.D. Dissertation Award)